A MULTIWAVELENGTH STUDY OF THE

ACCRETION REGION IN

MAGNETIC CATACLYSMIC VARIABLES

Stephen Brian Potter

A thesis submitted to the University of London for the
degree of Doctor of Philosophy

Department of Space and Climate Physics
Mullard Space Science Laboratory
Department of Physics and Astronomy
University College London, London.
February 1998

Abstract

This thesis is a study of the accretion regions in magnetic cataclysmic variables (MCVs).

After an overview of our current understanding of accretion regions in MCVs, I describe a model I have developed which models the polarized cyclotron emission from MCVs. I then use this model to show how different types of cyclotron light curves arise for various shaped accretion regions.

I then use this model on the MCV PQ Gem. PQ Gem is an asynchronous intermediate polar (a subclass of the MCVs) with was discovered to have polarized emission on the spin period of the white dwarf. It was therefore an ideal candidate to observe and model. I found that the polarized light curves could be modelled by emission from two extended emission regions located on opposite hemispheres of the white dwarf. The model light curves could explain the observations as a combination of self occultation and absorption of the emission regions. The model is also more self consistent than other attempts in that it models the multi color observations of PQ Gem simultaneously and is in agreement with X-ray observations. I also give an estimate for the magnetic field strength of the white dwarf in this system.

Several authors over the past decade have modelled cyclotron emission from MCVs using their own models. However model fits have until now been obtained by a trial and error method. I obtained the results for PQ Gem by a similar method. Therefore I have developed an optimisation technique that is more analytical and objective than previous methods. This was achieved with the combination of a genetic algorithm and

a more traditional line minimisation routine. I described the technique in detail and rigorously test it on simulated light curves.

Having developed the optimisation technique, I then applied it to real data in order to predict the shape and size of their emission regions. The results are compared to previous models and preconceptions on the shape of emission regions. Also, by making assumptions on the nature of the magnetic field, I then trace the magnetic field lines that feed the emission regions to the orbital plane in order to locate the threading regions in these systems.

Finally, I give a summary of this thesis and discuss possible work for the future.

Contents

List of Tables

List of Figures

11

Preface

Magnetic cataclysmic variables are the source of a wealth of fascinating phenomena, evident in observations from X–rays to radio. The magnetic fields in these systems are responsible for much of the rich variety of observations, including circularly and linearly polarized infrared and optical radiation. Moreover, the X–ray, UV, optical and infrared emission from MCVs have been observed to have pulsations at the spin period of the white dwarf, at the binary orbital period, and at the sidebands of these frequencies all as a result of the magnetic field in these systems.

However, these same magnetic fields make these fascinating phenomena very difficult to understand both intuitively and theoretically. For example, the stream from the secondary penetrates the magnetic field of the white dwarf and interacts dynamically as the result of several plasma–physical processes and instabilities. It is also responsible for disrupted accretion discs which then flow via accretion curtains onto the white dwarf. The accretion curtain, or the magnetically threaded accretion stream, funnels the material onto small hot regions on the surface of the white dwarf. The structure of these 'hot spots', and the nature of their X–ray, UV and particularly cyclotron emissions, depend very sensitively on the way in which the magnetic field interacts with accreting plasma. Unfortunately our ability to investigate the structure of the 'hot spots' depends on poorly understood magnetohydrodynamic processes at the threading region.

Insights into the magnetohydrodynamic processes, however, can be inferred from multiwavelength observations. In particular, the cyclotron emission has been one of the most valuable characteristics of MCVs. This is because the cyclotron emission is highly angular and frequency depen-

dent. This thesis, therefore, has been devoted to the exploitation of the information that cyclotron radiation carries.

The beginning of my PhD began with the development of the cyclotron emission model discussed in chapter 2. Then, in the same manner as other authors with similar models, I used the model to 'hand fit' the polarimetric observations of the intermediate polar PQ Gem. The results form the basis of chapter 3 and have also be published in Potter et al. (1997). I received help from my collaborators to various degrees along the way, nevertheless, the data reduction and analysis, model fitting, comparisons and implications of the results have been my work. I have also obtained and modelled new polarimetric data of PQ Gem which has also been published in Howell et al. (1997).

The more sophisticated modelling techniques developed in chapter 4, evolved from the hand fitting models used in chapter 2 and 3. I have called this optimisation technique 'Stokes Imaging' and it has been submitted for publication (Potter, Hakala & Cropper 1998) All the work presented is my own. Furthermore, the resulting modelling and work presented in chapters 5 and 6 are all my own work. The polarimetric observations presented in chapter 6 were initially 'hand fitted' by myself before the development of the 'Stokes Imaging' technique, the results of which have been published in Ramsay et al. (1996).

I have also 'hand' modelled polarimetric data of the AM Her system RX J0515.6+0105 which is not presented in this thesis but has been published in Harrop-Allin et al. (1997). Other data I have reduced and analysed has been presented in Cropper et al (1998).

Chapter 1

Introduction

This thesis is centred on the study of the magnetic cataclysmic variables (MCVs), a subclass of cataclysmic variables (CVs). The main theme throughout each chapter concentrates on that region on the surface of the primary star in these systems which is responsible for most of the observed emission at all wavelengths. Of particular interest is the observed polarized cyclotron emission.

This introduction is provided to highlight the important fundamental properties and physical processes occurring in these systems, in preparation for the chapters to follow. It is not intended to be a fully comprehensive review: For a fully up to date review see Warner (1995). Other relatively recent and relevant reviews are: Cropper (1990), Patterson (1994) and Beuermann & Burwitz (1995).

1.1 The classification of cataclysmic variables

Historically a new object in the sky would make its appearance as a result of enhanced optical brightness from an outburst event or nova. The results of photometric and spectroscopic observations of these cataclysmic variables gradually led to the speculation that all such objects are binary systems. Further extensive spectroscopic surveys by Kraft (1962, 1964) showed that all CVs are close binaries transferring mass from a main sequence companion star to a white dwarf. The classification of these 'nova' stars then arose from the morphology (amplitude and duration) of their outbursts in the following scheme.

Systems which have had one outburst only, such as DQ Her (Walker 1954), were called the classical (or old) novae. Their outburst amplitudes, which can be up to ~ 20 mag, are strongly correlated with the rate at which the outburst fades, resulting in a further sub-classification of fast and slow novae. These outbursts are thought to arise as a result of thermonuclear runaways of the hydrogen rich material accreting onto the white dwarf primary.

Some systems have been observed to have recurrent outbursts on the timescale of decades and hence have been given the classification of recurrent novae. Their outburst amplitudes are generally smaller than classical novae but in common with novae they eject a substantial shell of material at high velocities.

Dwarf nova outbursts are smaller in amplitude and occur more frequently than in recurrent novae. However, their outbursts are thought to arise as a result of temporary enhanced mass transfer through an ac-

cretion disc around the white dwarf. Based on the morphology of their outburst light curve, dwarf novae are further subdivided into Z Cam, SU UMa, and U Gem stars.

Nova-like objects are so called because they have similar spectral characteristics to classical novae but have never been observed in outburst. This may be because of the timescales over which they have been observed are short compared to an outburst timescale.

Finally there are the magnetic cataclysmic variables (MCVs), so called because the white dwarf primary in these systems has a magnetic field ($\geq 1 MG$). Depending on its strength, the magnetic field can partially or totally disrupt the formation of an accretion disc around the primary. The MCVs are further subdivided into the higher field polars or AM Her systems and the lower field intermediate polars (IPs). Some MCVs have also been classical novae (eg DQ Her, V1500 Cyg).

1.2   The structure of cataclysmic variables

The gravitational and rotational potential of a binary star system can be described by equipotential surfaces (Figure 1.1). Within a critical radius, the equipotential surfaces enclose one or the other of the stellar component of the binary. Beyond this critical radius the equipotential surfaces enclose both stars. At the critical potential (the Roche surface), the two equipotential lobes from the two stars come into contact at the Inner Lagrangian point (L_1). The relative sizes of the lobes are defined by the ratio of the stars' masses only, with the most massive star having the larger Roche surface. The scale of the system is determined only by the separa-
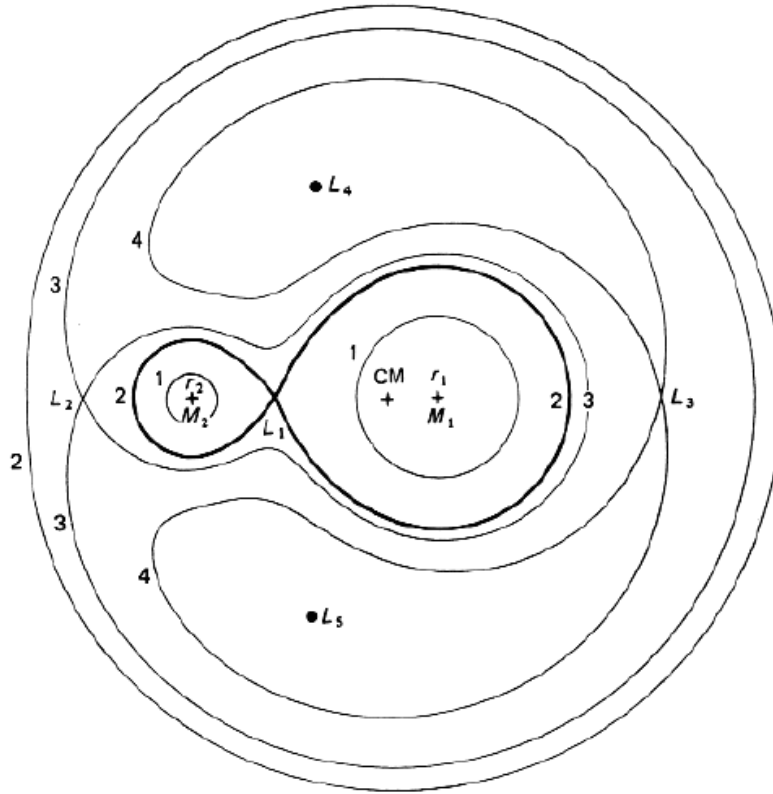
Figure 1.1: Section through the orbital plane showing Roche equipotentials for a binary system with mass ratio $q = M_2/M_1 = 0.2$. L_1–L_5 are the Lagrangian points and CM is the centre of mass. The equipotentials labelled 1–4 are of increasing potential with surface 2 being the Roche surface. From Frank, King & Raine (1985).

tion of the two stars.

Detached binaries are those systems in which neither star fill their Roche lobes. If both stars fill their Roche lobes then the system is said to be a contact binary. When only one of the stars fills its Roche lobe the system is semi-detached.

CVs are semidetached systems in which the more massive star (the primary) is a white dwarf. The secondary is a late type star, usually near the Main Sequence, which is tidally distorted and fills its Roche lobe. At the L_1 point the net force is zero, allowing the material at the L_1 point to overflow into the primary Roche lobe. For this mass transfer process to continue the secondary must expand on an evolutionary timescale as its mass is depleted, or the Roche lobe itself must contract. However, systems with orbital periods less than ~ 9 hr, are not in a state of evolutionary expansion (Patterson 1984). Most CVs have orbital periods less than 9 hr and therefore the Roche lobe radii must be decreasing in order to maintain mass transfer. Thus, the system is continually losing angular momentum and the system separation is decreasing.

Two mechanisms of angular momentum loss have been proposed. For systems with periods less than ~ 3 hr, the principle mechanism is the emission of gravitational radiation. In the case of the longer period systems, magnetic stellar-wind braking is the main candidate (see Lamb & Melia 1986).

As a result of the rotation of the binary system, material overflowing into the primary's Roche lobe will have to loose large amounts of angular momentum before it can accrete onto the white dwarf. The overflowing material forms a stream which in the absence of a strong white dwarf

magnetic field, orbits the white dwarf elliptically before interacting with itself. In this interaction kinetic energy is dissipated by the material, resulting in the formation of a ring. The accreting material must then loose angular momentum in order to decrease its radius from the white dwarf. The energy is dissipated by various viscous interactions such as turbulent and ion-ion viscosity, and localised magnetic fields (see Katz 1985). The orbiting gas then spirals inwards while the angular momentum is transferred to the outer region of the ring causing it to expand outwards, thus forming a disc. It is this disc that is responsible for the doubled Balmer emission lines seen in non–magnetic CVs. The inflowing mass transfer stream from the secondary also interacts with the disc forming a 'bright spot' that is believed to be the cause of the 'S' wave feature seen in some of the more highly inclined systems.

In non-magnetic CVs the gas in the disc dissipates half of its potential energy in the disc. The remaining rotational kinetic energy is released in the boundary layer where the rapidly rotating disc material meets the more slowly rotating surface of the white dwarf. However, if the white dwarf possesses a strong magnetic field as in the MCVs, the magnetosphere will either truncate or prevent the formation of an accretion disc.

1.3   The Magnetic Cataclysmic Variables

The first direct observational evidence of a primary containing a magnetic field occurred in 1974 when DQ Her was shown to have spin-modulated circular and linear optical polarization (Swedlund, Kemp & Wolstencroft 1974; Kemp, Swedlund & Wolstencroft 1974). The peak to peak ampli-

tudes of the polarizations were 0.6% (circular) and 0.2% (linear). Then in 1977 circular and linear optical polarisation at peak to peak levels of $\sim 13\%$ and $\sim 6\%$ respectively were discovered in the nova like variable AM Her (Tapia 1977a; Stockman et al. 1977). This was interpreted as polarized cyclotron emission from material being funnelled along magnetic field lines onto the pole(s) of the white dwarf.

The presence of a strong magnetic field on the primary star in close binaries has substantial implications for the understanding of the accretion processes in CVs.

1.3.1 Polars: AM Herculis stars

The star AM Her was originally discovered in 1924 and listed as a nova–like because of its variations in brightness and its emission line spectrum. It was also later suggested that AM Her could be the optical counterpart of the Uhuru X–ray source 3U 1809+50 (Berg & Duthie 1977). Later spectra and X–ray observations revealed a 3.09 h orbital period (Hearn et al. 1976, Cowley & Crampton 1977). This orbital period was also discovered in the linear and circular polarization at optical wavelengths, leading Tapia (1977a) to suggest the presence of a strong magnetic field. The magnetic field strength had to be very high to produce optical polarization and could be located only on the white dwarf primary. Because periods for the polarization, X–ray, and spectroscopic variations were equal, this indicated that the white dwarf must rotate at the same rate as the orbital motion, making it phase-locked in the reference frame of the binary.

The search for polarization was then extended to the other known nova–

likes. This resulted in the rapid discovery of two more AM Her–like systems which were also later discovered to be X–ray emitters (AN UMa: Krzeminski & Serkowski 1977, who also introduced the term polars; and VV Pup: Tapia 1977b). Besides the optical polarisation, the other defining characteristic of these objects is that the X-rays, UV, optical, the infrared band light curves and the radial velocity curves of the emission lines are all modulated on the same period. They also exhibit high ratios of soft–to–hard X–ray luminosity and high excitation optical spectra with prominent HeII 4686 emission lines.

There are now of ~ 50 polars. A list is given in table 1.1: Most have come from the optical identification of sources discovered in X–ray surveys. Also listed are their orbital periods, magnetic field strengths (when known), inclinations and magnetic field dipole offset angles (when known).

Table 1.1: The main system parameters of the currently known (or probable) AM Her systems.

Name	P_{orb} (min)	V mag	Distance (pc)	B (MG)	i (^{o})	β (^{o})	RA (2000.0)	Dec (2000.0)
RX0132–65	77.8	∼20	>300	68			01 32 42	–65 54 32
RX0153–59	∼80	∼15					01 54 02	–59 47 39
BL Hyi	113.6	15–19	128	33	70±10	153±10	01 41 01.1	–67 53 24
RX0203+29	275.5	∼17					02 03 48	+29 59
WW Hor	114.6	17–21	430	25			02 36 11.5	–52 19 14
EF Eri	81.0	13–15	≳ 89	10	58±12	27±18	03 14 12.9	–22 35 41
EXO0329–26	228.4	∼17		(10–50)			03 32 4.8	–25 56 49
UZ For	126.5	17–20.5	250	53,(75)	81±3	150±12	03 35 28.6	–25 44 22
RE0453–42	∼95	∼19					04 53 24.1	–42 14 07
RE0501–03	∼80	∼15					05 01	–03
RX0515+01	479.0[1]	∼14	∼500	30–55			05 15 42	+01 04 40
RE0531–46[2]	133.0	∼17	∼300	∼19			05 31 35.8	–46 24 07
BY Cam	199.3	15–17		41			05 42 49.0	+60 51 28
VV Pup	100.4	14–17	145	31.5,56	76±6	152±6	08 15 6.8	–19 03 16
EU Cnc	125.4	20–21	750				08 51 27.4	+11 46 57
RX0929–2404 [3]	203.4	∼17	∼830	42	80		09 29 07	–24 04 56
RX1002–19	107	∼17					10 02 11.4	–19 25 34
RX1007–20	∼208	∼18					10 07 34.4	–20 17 31
RX1015+09	79.9	∼17					10 15 30	+09 04
WGA 1047+63	80	19					10 47 9.9	+63 35 13
EK UMa	114.5	18–20	≳400	47	56±19	56±19	10 51 35.2	+54 04 37
AN UMa	114.8	14–19	≳ 270	36	65±5	20±5	11 04 25.9	+45 03 15
ST LMi	113.9	15–17	128	18	64±5	141±4	11 05 39.3	+25 06 29
AN UMa	115.9	13–17	88	230			11 15 47	+42 58 50
DP Leo	89.8	17–19	≳ 380	31,59	76±10	103±5	11 17 16.0	+17 57 41
RE1149+28	∼90	∼17					11 49 54.6	+28 45 12
RE1307+535 [4]	∼80	∼17	>705	30–40			13 07 56.4	+53 51 37
RX1313–32	∼252	∼16					13 13 18	–32 59
V834 Cen	101.5	15–16	86	23	45±9	25±5	14 09 7.5	–45 17 17
EUVE 1429	286	16	270		∼85		14 29 27	–38 04 10
MR Ser	113.6	15–17	139±12	24	43±5	38±5	15 52 47.4	+18 56 26
V2301 Oph [5]	112.97	∼16					18 00 35.5	+08 10 12.8
RE1802+18	113	∼14					18 02 6	+18 04 48
AM Her	185.6	12–16	75	14,28	30±5	61±5	18 16 13.3	+49 05 23
RE1844–74[5]	∼90	∼18					18 44 42.2	–74 18 39
EP Dra [6]	104.6	∼18	≳ 300	16	∼80	∼18	19 07 06.3	+69 08 39.8
RE1938–46 [7,8]	∼140	∼15		56			19 38 35.7	–46 12 49
RE1940–10 [9]	202.2						19 40 11.5	–10 25 25.7
RX1957–57	99	∼18	∼350	16			19 57 11.5	–57 38 22
QQ Vul	222.5	15–17	≳ 400	(10–50)	60±14	±19±9	20 05 40.7	+22 40 06
Drissen V211b [10]	∼160	∼18					20 08 56.6	–65 27 22
RX2022–39	78.0	19	>190	67			20 22 37.5	–39 54 13
RE2107–05 [11,12]	125.0	∼15	>200	36	80±5	40±10	21 07 58.3	–05 17 39
V1500 Cyg	201.0	∼17	∼1200	(20),(20)			21 11 36.5	+48 09 02
EUVE 2115–586	110	18	>250	11			21 15 41.0	–58 39 48
CE Gru	108.6	18–21		(25-50)			21 37 56.6	–43 42 14
RX2316–05	∼209	∼18					23 16 2.4	–05 27

Notes to table 1.1 For systems discovered prior to the *ROSAT* mission, the majority of data has been taken from Cropper (1990). For the post *ROSAT* systems, data has mainly been taken from Ritter & Kolb (1994), Beuermann & Thomas (1993), Beuermann & Schwope (1993) and Kolb & de Kool (1994). The magnetic field strength show the fields for the primary and secondary accretion poles respectively if known (Chanmugam 1992). Poorly determined field strengths are shown in brackets. From Ramsay (private communication).

(1) Garnavich, P. M., Szkody, P., Robb, R. M., Zurek, D. R., Hoard, D. W., 1994, ApJ, 435, L141

(2) Reinsch, K., Burwitz, V., Beuermann, K., Schwope, A. D., Thomas, H.-C., 1994, A&A, 291, L27

(3) Sekiguchi, K., Nakada, Y. & Basset, B., 1994, MNRAS, 266, L51

(4) Osborne et al. 1994, MNRAS, 270, 650

(5) O'Donoghue, D., Mason, K. O., Chen, A., Watson, M. G., 1993, MNRAS, 265, 545

(6) Remillard, R. A., Stroözas, B. A., Tapia, S. & Silber, A., 1991, ApJ, 379, 715

(7) Buckley, D. A. H. et al. 1993 MNRAS, 262, 9

(8) Ferrario, L., et al. 1994, MNRAS, 268, 128

(9) Staubert, R. et al. 1994, A&A, 288, 513

(10) Wickramasinghe, D. T., et al. 1993, MNRAS, 265, L29

(11) Schwope, A. D., Thomas, H.-C. & Beuermann, K., 1993, A&A, 271, L25

(12) Glenn et al. 1994, ApJ, 424, 967

1.3.2   The Fundamental Properties of MCVs

In this section I will give a general outline of the basic model for the AM Her stars and then describe in greater detail the various regions that are responsible for the rich variety of observations. Most of the detail de-

scribed here will also be relevant to the intermediate polars: those aspects which are different will be discussed later.

The accretion stream

Unlike the non–magnetic CVs, the magnetic field of the white dwarf is large enough to prevent the formation of an accretion disc. Instead the material leaving the L_1 point flows in the form of a narrow stream. At some point the magnetic energy density of the white dwarf begins to dominate the ram pressure of the stream at the magnetosphere. Once the material reaches the magnetospheric boundary, it is threaded by the field lines and thereafter is forced to flow along the field lines to the magnetic poles on the surface of the white dwarf. This may occur immediately after the L_1 point or the stream may travel on a ballistic trajectory for some distance before connecting to the field lines. The actual location of the region (at the equilibrium radius r_μ) is given by the balance of the ram pressure of the stream, the magnetic energy density B given by $B^2/8\pi \geq \rho v^2$, where ρ and v are the density and velocity of the stream respectively, and the orientation and geometry of the white dwarf's magnetic field. The stream therefore consists of two components: a ballistic part and a magnetically funnelled stream after the threading region.

The gas in the stream is ionized by collisions and photoionized by UV and X–ray photons from the accretion region on the white dwarf. Thus, the stream is the source of multi–component, asymmetric and variable Balmer and helium emission lines, ideal for Doppler mapping (Horne 1991).

The stream is also responsible for the absorption dips seen in the IR, optical and X–ray light curves observed in systems with high enough in-

clination. These occur when the accretion stream crosses the line of sight between the observer and the accretion spot hence causing absorption features. At X–ray wavelengths this is due to photoelectric absorption and free–free absorption in the optical. An analysis of data containing dips was given by Watson (1995). In eclipsing polars the stream can be seen as a distinct source of continuum light during ingress and egress. Schwope (1995a) and Hakala (1995) provide an analysis of the eclipsing polar HU Aqr which displays all the above features and Schwope (1995b) provides a discussion on accretion streams.

Mukai (1988) showed that in general for polars with an orbital period $P_{orb} < 2h$ the equilibrium radius r_μ is larger than the radius to the inner Lagrangian point (R_{L_1}) and $r_\mu < R_{L_1}$ for $P_{orb} > 2h$. In systems where $r_\mu < R_{L_1}$ the material leaving the L_1 point will accelerate and decrease in density by up to a factor of 30. It will also start feeling the influence of the magnetic field. The magnetic pressure will start to increase until it exceeds the thermal pressure of the gas. This occurs before r_μ and determines the shape and density of the stream, but not its trajectory. The stream probably has a denser core than its periphery so that the effect of the magnetic pressure is felt most in its outer parts (Mukai 1988). In a detailed discussion, Hameury, King & Losata (1986), suggest that the magnetic pressure continues to increase at a faster rate than the gas can adjust subsonically. As a result, the stream shatters into small fragments. The physics of the accretion stream and its interaction with the magnetic field at this point becomes very complex and their state is subject to several plasma–physical instabilities such as the Rayleigh–Taylor and Kelvin–Helmholtz instabilities.

The Rayleigh–Taylor instability arises from the opposition of the magnetic field to the stream resulting in the formation of large blobs which are only slowly penetrated by the magnetic field. The blobs are compressed even more by the continual increase in the magnetic pressure. At the same time the Kelvin–Helmholtz instability acts across the density gradient in the blobs stripping their surfaces of smaller drops which are more readily penetrated by the magnetic field. Liebert & Stockman (1985) and Lamb (1985) suggest that the larger blobs are shock heated and constantly ablated by the now confined smaller droplets moving almost perpendicularly at supersonic velocities.

The gas that survives the instabilities is thought to arrive at r_μ in the form of small blobs ($< 10^8$ cm) and possibly some larger blobs which thread onto the magnetic field lines. Some even larger blobs may also have survived and penetrated the field even further before becoming threaded. The threading region will therefore be extended in azimuth with the larger, least readily threaded blobs falling last to the surface. Once threaded, the field redirects the stream to follow the magnetic field lines down towards the surface of the white dwarf where the material passes through a shock and then settles through the post shock region onto the surface on the white dwarf (figure 1.2).

Accretion onto the white dwarf

As first pointed out by Lamb (1985) and from computations by Mukai (1988), an extended threading region will result in the stream impacting on the surface of the white dwarf in the form of arcs displaced from the primary's magnetic pole. The manner in which the blobs were threaded

Magnetic field line

SHOCK

Hard X-rays

Hot subsonic
settling flow

Soft X-rays
and UV

White dwarf
photosphere
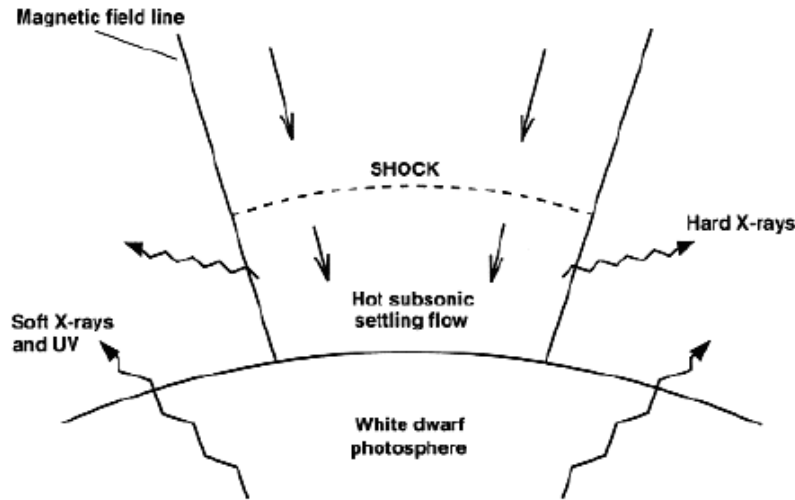
Figure 1.2: Schematic of a homogenous accretion column. From Watson (1986)

in the threading region governs the location, shape and the physical conditions along the arc. For any one particular system, the location and structure of the threading region will depend on the strength, geometry and orientation of the primary's magnetic field and on the mass accretion rate. This is borne out by the large differences in observational characteristics of polars. The situation is further complicated in that systems that are very similar can be observed to be very different because of their differing inclinations (the angle at which the binary plane is viewed).

The gas falling supersonically along the field lines impacts with the photosphere of the primary, producing a shock front. The easiest accretion geometry is to assume a radial, one dimensional, uniform density flow before encountering the surface. The flow decelerates by a factor ~ 4
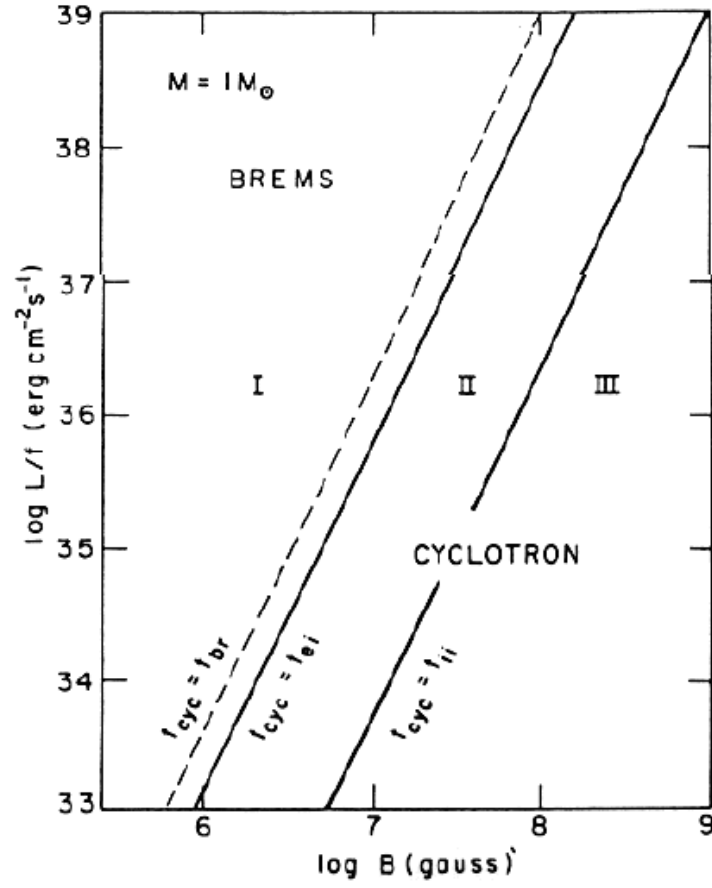
Figure 1.3: The cooling regimes in the B–$\log L/f$ plane for a one solar mass white dwarf. From Lamb & Masters (1979)

as it passes through the shock and then cools as it settles on to the surface (figure 1.2).

The height of the shock is then determined by the efficiency of the cooling mechanisms acting on the gas below the shock. The temperature immediately behind the shock is given by

$$T_s = \frac{3}{8}\frac{GM\mu m_H}{kR}$$

(Frank, King & Raine 1985). For typical white dwarf parameters this will give $T_s \sim$ a few $10^8 K$. Thus the primary emission from the shocked inflow is X–rays at $\sim 10 - 20$ keV in the form of bremsstrahlung (free–free) emission mostly from the denser and cooler base of the flow. In some regimes, for example at high fields and low specific accretion rates, cyclotron cooling by semi-relativistic electrons spiralling around the magnetic field lines may begin to dominate over bremsstrahlung. Such a region must be present to account for the phase–dependent cyclotron emission observed in many AM Her systems. The relative importance of the two cooling mechanisms depends on the conditions in the post–shock region, especially on the magnetic field strength B and on the specific accretion rate (accretion rate per unit area L/f, where L is the luminosity proportional to the accretion rate, f is the fraction of the white dwarf's surface covered by the column). Compton cooling through the scattering of the relatively lower energy photons by the shocked electrons will also contribute to the cooling of the gas. Figure 1.3 shows the regimes in the B–$\log L/f$ plane in which the different cooling mechanisms dominate, produced by Lamb & Masters (1979).

These homogeneous (uniform) column models predict that the emitted radiation spectrum has three components. The highest energy com-

ponent is hard X–ray bremsstrahlung, emitted from the post shock flow in the column, which is optically thin to hard X–rays, half which will escape into space, with the other half directed towards the white dwarf surface. This is mostly reflected for $E \gtrsim 30 \text{keV}$ but absorbed for lower energies, which are thermalized and remitted as an approximately blackbody spectrum in the UV or soft X–ray region with $kT_{BB} \sim 40eV$ (Milgrom & Salpeter 1975) to produce the second component. The third component is the cyclotron emission, mentioned above, from the column at optical wavelengths. This is optically thick for low harmonics and optically thin for higher ones (see chapter 2).

However, the luminosity balance ($L_{hard} \gtrsim L_{soft}$) predicted by these basic radial, homogeneous column models did not agree with observations. Ramsay et al. (1994) reported that at least 12 AM Her systems out of a sample of 16 violate this approximation relation. Other authors (e.g Beuermann 1995) reported soft–to– hard ratios of 50 or more in some individual systems. This came to be known as the soft X–ray excess in AM Hers.

Kuijpers & Pringle (1982) were the first to suggest that inhomogeneous flow might be an explanation for the soft X–ray excess. Frank et al (1988) used this basic idea of inhomogeneous flow and showed that a soft X–ray excess is expected provided the flow is broken up. The treatment by Frank et al (1988) is complex; however the result lies in that a soft X–ray excess can be achieved from having several 'buried' shocks sufficiently far apart that they can be regarded as independent. The total emission can be obtained from summing the contributions from each shock (figure 1.4). The emergent radiation must make its way through a

substantial optical depth, thereby degrading most of it to soft X–rays.

This led King (1995) to propose three characteristic scales for the highly inhomogeneous accretion region in polars (figure 1.5). These are: f_{acc}, the area over which blobs accrete, f_{eff}, the area over which the photosphere around each accreting blob emits soft X–rays and f_{zone}, the region over which the blobs accrete, so that $f_{acc} << f_{eff} < f_{zone}$.

However, AM Her systems do emit hard X–rays, and all produce cyclotron radiation to some degree. Therefore, the model of King (1995) still requires a fraction of the gas accreting with the dense blobs to shock above the white dwarf's surface, producing hard X–rays and cyclotron emission. The irradiation of the white dwarf's surface will add soft X–rays to those emitted from the blob accretion.

Magnetic fields

The magnetic field strengths of the white dwarfs in AM Her stars has been determined using three different methods. The method used depends on several factors, namely the actual strength of the magnetic field, whether the system is in a high or low state and on the quality of the observations.

Cyclotron emission features were first seen in VV Pup by Visvanathan and Wickramasinghe (1979) in the form of a series of broad humps in the spectrum. These correspond to the harmonics of the cyclotron frequency (see chapter 2), the spacing of which is directly related to the magnetic field in the cyclotron emitting region. This method can also be applied to low field systems by observing in the near IR.

During the faint state the photosphere of the white dwarf can be a

photosphere

WD atmosphere

z

D

z

d
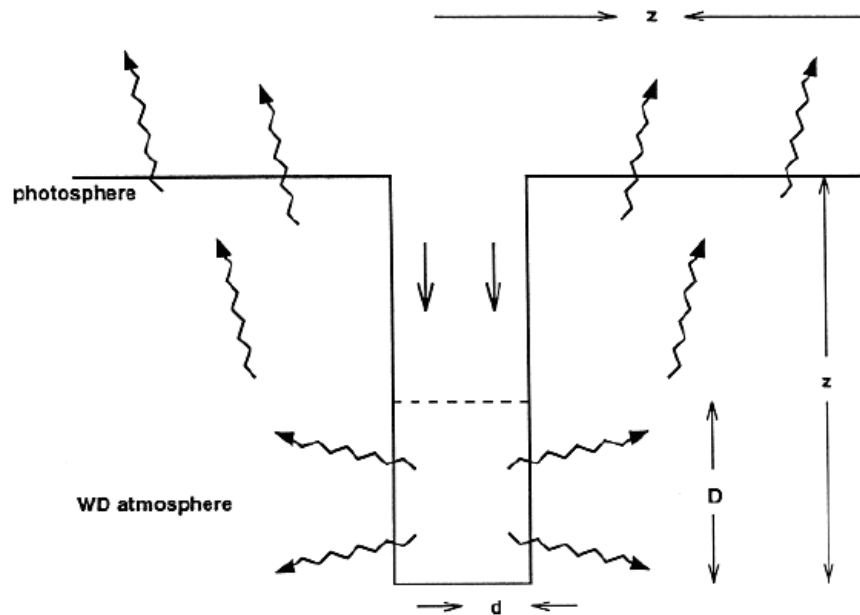
Figure 1.4: Schematic view of a buried shock producing a soft X–ray excess if $d < D < z$. Adopted from King (1995)
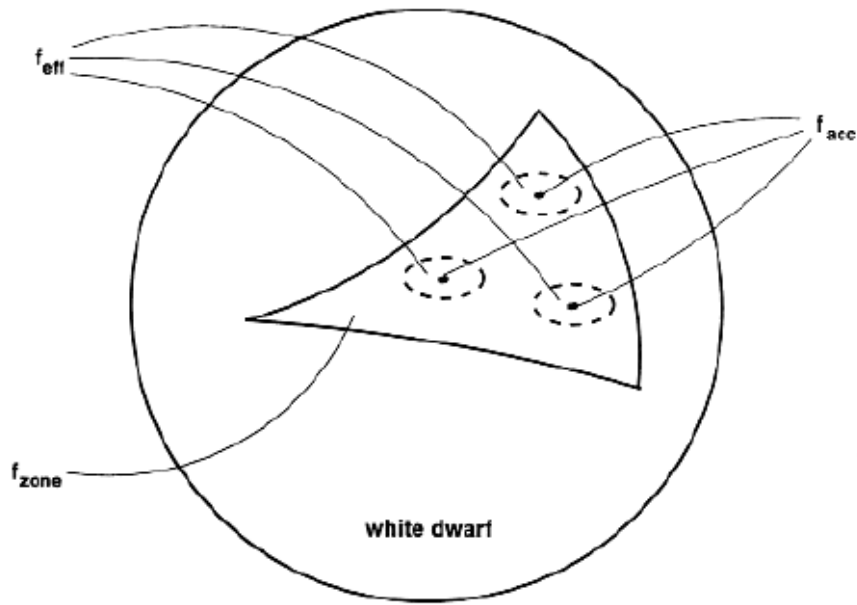
Figure 1.5: Schematic view of the three fractional areas f_{acc}, f_{eff} and f_{zone} over which highly inhomogeneous accretion occurs (see text). Adopted from King (1995)

significant component to the total light. During this state, Zeeman splitting can be seen in the hydrogen lines and also polarization features (e.g. Schmidt, Stockman & Margon, 1981). The wavelengths and profiles of the Zeeman components allows the field to be calculated in a flux–weighted fashion.

Also, during a bright state, non-photospheric (or halo) Zeeman features can be seen. These have been interpreted as being due to cool gas seen in absorption against the cyclotron emission.

Only two systems (V834 Cen and MR Ser) have had their field strengths measured using all three methods. The cyclotron and halo Zeeman measurements agree, as expected, because they both measure the field of the cyclotron emission. An analysis of the photospheric Zeeman features has a lower value, as expected because it reflects the flux–weighted average field over the whole visible white dwarf.

1.3.3   Intermediate Polars

These systems resemble the Polars in that they are characterised by strong X–ray emission, high excitation spectra and have very stable pulsations in their optical and X–ray light curves. However, they differ in two respects: IPs have little or no observed polarization, but more importantly, the primary in IPs rotate asynchronously with the orbital period. The asynchronism is an indication that either the braking torque is insufficient to produce synchronism or an event or process occurred that broke synchronism. For example, a nova explosion or a period of exceptionally high accretion rate may have pushed it out of synchronism, or it may simply be in the process of being synchronised for the first time.

Table 1.2: The known IPs. Adopted from Warner (1995).

Star	Alias	P_{orb} (h)	m_v	$P_{rot}(1)$ (s)	$\dot{P}_{rot}(1)$ $\times 10^{-11}$	P_{syn} (s)	$i°$
EX Hya	4U1228-29	1.633	13.5	4021.61 OX	-3.8 ± 0.2		78
RXJ1712.6-2414		2.65 or 3.41	14.2	927 O		1003/10270 O	
BG CMi	3A0729+103	3.235	14.8	913.49 X	5.7 ± 0.6	913.49 OX	30:
V1223 Sgr	4U1849-31	3.366	13.0->16.8	745.43 X	2.3 ± 0.3	794.38 OX	<40
AO Psc	H2252-035	3.591	13.2-15.3	805.4 XO	-6.6 ± 1.0	858.69 OX:	60:
YY Dra	3A1148+719	3.910	16.0	529.2 X	<21	550 O	42
FO Aqr	H2215-086	4.849	13.0-13.8	1254.45 OX	3.4 ± 0.4	1373 OX	70 ± 5
PQ Gem	RE0751+14	5.18	14.5	833.37 XO		872 O	low?
TV Col	2A0526-328	5.487	13.8	1910 OX			70:
TX Col	1H0542-407	5.718	15.7	1910.5 X		2106 OX	25:
XY Ari	1H0253+193	6.06	K=13.5	206.30 X			>70
V1062 Tau	1H0459+248	9.952	15.6	3720 OX		3720 OX	
GK Per	A0327+43	47.923	13	351.34 X	-2.5:	351.3 O	65

Table 1.2 lists the known IPs and their main characteristics. The white dwarf rotational periods range from 33 s to 2.0 hr. The white dwarfs' magnetic moments are slightly weaker than those of the polars, but with some overlap.

A consequence of the asynchronously rotating primary is that the accretion region produces a beam which can illuminate other structures in the system. Subsequently, orbital, spin, beat (the beat frequency between the orbital and spin frequencies) and their sideband periods are observed to greater or lesser degrees from system to system.

Modes of accretion

As a consequence of the rotating weaker magnetic fields in IPs, there are two modes of mass transfer onto the primaries. If the magnetic moment μ of the primary is too small to prevent the formation of a disc then magnetically controlled accretion will take place from the inner edge of the disc. If μ is sufficient to prevent the formation of a disc then the process of mass transfer is governed by the location of the threading region(s). In both cases the process is time-dependent, three–dimensional and non–axisymmetric.

Ghosh & Lamb (1978, 1979a,b) laid the foundations for the understanding of the interaction between the magnetic field of the primary and the disc in the first case. Figure 1.6 shows a cross–section of their model. The disc is assumed to be constructed of an homogeneous diamagnetic plasma which prevents the penetration of any magnetic field. However, four methods of penetration of the disc have been recognised. Firstly, the kinetic energy of the convective and turbulent motions, can exceed
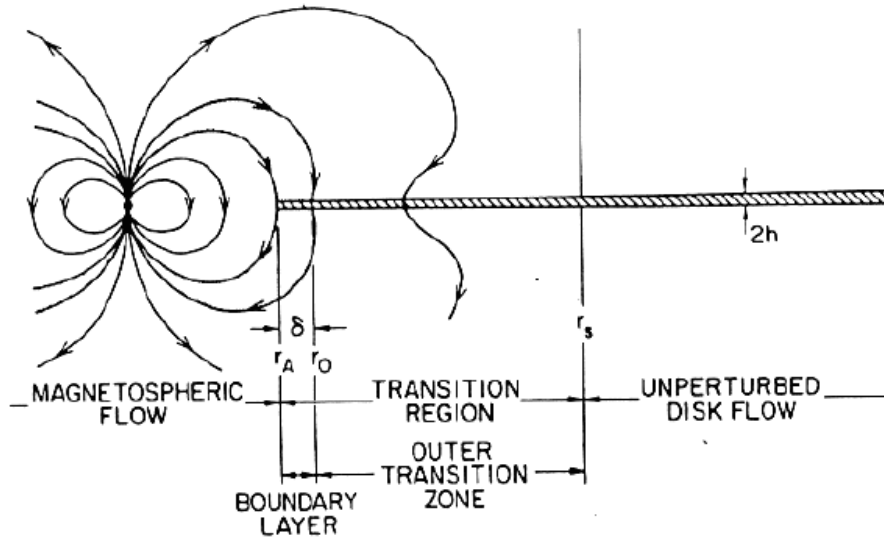
Figure 1.6: A schematic view of the interaction between the accretion disc and the magnetic field of the primary. From Ghosh & Lamb (1978)

the magnetic energy density at the surface of the disc allowing the field to penetrate. Then there is the Kelvin–Helmholtz instability which can grow and carry the field into the disc. The field could simply reconnect with the magnetic field lines of the disc. Finally Livio & Pringle (1992) also pointed out that the field could diffuse into the disc as a result of the magnetic or hydrodynamic processes that give rise to the disc kinematic viscosity.

As a result, the field will penetrate the disc within the region $r_0 < r < r_s$ (figure 1.6). In this region the disc will drag the field lines with it producing a torque on the primary. There is also a corotational radius r_{co} where the Keplerian and the primary angular velocities are equal. For $r > r_{co}$, the Keplerian angular velocity is less than that of the primary

and the field lines are dragged backwards causing the primary's rotation to slow down. If the primary rotates so slowly that $r_{co} > r_s$ then all the torque will act to spin up the primary. However, if $r_{co} < r_s$ then the change in rotational period is determined by the net torque.

Within $r_0 < r < r_s$ the magnetic field lines are dragged inwards until the boundary layer $r_A < r < r_0$ is reached. At this point the magnetic forces distort the gas flow to rotate at the corotation velocity. If, however, r_0 is significantly different from r_{co} then a considerable amount of angular momentum and energy will be dissipated within the boundary layer heating up the inner disc. The accretion regions on the surface of the white dwarf are then determined in the same way as for the polars described above, but larger and more extended accretion regions are expected.

In the second case, a disc is prevented from forming if the radius at which the gas attaches to the field lines is greater than the circularization radius. The details of the stream/magnetosphere interaction are even more complicated than that for the AM Her systems. Hameury, King & Lasota (1986b) and Wickramasinghe, Wu & Ferrario (1991) derived approximations for the threading radius and conditions for discless accretion respectively. However, the physical appearance of a discless, asynchronous rotator is difficult to envisage and is currently the matter of some debate.

Hameury, King & Lasota (1986b) envisaged a non–accreting disc around the primary that gives the appearance of an accretion disc and concluded that strong shocks would form in the threading region. Furthermore, the rapid motion of the field lines would lead to fragmentation of the stream resulting in a greater amount of clumpiness in the accreting gas than in

the polars. As a consequence, a higher amount of soft X–ray excess would be expected in IPs than in polars which is not observed. The standard explanation is that the high mass transfer rates and the larger accretion areas results in a greater amount of absorption within the system. However, Haberl & Motch (1995) recently identified a group of "soft–IPs" which are no nearer, and don't appear to be in any more favourable presentation, than any of the other IPs.

More insight into the physical appearance accretion flows in IPs has been made through theoretical modelling by King (1993) and Wynn & King (1995). They applied the work of Arons & Lea (1980) to IPs and found that blobs are not immediately forced to follow the magnetic field lines, but orbit the white dwarf several times before doing so. The blobs interact with the magnetosphere through surface drag, allowing the exchange of orbital energy and angular momentum between the blobs and the field. King (1993) showed that the timescale for this to occur was an order of magnitude longer than the dynamical timescale but much shorter than the viscous timescale on which an accretion disc can form by self–interaction. In this picture, the abrupt transition from ballistic trajectories to one confined by a magnetic field is replace by one in which the gas flows under gravity but is resisted by field drag.

Blob orbits and the spin evolution of the white dwarf were also studied by King (1993) and Wynn & King (1995), both analytically and numerically. A result is that the blobs were either accreted or ejected depending on the white dwarf spin period and the drag coefficient of the magnetic field. The result of the torques would then dictate an equilibrium spin period found to be ~ 0.1 of the orbital period. Wynn & King (1995) show that

once the white dwarf has attained spin equilibrium, the mass flow can be computed. Doppler tomograms and trailed spectra of the predicted flow can be produced thus providing tests for the model (Wynn & King 1995).

Lubow (1989) has also pointed out that an intermediate case can exist in which part of the stream can continue its trajectory over the surface of the disc until threading onto the magnetic field lines at r_0. This hybrid of disc and discless models has been investigated in observations by Hellier et al. (1993a,b).

See Hellier (1995) for an investigation of the accretion geometry in some well studied systems and Patterson (1994) for an extensive review of the IPs.

Chapter 2

Modelling the Cyclotron Radiation

The analysis of the polarized cyclotron emission has been one of the most valuable techniques for determining the structure of the accretion region in MCVs. This is because the observed polarized emission is very sensitive on the viewing angle to the magnetic field line that feeds the accretion region(s). Several authors therefore, have calculated the polarized emission from the postshock region. (See Wickramasinghe (1988) and Schwope (1990) for reviews of the modelling of the transfer of radiation through a standard accretion column). These calculations can then be used in conjunction with polarization data to model the structure of the accretion region (see for example Cropper 1985, Ferrario & Wickramasinghe 1990, Potter et al. 1997: chapter 3, Potter et al 1998: chapter 4, 5, 6).

This chapter describes a cyclotron emission model that I have developed and which is used throughout this thesis. I will begin by discussing

the nature of cyclotron radiation and the opacity calculations of Meggitt and Wickramasinghe (1982, MW82)) that are used by the model. The bulk of the chapter is then an investigation into the morphology of polarized light curves that are produced from different accretion scenarios (the shape and location of the cyclotron emitting region on the surface of the white dwarf).

2.1 Cyclotron radiation

Cyclotron radiation arises from non-relativistic particles accelerating in a magnetic field $\mathbf{B}$. Applying the Lorentz equation on an isolated charge q of mass m in a magnetic field gives

$$\mathbf{F} = \frac{q}{c}\mathbf{v} \times \mathbf{B} \qquad (2.1)$$

with $q\mathbf{v}\dot{\mathbf{E}} = 0$ implying that $|\mathbf{v}|$ is a constant. Therefore it follows that

$$m\gamma\frac{d\mathbf{v}}{dt} = \frac{q}{c}\mathbf{v} \times \mathbf{B}, \qquad (2.2)$$

where γ is the Lorentzian correction. Separating the velocity components along the magnetic field $\mathbf{v}_{\parallel}$ and in a plane normal to the magnetic field $\mathbf{v}_{\perp}$ will give

$$\frac{d\mathbf{v}_{\parallel}}{dt} = 0, \quad \frac{d\mathbf{v}_{\perp}}{dt} = \frac{q}{\gamma mc}\mathbf{v}_{\perp} \times \mathbf{B} \qquad (2.3)$$

which implies that $|\mathbf{v}_{\perp}|$ and $\mathbf{v}_{\parallel}$ are constant. This results in uniform circular motion of the projected motion on the normal plane. The combination of the circular motion and the constant uniform motion along the magnetic field is a helical motion of the particle.

An isolated electron will then gyrate with a gyration frequency of

$$\omega_o = \frac{e\mathbf{B}}{\gamma m_e c} \qquad (2.4)$$

and will emit radiation at all harmonics (i.e., integer multiples) of this fundamental frequency. Hence the energy of the electron affects the frequencies at which the radiation is emitted and also the distribution of the energy among the harmonics. i.e. the more energetic the electron the higher the harmonic at which the radiated power is emitted. The radiation will be in general elliptically polarized, becoming circularly polarized when emitted along the magnetic field lines and linearly polarized when emitted perpendicular to the magnetic field lines (see Drummond and Rosenbluth 1963). The intensity of the radiation is also dependent on the direction of the magnetic field and on the harmonic of the radiation. At high harmonics the anisotropy in the intensity is very pronounced with the radiation being restricted to a narrow beam centred on the orbital plane of the electrons circular motion. Near the fundamental frequency the anisotropy is less pronounced.

The emission from an ensemble of electrons will have a distribution of energies, making the harmonics broader. Low energy ($\gamma \simeq 1$) electrons will emit near the frequencies $n\omega_c$, while highly energetic ($\gamma \gg 1$) electrons will radiate at frequencies $n\omega_o = n\omega_c/\gamma \ll n\omega_c$. Ordinarily the line width due to this relativistic mass increase would be of the order of the square of the electron's thermal energy. However, the more energetic electrons emit preferentially at higher harmonics. Hence the higher harmonics will be broader than the lower ones and shifted towards lower frequencies (Fig. 2.1). The distribution of Doppler shifts of radiation from electrons moving toward and away from the observer is also an important
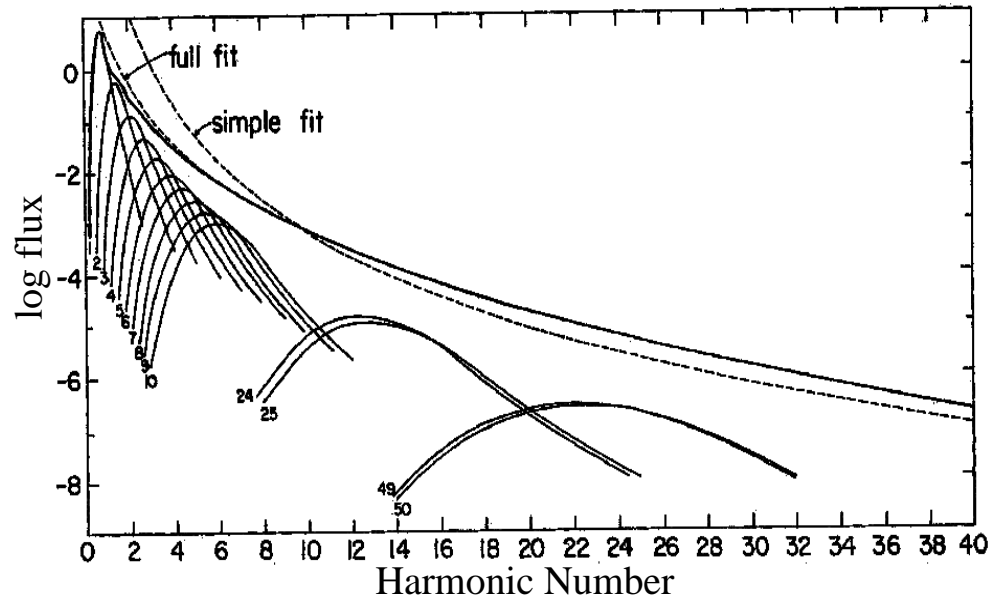
Figure 2.1: Distribution of energy amongst the harmonics for a viewing angle of $\alpha = 0.16$. Adapted from Masters (1978)

broadening mechanism at angles of $\alpha \neq 0°$ to the magnetic field. At high temperatures the broadening mechanism is partly compensated by the beaming of the radiation, most of the radiation being emitted in the direction of the motion. (Masters 1978, Meggitt and Wickramasinghe 1982).

2.1.1   Faraday mixing and cyclotron absorption

The discussion of MW82 continues with the addition of Faraday mixing and cyclotron absorption into their calculations. As mentioned above the radiation will in general be elliptically polarized, becoming circularly polarized when emitted along the magnetic field lines and linearly polarized when emitted perpendicular to the magnetic field lines. However as the physical depth s/s_o increases two mechanisms start to become impor-

tant. First, the Faraday mixing coefficients can change the ratio of linear to circular polarization. This plays an important role only if the Faraday mixing coefficients dominate over the cyclotron absorption coefficients, which are dependent on the physical depth. As a result for $\omega/\omega_c \geq 5$ the linear polarization is confined to angles near $\alpha = 90°$. At sufficiently low harmonics, large values of the opacity κ are encountered and the cyclotron absorption coefficients become comparable or even exceed the the Faraday mixing coefficients. When this happens the dominant effect is depolarization with Faraday mixing playing a minor role.

Secondly the total polarization decreases to zero as the intensity I_ω approaches the Plank function. i.e. one cannot have more intensity than given by the Plank function.

There is a third regime in which the optical depth can become large and can be described by the intensity approaching the Plank function and so does not vary with angle. In this regime the radiation is completely unpolarized.

All these effects give rise to a number of interesting conclusions. Firstly, as a result of their high opacity, the lower harmonics become depolarized at low optical depths without any appreciable Faraday mixing. Thus computations, such as those by MW82, of these low harmonics do not show the confinement of linear polarization around $\alpha = 90°$. For intermediate and high harmonics with a moderate path length of material, Faraday mixing confines the linear polarization to angles near $\alpha = 90°$. As the path length is increased the linear polarization gradually disappears as a result of depolarization. Opacity will also increase with temperature and so shorter path lengths are required to depolarize the radiation. However

opacity decreases greatly as the angle from the magnetic field approaches zero making it necessary for the path lengths to be larger to depolarize the radiation. As a result some circular polarization will persist in most circumstances.

2.1.2   Free-free opacity and scattering

The calculations of MW82 described above, did not include the effects of free- free opacity, such that the intensities and polarizations are specified completely by the electron temperature T_e, the angle α with respect to the direction of magnetic field, the dimensionless frequency ω/ω_c, and the optical depth parameter Λ given by

$$\Lambda = 2.01 \times 10^5 \left(\frac{s}{10^5 \, cm}\right) \left(\frac{N_e}{10^{16} cm^{-3}}\right) \left(\frac{3 \times 10^7 G}{B}\right) \tag{2.5}$$

in terms of the path length s, the electron number density N_e, and the magnetic field B. Wickramasinghe & Meggitt (1985) (WM85) went on to include the effects of free-free opacity as a pure absorption process into their calculations. Other authors such as Pavlov et al. (1980), included collisions into their cyclotron opacity. However this formalism allows the total opacity to be calculated only in the non-relativistic regime. For the high temperature systems that I am interested in here, relativistic effects will need to be taken into account. MW82 included relativistic effects in their calculations of the cyclotron absorption component. WM85 were therefore able to present calculations for a large region of parameter space for $T_e, N_e, \Lambda, \omega/\omega_c$ and α. This time N_e has to be specified in addition to Λ since free-free opacity has been included.

WM85 decided not to include the difficult problem of electron scat-

tering into their radiative transfer calculations. They reasoned that the large variation in the optical depths of electron scattering τ_{es}, free-free opacity τ_{ff} and cyclotron opacity τ_{cyc}, with viewing angle, shows that scattering cannot be dominant. They therefore assumed $\tau_{es} \ll 1$.

The results of their calculations can be seen in figure 2.2 and can be understood as the combination of several main effects. As stated above from MW82, for a given angle α, the cyclotron opacity decreases with increase in the harmonic number at the harmonic peaks. At lower temperatures the cyclotron opacity shows structure, with local maxima occurring at the harmonic peaks. Free-free opacity dominates at the higher frequencies where the cyclotron opacity is small and in between harmonics for the lower temperatures. It also dominates as α approaches zero. In regions where the cyclotron opacity is low, the intensity and polarization characteristics are those of optically thin free-free radiation.

To summarise, the diagrams in figure 2.2, taken from WM85, can be divided into three basic regions. The lower right hand corner of each diagram corresponds to where the intensity spectrum is blackbody–like, showing no variation with angle and zero polarization. This is the optically thick region. The marginally optically thick region, running from the bottom left to the top right hand side of each diagram, is characterised by high values of circular polarization and intensity. Finally the top left hand corner of each diagram is where the cyclotron opacity is very small and free-free opacity dominates. Here the polarization and the intensity are low (see WM85 for a more detailed description).
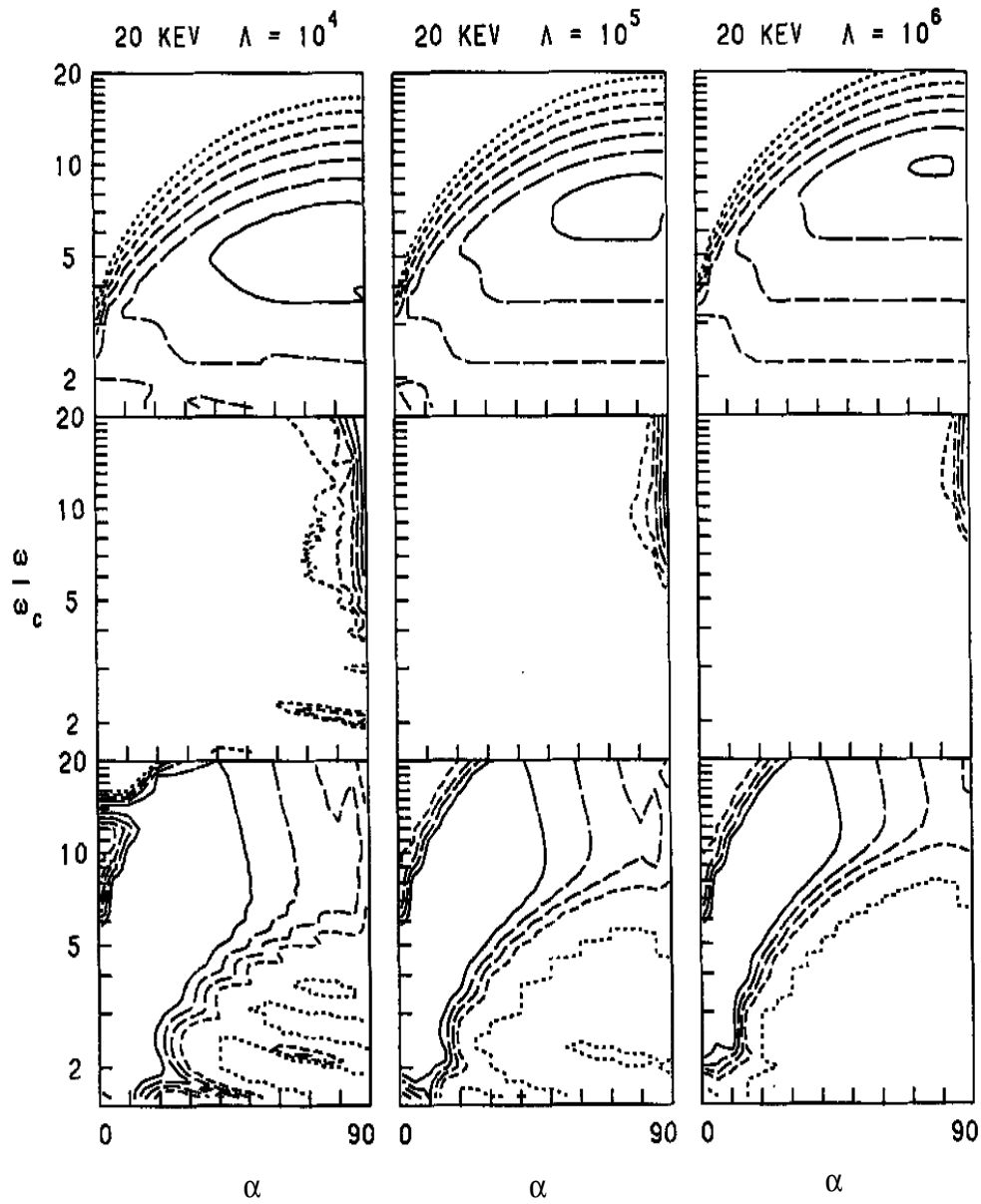
Figure 2.2: Grid of calculations. Top row:Intensity, Middle row:Circular polarization, Bottom row:Linear polarization. Larger dashes correspond to larger values. Adapted from WM85.

2.2 The Models

The first stage in modelling cyclotron emission is to calculate the viewing angle i.e. the angle between the line of sight and the magnetic field line where the emission emanates. I have achieved this by using a dipole magnetic field formalism as described in Cropper 1989. The dipole magnetic field can be parameterised by

$$\mathbf{r}(x, y, z) = r_0 \sin^2 \theta (\sin \theta \cos \psi, \sin \theta \sin \psi, \cos \theta) \tag{2.6}$$

where x, y, z and r, θ, ψ are the Cartesian and spherical polar components in the magnetic field reference frame respectively. The viewing angle to a specific emission point can then be calculated by first calculating the gradient of the magnetic field line at the emission point using

$$\frac{d\mathbf{r}(x, y, z)}{d\theta} = r_0 (3 \sin^2 \theta \cos \theta \cos \psi, 3 \sin^2 \theta \cos \theta \sin \psi, 2 \sin \theta \cos^2 \theta - \sin^3 \theta)$$

$$\tag{2.7}$$

and then rotating this vector into the frame of the white dwarf. This vector is then rotated as the white dwarf rotates. Finally the viewing angle is calculated by rotating this vector into the viewer's frame. The magnetic dipole is offset from the spin axis of the white dwarf by an angle β and the whole system is inclined with respect to the viewer by an angle i (the inclination).

In constructing the models I have assumed constant electron temperature, T_e, electron number density, N_e, and radial thickness of the emission region above the surface of the white dwarf. The height of the emission region is assumed to be a very small fraction of the white dwarf's radius. The value of the optical depth parameter changes across the emission region because of changes in the magnetic field strength (assuming a dipole

Figure 2.3: Diagram of angles. θ, ψ, β and ϕ are the magnetic latitude, magnetic longitude, dipole offset angle and the phase respectively.
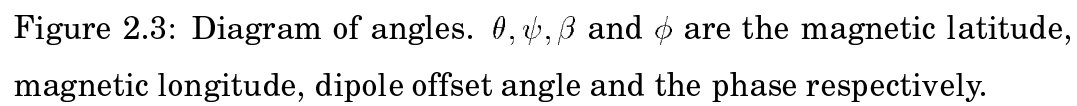
magnetic field), given by

$$B = \frac{B_0}{2} \left(\frac{R}{r}\right)^3 \left[3\cos^2\theta + 1\right]^{1/2} \tag{2.8}$$

and is characterised by equation (2.5). The magnetic field is assumed to be an incline dipole. However, in the chapters to follow the magnetic field strength is allowed to vary between the two poles. This allows a first order approximation to offset dipoles. As described above, the effects of cyclotron and free-free opacities are included in the grid of calculations.

Having calculated the viewing angle, local magnetic field strength and hence the local value for Λ, the calculations of WM85 can then be interpolated to give the intensity, percentage of circular and linear polarization and the position angle of linear polarization for an emission point. For extended emission the Stokes parameters are calculated for each point along the region and averaged as a function of phase. The complete radiative transfer through the shock structure is not carried out. As a first order approximation, a $cos(\theta)$ term is included to simulate absorption along the shock.

In the convention used here, the magnetic latitude of an emission point (θ) is measured from the magnetic pole in the hemisphere most pointing towards the observer. Therefore the magnetic equator is at a magnetic latitude of $\theta = 90°$ and the magnetic pole in the hemisphere pointing away from the observer is at a magnetic latitude of $\theta = 180°$. The magnetic longitude of the emission point (ψ) is measured in an anticlockwise direction from the line joining the magnetic pole and the spin pole of the white dwarf as it rotates in a clockwise direction (see figure 2.3).

2.2.1   Point source emission

Before analysing polarization data from systems such as IPs, it is impor-
tant to gain an understanding of the dependence of cyclotron radiation
with viewing angle and thus spin phase in IPs. In figure 2.4 I have mod-
elled the polarized cyclotron emission from a point source located in a
dipole magnetic field inclined to the spin axis of the white dwarf by some
angle β. This is the simplest case to model and is a good starting point
for understanding cyclotron emission.

The emission point in question has a magnetic longitude of $\psi = 180°$
and a magnetic latitude of $\theta = 5°$. Figure 2.4 gives the polarized cyclotron
emission for a range of inclinations of the system. I have kept the mag-
netic dipole offset angle at a constant value of $\beta = 25°$. The inclination
increases from an angle of $i = 5°$ in the top row to $i = 85°$ in the bottom
row. I have used the $T_e = 10$keV temperature model of WM85 with a po-
lar magnetic field strength of $B_p = 1.4 \times 10^7$ Gauss and the optical depth
parameter set to $\Lambda = 1.0 \times 10^7$ at the magnetic pole. The columns in the
figure are the white dwarf at spin phase $\phi = 0.5$, the intensity, circular
polarized flux, linear polarized flux and the position angle of linear po-
larization respectively. Phase zero ($\phi = 0$) in the diagrams corresponds
to when the magnetic dipole in the hemisphere most pointing towards the
observer is on the opposite end of the spin axis of the white dwarf. Thus
phase $\phi = 0.5$ corresponds to when the magnetic dipole is most pointing
towards the observer (Fig. 2.4). The light curves correspond to the I pass-
band.

The four columns describing the polarizations can now be explained in
turn. Firstly the intensity curves show their dependence on viewing an-
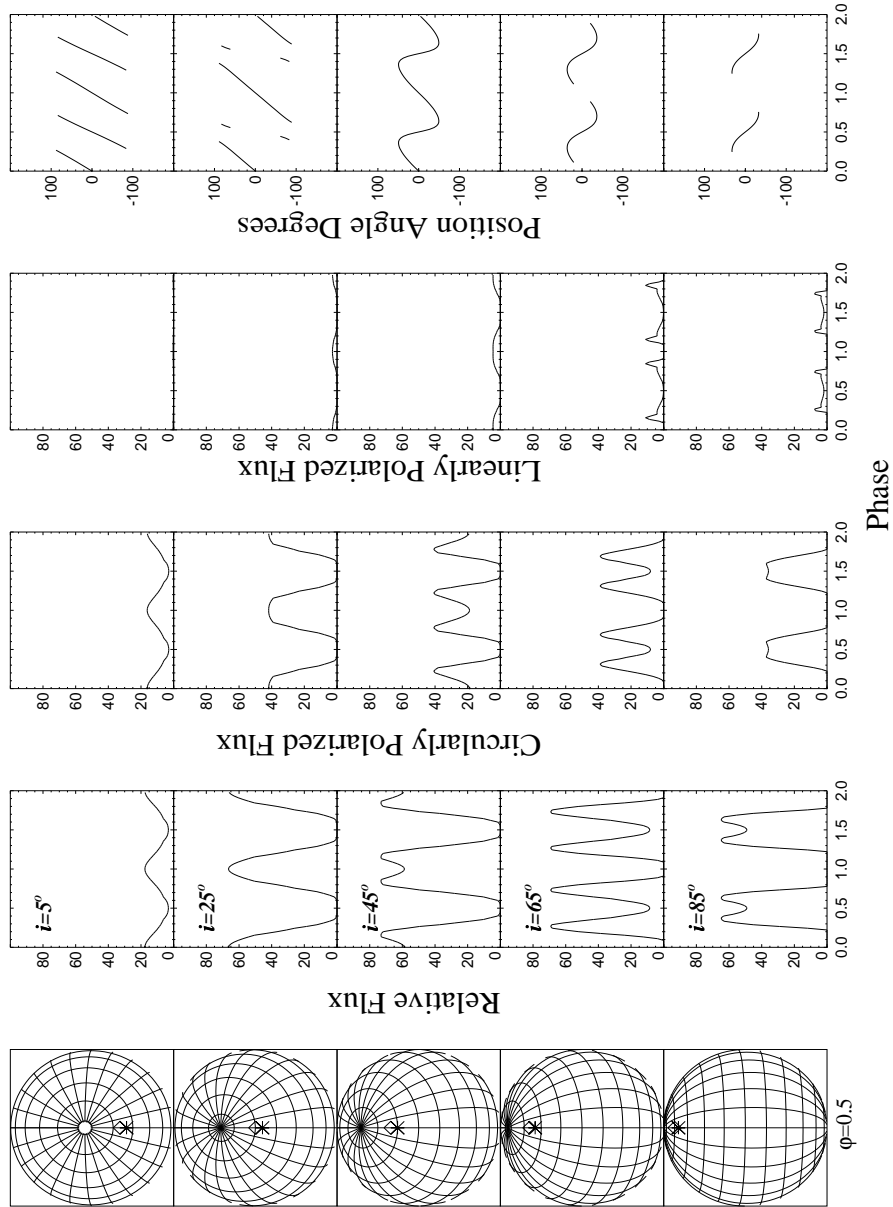
Figure 2.4: Point source emission. $\theta = 5^\circ, \psi = 180^\circ, \beta = 25^\circ$
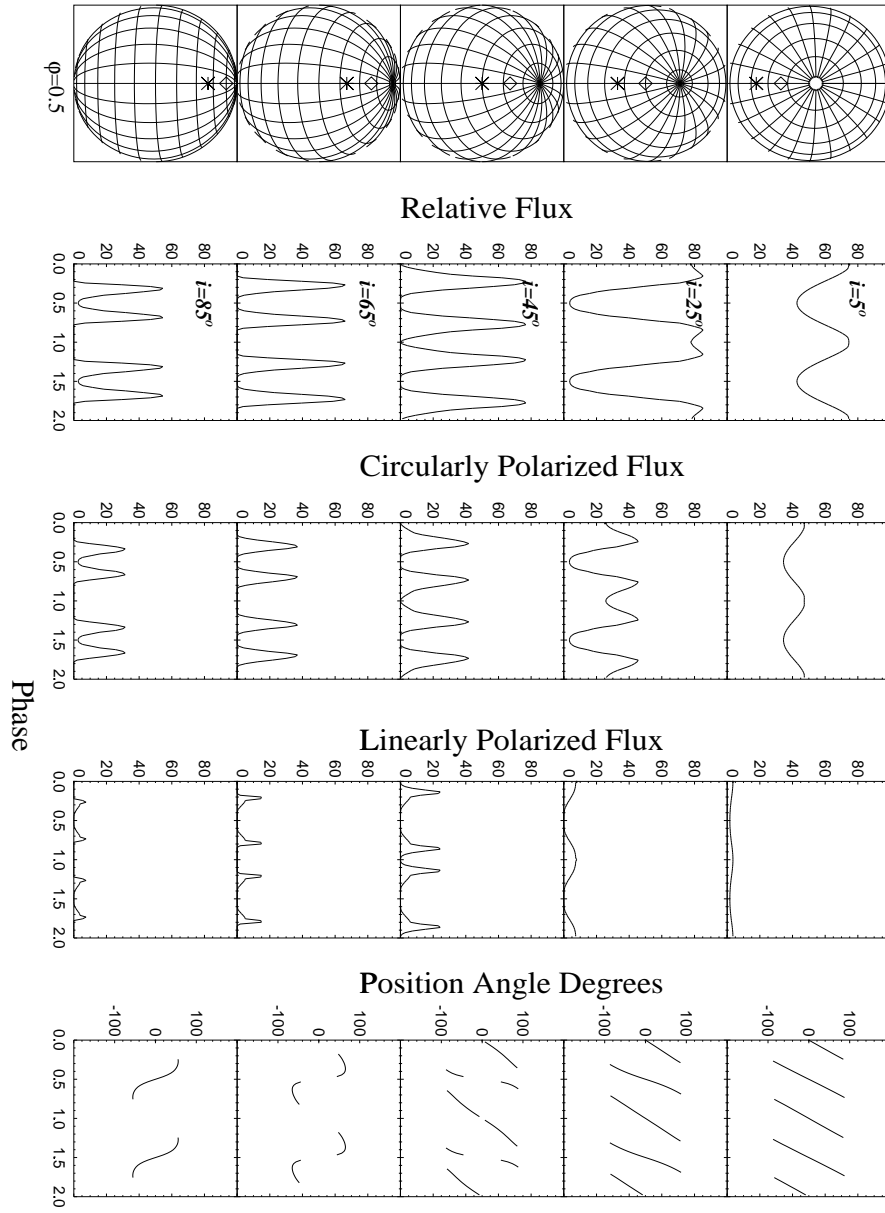
Figure 2.5: Point source emission.$\theta = 20°, \psi = 180°, \beta = 25°$

gle. At the lowest inclination most of the intensity arises at phase $\phi = 0$ and the least at phase $\phi = 0.5$. At this low inclination the variation of viewing angle (not position angle) is low and so the amplitude of the intensity variations is relatively low. However, as the inclination of the system is increased the beaming effect becomes more important at phase $\phi = 0$ shown by an increase in the intensity at this phase and by an increase in the amplitude of the light curve. At phase $\phi = 0.5$, with the system at an inclination of $i = 25°$, the magnetic field line at the emission point is almost parallel to the line of sight of the viewer. The dip at this phase arises as a result of free-free or self absorption of the cyclotron radiation. As the inclination of the system increases further the beaming effect at phase $\phi = 0$ becomes less important and a dip starts to split the peak into two. Also at phase $\phi = 0.5$ absorption effects become less pronounced increasing the level of intensity at this phase. At some point, the absorption dip and the main dip due to cyclotron beaming become comparable to each other, giving rise to a double–peaked intensity light curve. Eventually, at the highest inclinations, the emission point at phase $\phi = 0$ is occulted by the white dwarf thus giving zero intensity, while at phase $\phi = 0.5$ the effects of absorption are becoming negligible giving rise to a peak.

The second column in figure 2.4 shows the circularly polarized flux. Again, as for the intensity in the low inclination system, the amplitude of the polarization curve is small relative to the higher inclinations with a maximum at phase $\phi = 0$ and a minimum at phase $\phi = 0.5$. Depolarization of the cyclotron radiation has a marked effect at phase $\phi = 0.5$ where the magnetic field line, from which emission emanates, is close to

being parallel to the line of sight. At the highest inclinations there is now a peak at phase $\phi = 0.5$ where the angle to the magnetic field moves away from the line of sight. Due to occultation of the white dwarf, there is no emission at phase $\phi = 0$.

As can be seen from the third column in figure 2.4, the flux of linear of polarization remains at relatively low levels for the low and intermediate inclination angles. However, as the inclination approaches high values, there is an increase in the level of linearly polarized flux in very narrow regions of phase. These large peaks coincide with the phase at which the intensity and circular polarization decrease rapidly to zero, when the emission point disappears or reappears over the limb of the white dwarf and hence the angle between the magnetic field line and the line of sight approaches $90°$.

The position angle of the linear polarization is the angle of the projection of the magnetic field into the plane of the sky. It is therefore an indication of the direction of the magnetic field. The fourth column in figure 2.4 shows that for low inclination systems the position angle of linear polarization varies rapidly through $360°$, shown here as varying between $-90°$ and $90°$. The higher inclined systems give a smaller and more sinusoidal variation in position angle. However the viewing angle (not the position angle) to the magnetic field line, now varies from $\alpha \sim 90°$ as the emission point appears over the limb of the white dwarf, to $\alpha \sim 0°$, as it passes closest to the line of sight, and then back to $\alpha \sim -90°$, as it disappears over the limb of the white dwarf.

Figure 2.5 shows the effects of moving the emission point further in magnetic latitude ($\theta = 20°$) from the magnetic pole (all other parameters

are kept the same). The basic shapes of the light curves remain the same, except that features which vary with an increase in the inclination now occur sooner at lower inclinations.

The intensity and the circular polarization light curves become double–peaked at a lower inclination than for the above case and remain so for the highest inclinations. The linear polarization peaks also appear at smaller inclinations and are slightly larger than the smaller dipole offset models. The position angle of the linear polarization varies over a large range of angles and continues to do so for higher inclinations than it did for the $\theta = 5°$ case.

2.2.2 Offset point sources

The point source emission models described above are all rather symmetrical. In reality the light curves observed from real systems are asymmetrical. Many of the asymmetries can be modelled by offsetting the emission point in magnetic longitude (ψ).

Figure 2.6 shows the result of modelling the emission from a point source with the parameters $\psi = 135°, \theta = 20°, \beta = 25°$ and the inclination running from $i = 5°$ to $i = 85°$. The only difference from above being that the magnetic longitude (ψ) has been changed to $135°$ which places it ahead of the magnetic pole in spin phase.

As expected, intuitively, the intensity variations are similar as before but are slightly ahead in phase. Asymmetries start to become more pronounced in the higher inclined models. The double–peaks of the intensity, circular polarization and especially the linear polarization become unequal. Generally there is more cyclotron emission when the emission

φ=0.5
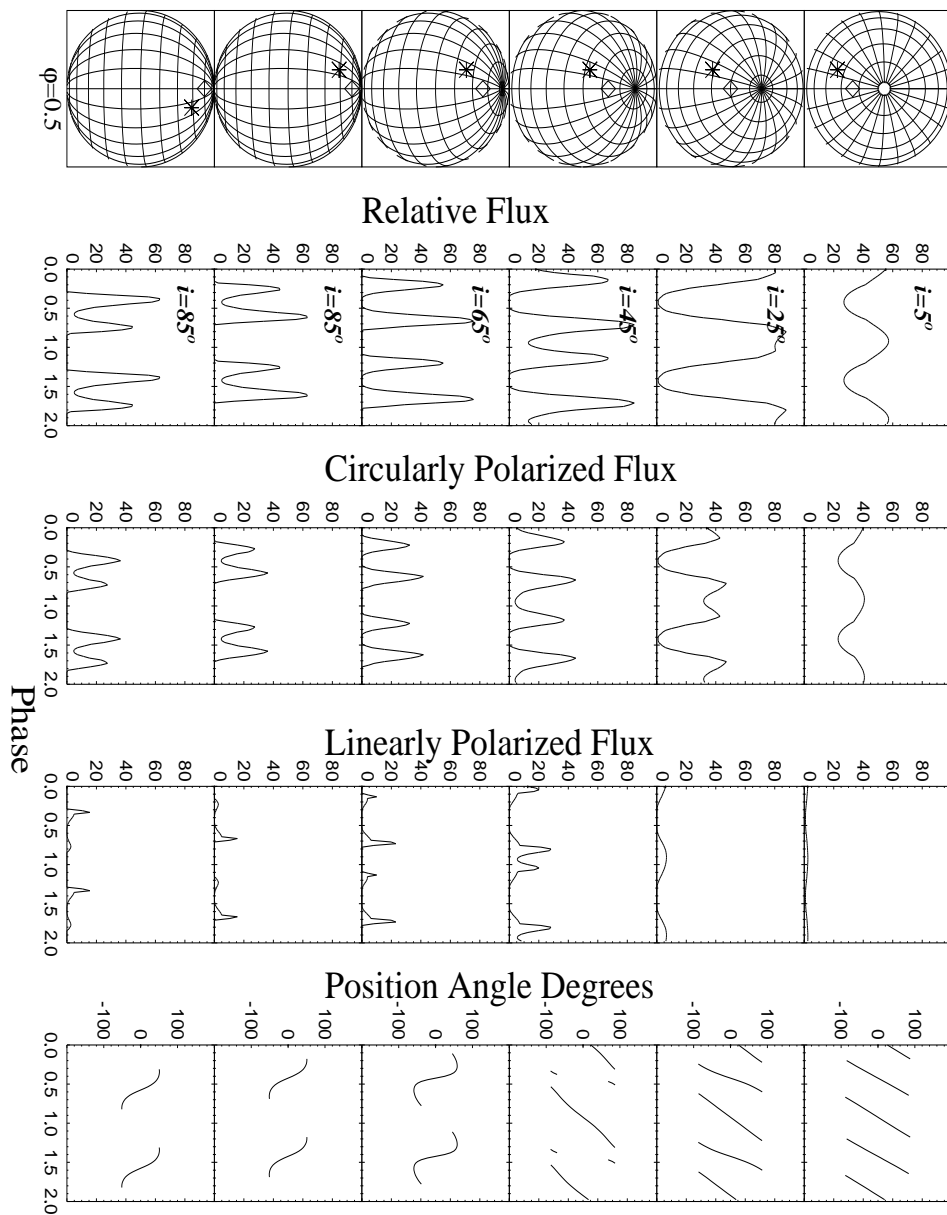
Figure 2.6: Offset point source emission. $\theta = 20°, \psi = 135°, \beta = 25°$

point disappears over the limb of the white dwarf. This is because the field line points slightly in the direction of rotation of the white dwarf. Before the emission point disappears around the limb of the white dwarf, the viewing angle passes through $90°$ giving rise to a larger linear polarization pulse.

The position angle of the linear polarization curves are slightly earlier in phase.

Changing the magnetic longitude to $\psi = 225°$ puts the emission point behind the magnetic pole so that it appears later in phase around the limb of the white dwarf than the magnetic pole. The only difference in the intensity, circular polarization and linear polarization is that they are inverted in phase with respect to the model just described above (bottom row of figure 2.6). i.e. the large and small peaks have interchanged places. This time the magnetic field line is pointing slightly backwards from the rotation of the white dwarf.

The position angle of linear polarization has the same basic shape as above, but has been rotated through $180°$. To reflect the position angle light curve through $0°$ requires that the sign of the polarization be reversed. In this case all the other polarization curves remain the same except for the circular polarization, which will have changed its sign.

2.2.3   Two opposite point sources

Finally I consider emission from two point sources diametrically opposed on a magnetic dipole field. The emission points have the parameters $\psi = 180°, \theta = 20°$ (same as the one point source described above, upper emission point) and $\psi = 0°, \theta = 160°$ (lower emission point) with the magnetic

dipole offset at an angle of $\beta = 25°$. Positive and negative polarizations emanates from the poles most pointing towards and away from the observer respectively.

Figure 2.7 shows the model polarization light curves. I have shown the light curves produced for system inclinations of $i = 65°$ and $i = 85°$. (For lower inclinations the lower emission point is occulted by the white dwarf during all spin phases and the light curves reduce to the one point source model depicted in figure 2.5).

The intensity, circular polarization and the position angle of linear polarization are easily separable in phase into the two emission components. The emission points are diametrically opposed on the white dwarf resulting in one emission point only, being visible at any particular phase (except at the phase where they are both on the limb of the white dwarf). Therefore during the phase interval $\phi \sim 0.2 - 0.8$ the light curves are exactly the same as the one point emission model described in figure 2.5. During the phase interval $\phi \sim 0.8 - 1.2$ the lower emission point, responsible for the negative polarization, is the source of the polarization emission.

The most obvious indication that there is two pole emission is that there is both negative and positive circular polarization. The positive peak has a dip superimposed on it due to the emission point being close to the line of sight. The negative polarization is single peaked because the lower emission point has larger angles to the line of sight, except in the higher inclination case. However because of these larger angles, the linear polarization pulses from the lower hemisphere will be larger than the linear polarization pulses from the upper hemisphere. Also, as a re-
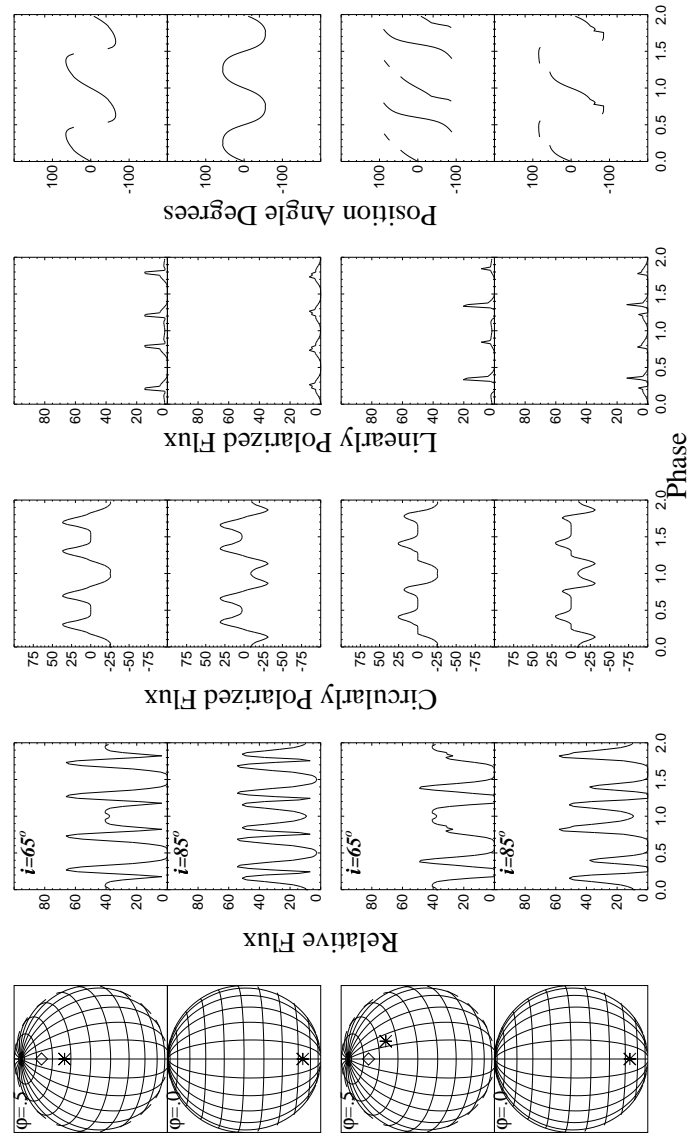
Figure 2.7: Two opposite point sources. $\theta = 20°, \psi = 180°$ (upper emission point) $\theta = 160°, \psi = 0°$ (lower emission point), $\beta = 25°$

sult of the emission points being diametrically opposed, they appear on the limbs of the white dwarf at the same time. The linear polarization pulses from the upper and lower emission points are then indistinguishable. The position angle of linear polarization shows a smooth sinusoidal variation because both emission points act exactly out of phase.

In the bottom two rows of figure 2.7 I have demonstrated the effects on the polarization light curves of moving one of the emission points so that they are no longer diametrically opposed. Specifically, the upper emission point now has the parameters $\psi = 220°$ and $\theta = 40°$.

The intensity and positive circular polarization curves start to show asymmetries as demonstrated in the one point source emission model discussed above. Now that the two emission poles appear over the limbs of the white dwarf at slightly different phases, the linear pulses become distinguishable from each other. The largest pulse arises from the upper emission point only and the two unequal, asymmetrical pulses arise from the combined emission from both points.

2.2.4   Emission from extended sources

Although the point source models are successful in describing some of the general characteristics of the polarized cyclotron emission in systems such as AM Hers and IPs, they cannot explain several observational features. Firstly a point source with a constant optical depth parameter Λ, cannot reproduce the wide wavelength range over which circular and linear polarizations are observed. Secondly, extended sources are better at producing the asymmetries in the phase dependent intensity and polarization curves. Also, extended regions are expected, cf chapter 1. Below

I demonstrate the effects of extended emission regions and take into account the effects of field spread, change in magnetic field strength and thus the optical depth parameter across the emission region.

2.2.5   Symmetric arcs

I first model arc shaped emission regions symmetrically placed around the magnetic dipole. Figure 2.8 shows the model light curves of emission arcs of increasing extent in magnetic longitude ψ. Each arc is kept at a constant magnetic latitude of $\theta = 20°$. Also in each case the inclination, magnetic dipole offset, wavelength range, polar magnetic field strength and the optical depth parameters are kept at constant values of $i = 65°, \beta = 25°, \lambda = 7.5 \times 10^{-7} - 8.5 \times 10^{-7}\mathrm{m}$, $B_p = 1.4 \times 10^7$ Gauss and $\Lambda_p = 1.0 \times 10^7$ respectively.

The top row shows the light curves for an arc extended in magnetic longitude $\delta\psi = 10°$ from $\psi = 175°$ to $\psi = 185°$. The differences between the single point source in figure 2.5 (row 4) and the small symmetrically placed arc are very slight. However as the length of the arc is increased, changes start to appear.

Firstly, as the arc increases in size parts of it remain uneclipsed for a larger fraction of the spin phase thus broadening the spin pulses. The absorption dip in the intensity and the circular polarization becomes less pronounced as the amount of emission either side of the center of the arc increases. Indeed, when the arc becomes sufficiently extended, the amount of polarized emission emanating from either side of the center of the arc increases to produce a peak where absorption would have otherwise occurred if emission was from only the center of the arc.
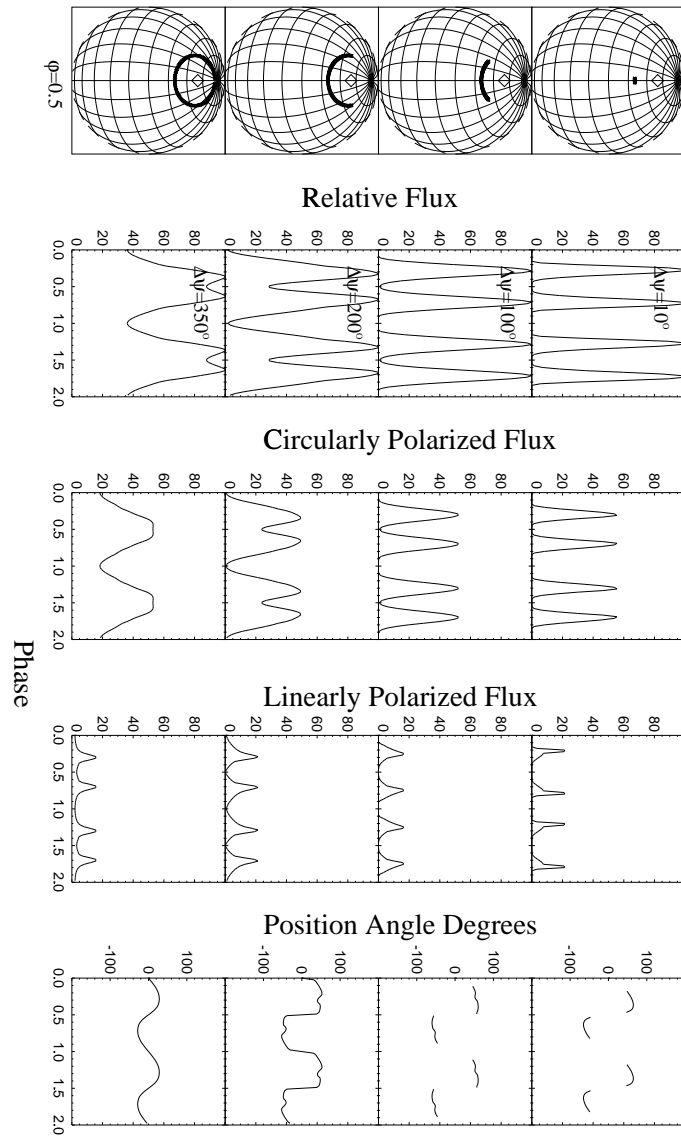
Figure 2.8: Symmetric arcs. $\theta = 20^{\circ}, \beta = 25^{\circ}$

The position angle of linear polarization also begins to show more features with dips and bumps appearing at various phases. Particularly noticeable are the dips in the otherwise sinusoidal variation at phases $\phi \sim 0.3$ and $\phi \sim 0.7$. These occur when half of an arc has appeared over the limb of the white dwarf. The two peaks at either side of the dip are then explained as the result of two sinusoidal variations slightly out of phase. Also, because of the contribution of emission from points on field lines at different angles, the amplitude of the position angle variation decreases. The bottom row shows emission from an arc that is almost a ring. In this case, part of the arc is always in view resulting in a smooth sinusoidal variation in the position angle curve.

2.2.6   Asymmetric arcs

Next I consider the effects of extending the arc at a constant magnetic latitude, asymmetrically around the magnetic pole in an anticlockwise direction from the line joining the spin and magnetic poles (Fig. 2.9). The inclination, magnetic dipole offset angle, wavelength range, polar magnetic field strength and the optical depth parameters are kept at constant values as above.

The polarized light curves can be understood as a combination of the main features from all the model simulations described above. Firstly the unequal weighting of the intensity pulses can be understood by the same reasons for the offset point source emission. i.e. there will be preferentially more emission as the emission region appears over the limb of the white dwarf where the viewing angles go through $90°$. The emission region will have disappeared over the limb of the white dwarf before the

field lines have a second chance of being viewed through $90°$. In the offset point source model (Fig. 2.4), the emission point was placed ahead of the magnetic pole, thus there was preferentially more emission in the second pulse.

Next, as the arcs increase in extent, the absorption dip gradually becomes less pronounced giving rise to a peak with the largest arcs. This is similar to the symmetric arcs described above. The final intensity best shows the combination of all these features. It appears to be only one pulse, however it results from the addition of the two intensity pulses joined together by a third pulse, rather than an absorption dip, as a result of the extended arc.

Finally the linear polarization pulses show a rapid change in their relative weighting. For the smallest arc, both pulses are of equal strength. However, as the arc increases the second pulse becomes much less significant. As the arc then extends past $\delta\psi = 180°$ the pulses become more equally weighted. As before, the amplitude of position angle decreases and is no longer a smooth sinusoidal variation. Again as for the symmetrical arcs, the dips that appear in the otherwise smooth variation of the position angle occur when a significant part of the arc appears over the limb of the white dwarf.

2.2.7   Extended arcs

So far I have only considered arcs that have been placed at a constant magnetic latitude. In reality, material in an MCV probably attaches to magnetic field lines at a radius from the white dwarf which varies with magnetic longitude. Here I model emission from arcs that are extended
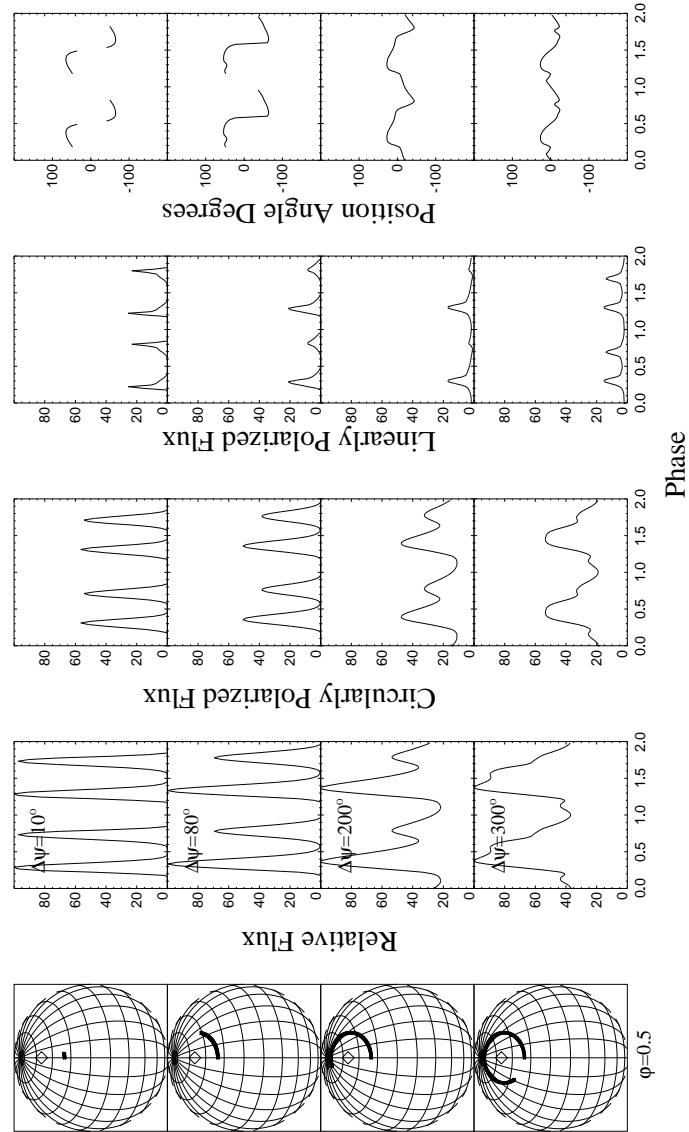
Figure 2.9: Asymmetric arcs. $\theta = 20^\circ, \beta = 25^\circ$

in magnetic longitude (ψ) and magnetic latitude (θ) towards the magnetic equator. Arcs may be extended in other ways but I found that extending the arcs away from the magnetic pole towards the magnetic equator, giving it a comma type shape, was best at reproducing some observational features (see later).

The top three rows of figure 2.10 shows the result of increasing the extent of the accretion arc. In all the plots I have again kept the inclination, magnetic dipole offset angle, wavelength range, polar magnetic field strength and the optical depth parameters constant. However the magnetic field strength and hence the optical depth parameter, now vary across the emission arc as a result of the change in magnetic latitude. In each row the arc is extended in magnetic longitude by $\delta\psi = 110°$ from $\psi = 80°$ to $\psi = 190°$.

The first thing to notice is the unequal weighting of the intensity and linear polarization pulses due to the offset arc as explained above. From figure 2.10 it can be seen that extending the arcs has the most pronounced affect on the linear polarization and its position angle.

The first linear pulse appears smaller in strength but broader in phase, while the second pulse keeps its sharp tall shape. This is because the arc gradually appears over the limb of the white dwarf, so that different parts of the arc contribute a linear pulse at slightly different phases. However most of the arc will disappear over the limb of the white dwarf all at the same time, especially when the arc is more extended in magnetic latitude, giving rise to a sharper linear pulse.

The position angle variation appears more complicated than the previous case. The most obvious feature is that the variation in position an-
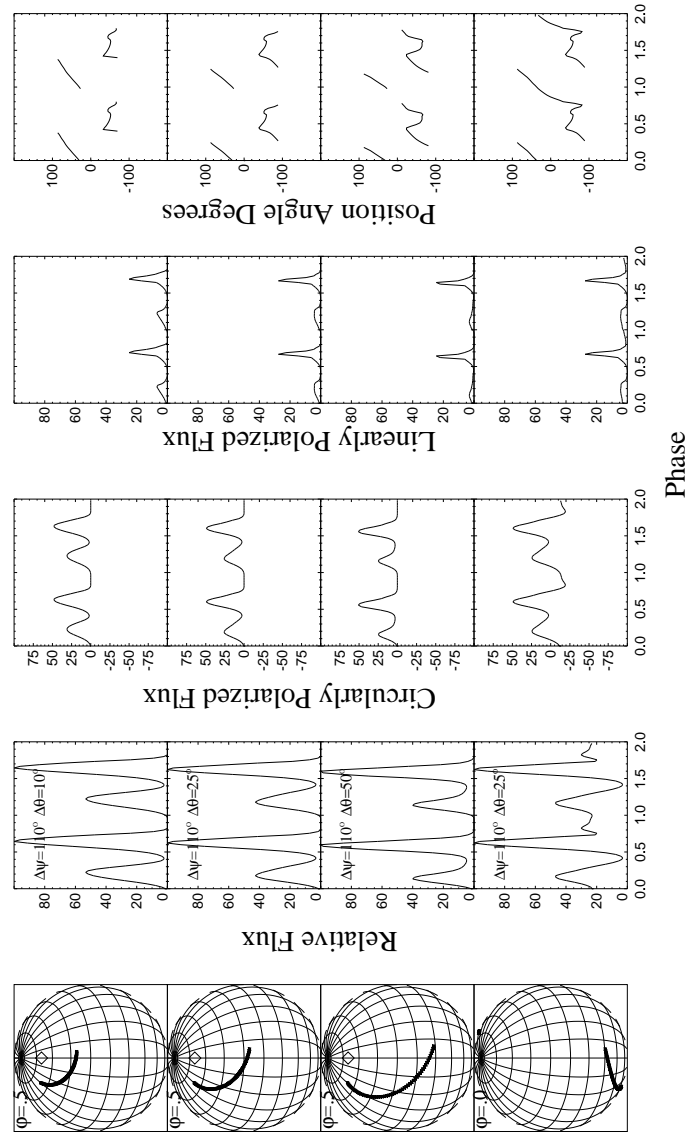
Figure 2.10: The models showing the results of increasing the extent of the arc from the top to the bottom. The bottom plot shows the emission from two diametrically opposite arcs .

gle remains very large. Previously, when extending the arc at constant magnetic latitude, the variation in position angle would decrease. As the arc is extended the variation in position angle becomes steeper. Also, various features in the position angle curve more slightly earlier in phase as more of the arc is weighted ahead of the magnetic dipole. There are basically three dips corresponding to the appearance of the arc over the limb of the white dwarf, to the arc passing through the line of closest approach and to the disappearance of the arc over the limb of the white dwarf.

2.2.8 Two opposite arcs

Finally I consider emission from extended sources diametrically opposed on a magnetic dipole field. The emission arcs have the parameters $\delta\psi = 110°, \psi_1 = 80°, \psi_2 = 190°, \delta\theta = 25°, \theta_1 = 20°, \theta_2 = 45°$ (upper emission arc) and the lower emission arc has the parameters $\delta\psi = 110°, \psi_1 = 260°, \psi_2 = 370°, \delta\theta = 25°, \theta_1 = 160°, \theta_2 = 135°$. Once again I have used the constant values for the inclination, magnetic dipole offset angle, wavelength range, polar magnetic field strength and the optical depth parameters as above. Positive and negative polarizations emanate from the poles most pointing towards and away from the observer respectively. The modelling is shown in the bottom row of figure 2.10.

As with the point source emission, the presence of both negative and positive polarizations is the first obvious indication that I am modelling emission from two regions. Also the peak in the positive circular polarization has an absorption dip superimposed on it, confirming that this arc is in the hemisphere most pointing towards the observer. The negative circular polarization peak shows no such absorption dip as would be ex-

pected for the larger angles the magnetic field lines from this arc make to the line of sight. A third intensity pulse is also seen in the light curve where the tail of the lower emission arc is favourably presented to the line of sight (phase $\phi \sim 0.9$).

The linear polarization is more difficult to entangle because I have modelled emission from arcs that are exactly diametrically opposed on the surface of the white dwarf. Hence linear polarization pulses from both arcs would occur at almost the same phase. Emission from two arcs can only be calculated from the relative weighting of the linear polarization pulses (compare one and two arc emission between rows 2 and 4 respectively). The smaller pulse is slightly broader in phase. The gaps in the position angle of linear polarization due to emission from one pole are now occupied by the emission from the second pole, making the position angle variation less discontinuous.

2.2.9   Wavelength dependence

Above I have shown that asymmetries in phase–dependent light and polarized curves can be modelled by emission from arc shape regions located on the surface of the white dwarf. This section addresses the wavelength dependence.

In figure 2.11 I compare the cyclotron intensity and total polarized flux spectra for a point source and an extended emission region. This shows graphically the point made earlier (section 2.2.4) that the point source emission cannot explain the wide wavelength range over which circular and linear polarizations are detected. In calculating the model cyclotron emission from an extended arc I have used the same model parameters
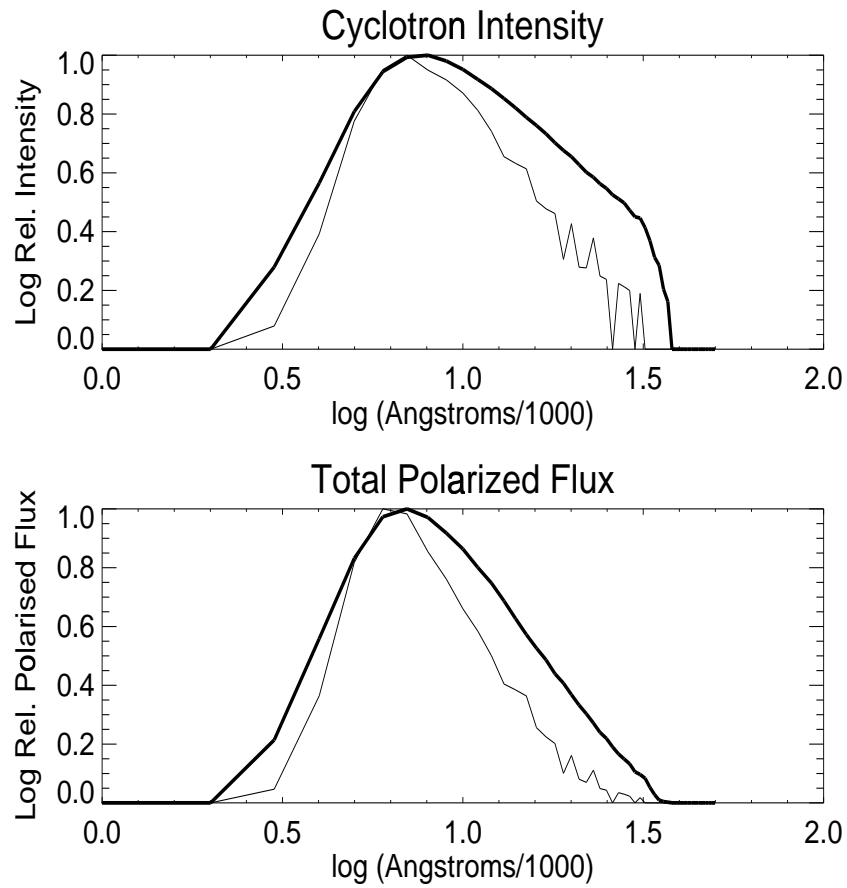
Figure 2.11: Cyclotron spectra. The thick and thin lines represent the extended and point source emission spectra respectively.
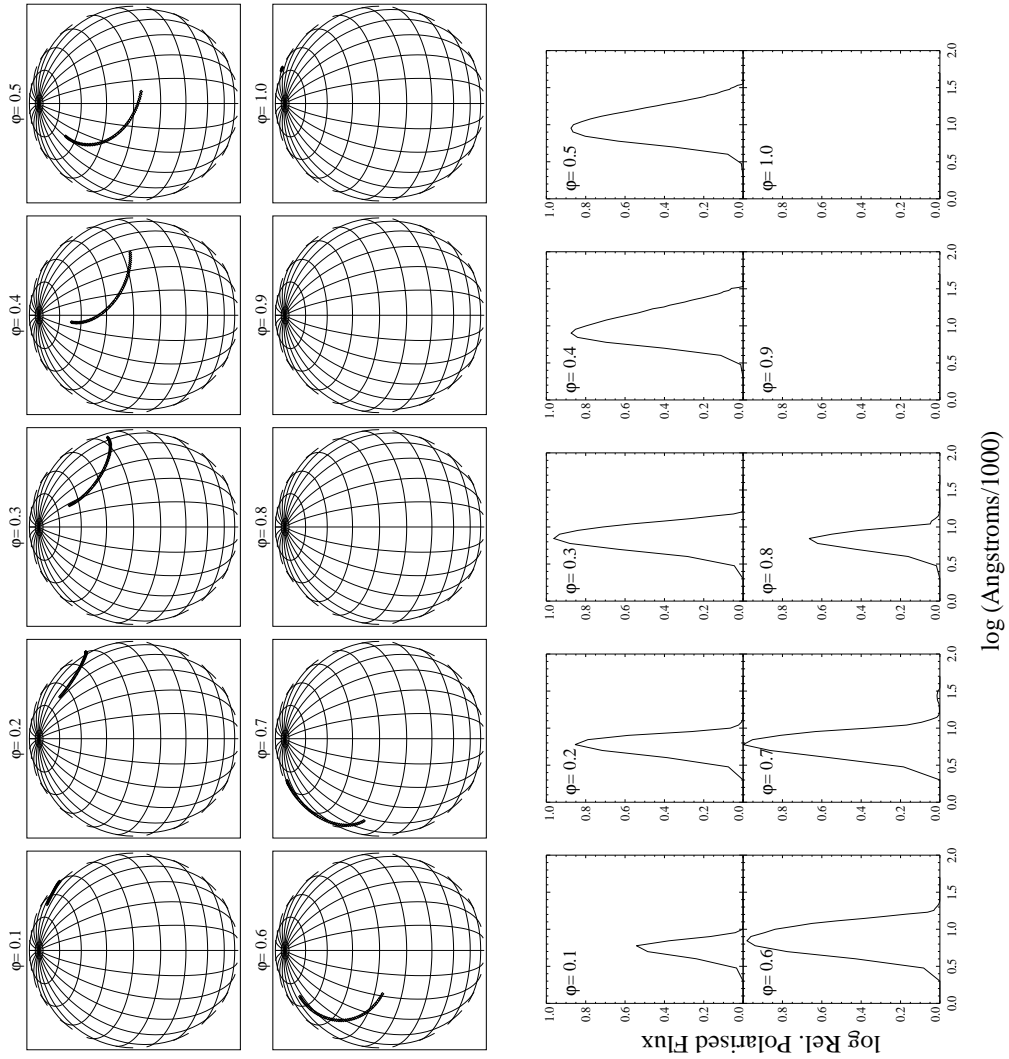
Figure 2.12: Phased cyclotron spectra.
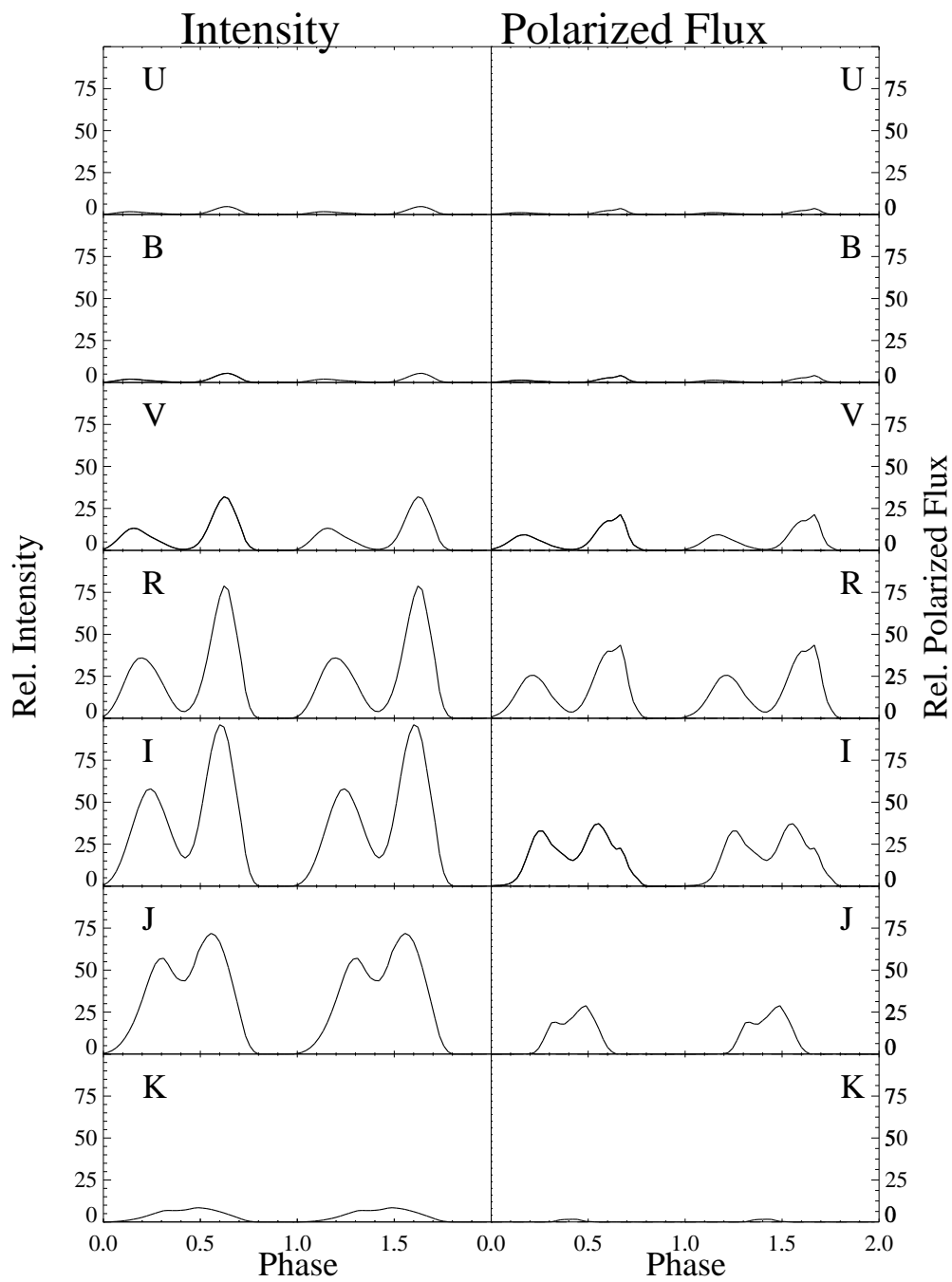
Figure 2.13: Multiwavelength modelling for the spectra in figure 2.12.

as those used in figure 2.10 (second row) i.e. the inclination $i = 65°$, magnetic dipole offset angle $\beta = 25°$, magnetic longitude is extended by $\delta\psi = 110°$ from $\psi = 80°$ to $\psi = 190°$ magnetic latitude is extended by $\delta\theta = 25°$ from $\theta = 20°$ to $\theta = 45°$ and the polar magnetic field strength and optical depth parameter are $B_p = 18\text{MG}$ and $\Lambda_p = 1.0 \times 10^7$ respectively. The point source model has a magnetic longitude of $\psi = 180°$ and a magnetic latitude of $\theta = 20°$ with the other parameters unchanged.

The spectra shown in figure 2.11 are the summed, normalised spectra for one complete rotation of the white dwarf. The top row shows the cyclotron intensity spectra, while the bottom row is the polarized flux intensity spectra. It is immediately obvious that the extended arc model spectra (thick lines) are more extended in wavelength than the point source model spectra (thin lines). Also there is more flux at the shorter and longer wavelength ends of the extended arc spectra. The point source spectra show cyclotron humps which appear to have been smoothed out in the extended arc spectra.

These effects are a result of the magnetic field strength, and hence the optical depth parameter, varying across the emission arc. The point source model will give maximum flux and cyclotron harmonics at specific wavelengths depending on the magnetic field strength at that point. However, in the extended arc model, each point along the arc has a different magnetic field strength, forcing the maximum flux and cyclotron harmonics of each point to occur at slightly different wavelengths. As a result, when the spectra from all these points are summed, any cyclotron harmonics are smoothed out.

In figure 2.12 I demonstrate how the extended arc polarized spectra

change over the spin phase of the white dwarf. In the same figure I also show how the arc appears to the viewer as a function of phase.

The first and most obvious feature is at phase $\phi \sim 0.9 - 0.0$ where the polarized flux has decreased to zero. This coincides with the occultation of the emission arc by the white dwarf. There is also a slight dip in the maximum polarized flux at phase $\phi \sim 0.4 - 0.6$ due to cyclotron self absorption or electron scattering which results in depolarization of the cyclotron radiation as the emission arc is viewed parallel to the magnetic field lines.

It can also be seen that the polarized energy distribution changes as a function of phase, evident from a change in the width of the spectra. This is most noticeable on the red end of the spectra, which increases from zero at phase $\phi \sim 0.0 - 0.1$ to a maximum at phase $\phi \sim 0.4 - 0.5$ during which the fraction of the arc visible to the viewer also increases. After phase $\phi \sim 0.5$ the amount of red polarized flux rapidly decreases, except at phase $\phi = 0.7$ where there might be an indication that the red flux is on the increase. The arc disappears over the limb of the white dwarf before the polarized flux is given the chance to increase any further.

These features are again explained as a result of the combination of the magnetic field strength varying across the extended arc and the spread in the magnetic field lines across the arc. The front end of the arc is closest to the magnetic dipole and hence has the strongest magnetic field. As a result the spectra from the front of the arc is slightly bluer than the spectra from the tailing end of the arc where the magnetic field strength is weaker.

As this is the case, one would then expect time delays in the phase de-

pendent light curves between different wavelengths. In figure 2.13 I have plotted the intensity and the total polarized flux light curves for different wavelengths corresponding to the UBRIJ and K wave bands.

Both the intensity and the polarized flux show maximum flux in the I band and decreases rapidly either side of this band. The absorption dip is very prominent in the bluer bands at phase $\phi \sim 0.4$, becoming less pronounced towards the red bands. The bands in which the absorption dip and the maximum polarized flux occurs are dependent on the polar magnetic field strength: a stronger magnetic field will move the light curves further into the bluer wavelengths.

As predicted above, the bluer polarized flux begins to rise to a maximum before the red polarized flux, while the intensity rises at almost the same time in all bands (phase $\phi \sim 0.0 - 0.3$). The absorption dip at phase $\phi \sim 0.3 - 0.5$ decreases towards the red, not only because of its energy dependence but also because the red flux emanating from the tail end of the arc is not yet at the orientation at which it would be self–absorbed. The tail end of the polarized pulse at phase $\phi \sim 0.6 - 0.8$ is cut short at the redder bands because the tail end of the extended arc is now self–absorbed. Note the intensity pulse decreases to zero at phase $\phi \sim 0.8$ in all the wave bands. The arc then disappears over the limb of the white dwarf before the red polarized flux has a chance to increase once again.

2.3   Summary

In this chapter I have presented model polarized light curves of cyclotron emission for various shapes of emission regions on the surface of the white

dwarf. I have shown that the light curves show several different features which depend on the shape of the emission region. Some features are common to all emission regions and others only occur in certain circumstances. In general all four light curves (intensity, circular polarization, linear polarization and its position angle) are needed to predict the shapes of the emission regions. The main points can be summarised as follows:

- The amplitude of the variation in the intensity light curve is a good indicator of the inclination of the system. i.e. low inclinations generally give low amplitude variation. Larger amplitudes also arise from systems in which the magnetic dipole is offset from the spin axis or the emission region is offset from the magnetic pole.

- Emission from single point sources show smooth variations in the position angle curve with an amplitude also dependent on the inclination of the system.

- Emission from regions located on opposite hemispheres of the white dwarf are usually identified by both positive and negative circular polarization.

- The relative sizes of the intensity humps, and especially the linear polarized pulses, indicate whether the emission region is ahead or behind in phase with respect the the magnetic dipole.

- Large linear pulses occur when emission regions traverse the limb of the white dwarf.

- Regions extended in magnetic longitude show dips in the position angle variation corresponding to the regions being on the limb of the white dwarf or crossing the line of closest approach to the observer.

- Regions extended in both magnetic longitude and latitude shift the position angle dips in phase and also alter the magnitude of the dips. Unlike regions extended in magnetic longitude only however, regions extended in magnetic latitude have large variations in position angle for high as well as for low inclined systems.

- Extended sources show polarized emission over a larger wavelength range than for single point sources.

- The wavelength at which the most polarized flux occurs is dependent on the magnetic field strength of the white dwarf.

- Absorption and occultation by the white dwarf of the emission region can cause dips to occur in the polarized light curves. Absorption dips are generally energy dependent and also depend on the magnetic field strength of the white dwarf.

Similar work on modelling accretion regions has been carried out by for example Piirola et al. (1993), Ferrario & Wickramasinghe (1990) and Cropper (1986). The work done in this chapter, however, was provided to give a more extensive review of how the effects of different shapes and locations of emission regions effect the characteristics of the cyclotron radiation when viewed from Earth. This chapter also forms the basis for the chapters that are about to follow.

Chapter 3

A multi–wavelength study of the intermediate polar PQ Gem

3.1 Introduction

PQ Gem (RE J0751+14) was discovered as an extreme-ultraviolet $(70 - 200\text{Å})$ source during the first all-sky survey in this band, made with the Wide Field Camera (WFC) instrument on *ROSAT* (Pye et al. 1995). Observations by Mason et al. (1992; hereafter M92) in the X-ray, optical and infrared regions led to the classification of the source as a cataclysmic variable of the intermediate polar type (Chapter 1,Patterson 1994, Warner 1995). A double–peaked 13.9-min periodicity in the flux levels at both X-ray (*GINGA*) and infrared (K-band) wavelengths established by M92 was taken to be the spin period of the white dwarf in the binary system.

Such a profile is atypical of intermediate polar behaviour where the spin-pulses are usually quasi-sinusoidal. Variations in the centroid positions of the broad H emission lines discovered by M92 can be reasonably explained as being due to orbital motion with a period of the order of 5.5 h. The *GINGA* modulation showed a clear dependence on the X-ray energy when folded on the spin period. At the lowest energies the profile is highly asymmetric and there are two maxima and minima per cycle. The higher energy profiles are simpler showing only one maximum and minimum per cycle above 10 keV. As the energy increases the phase of maximum flux moves to an earlier phase.

The orbital period suggested by M92 is also consistent with a 14.5-min periodicity which is seen in the U, B, V bands (Rosen, Mittaz & Hakala 1993) being the synodic (beat) period. They suggested that the R and I-band light curves are of cyclotron origin having found evidence of variable circular polarization and that the double–peaked nature of the light curves are a result of the beaming of the cyclotron emission from one pole rather than emission from two poles.

Piirola, Hakala & Coyne (1993) studied the polarized flux variations first reported by Rosen, Mittaz and Hakala (1993). They found both positive and negative circular polarization varying over the spin period in PQ Gem and suggested cyclotron emission from two extended regions near the opposite magnetic poles of the white dwarf. Emission from a single region cannot produce a sign change in the circular polarization unless the region is sufficiently vertically extended to be seen beyond the limb, or the field lines are inclined, in which case only a brief sign change is seen. They simulated the polarized emission by using the calculations of

MW82. The calculations assumed radial field lines through the regions of cyclotron emission. The model generated positive and negative circular polarization from the upper and lower hemispheres respectively of the white dwarf. They estimated the strength of the magnetic field to be between 8-18 MG. PQ Gem was the first intermediate polar with a detection of spin-modulated polarization and this makes it an important object for further study.

Duck et al. (1994) obtained *ROSAT* pointed observations of PQ Gem which revealed a distinct soft X-ray component reminiscent of that seen in the strongly magnetic polars. When folded on the 13.9 minute spin period of the white dwarf, the soft X-ray light curve is characterised by a large amplitude, quasi-sinusoidal variation, the rising phase of which is cut into by a dip feature with a deep narrow core. A dip is seen at similar spin phase in the medium energy (1-20 keV) light curve measured with the *GINGA* satellite, most prominently at the lowest energies within this range (M92; Duck et al. 1994) and results in the double–peaked appearance of the medium energy light curve. It was suggested that the energy dependence of this dip is caused by absorption arising from the passage of dense accreting material in front of the emission region. There is no evidence for a 'soft X-ray excess' in the star (Mason 1995; Duck et al. 1994).

Väth et al. (1996) made a quantitative fit to the F_c^{obs} observations and assumed the same geometrical arguments as Piirola et al.(1993) to give a similar estimate of the magnetic field strength. Furthermore they made use of the X-ray observations of M92 to constrain the mass M_{WD} and the specific accretion rate $\dot{m}$ of PQ Gem.

Later Stavroyiannopoulos et al. (1996) obtained time-resolved HST

UV spectroscopy of PQ Gem. The $\lambda 1150 - 2600 \overset{\circ}{A}$ continuum light curve is dominated by the 13.9 minute spin period at all UV wavelengths covered. The profile of the light curve when folded on the spin period, contains a dip which is deepest in the far UV and which they believe, like its X-ray counterpart, is caused by stream occultation of the white dwarf. However, in their observations the UV dip was not exactly coincident with the phase of the X-ray dip. Also, the continuum and emission line fluxes were found to be modulated on the 14.5 minute beat period but in anti-phase. They concluded that the spectrum is multi-component in nature with two spin-modulated continuum components and a beat-modulated continuum component. One spin component rises towards the blue and appears to be occulted by the accretion flow while the other shows a red spectral distribution which is not obviously subject to absorption. They were unable to find a site or an explanation for the fact that the continuum and line fluxes were anti-phased on the beat modulation.

More recently (and following the publication of the work presented in this chapter in Potter et al. 1997) Howell et al. (1997) obtained simultaneous extreme ultraviolet and optical polarimetric and photometric observations of PQ Gem. The *EUVE* satellite performs simultaneous spectroscopic and photometric observations in the EUV spectral range ($70 - 170 \overset{\circ}{A}$; Bowyer & Malina 1991; Sirk at al. 1997) They showed that the EUV light curve is similar in appearance to the *ROSAT* pointed observations of PQ Gem obtained by Duck et al. (1994), including a narrow 'dip' feature that is modulated with the white dwarf spin period. They also used a slightly modified version of the cyclotron model presented below and obtained reasonable fits to the optical light curve and linear polar-

ization curve, but not the position angle variation.

Mason (1997) had used X-ray and optical timings of the 13.9 min white dwarf spin period to obtain an ephemeris for the spin period in PQ Gem. He found the spin period to be increasing on a timescale of 2.4×10^5 years ($\dot{P} = 1.1 \times 10^{-10}$). This is the largest period change yet found in an intermediate polar and only the second IP in which the spin period of the white dwarf is confirmed to be increasing. The low energy X-ray dip was found to precede the maximum X-ray light in phase, implying that the accretion stream strikes the surface of the white dwarf at an angle. This is consistent with a view (discussed below in this chapter) in which material accretes along field lines leading the magnetic pole in the rotation cycle of the white dwarf.

Buckley et al. (1995) have reported periodic polarization variability in a second intermediate polar, RXJ1712.6-2414. They detected negative circular polarization over the entire spin cycle, implying a low inclination system with only one accreting pole being observed. The only other intermediate polar with detectable circular polarization to date is BG CMi (Penning, Schmidt, & Liebert 1986), but this shows no detectable modulation at the white dwarf rotation period.

In this chapter I present simultaneous UBVRIJK observations of the intermediate polar PQ Gem (RE J0751+14) obtained on 1993 February 18 and 19 using the Hatfield Polarimeter on UKIRT and published in Potter et al. (1997). The light curves show double–peaked modulation on the spin period at the longer wavelengths and become single peaked at the shorter wavelengths. Both positive and negative circular polarizations are detected on the spin period in the V, to K bands as in previous obser-

vations by Piirola, Hakala & Coyne (1993) and suggesting emission from two magnetic poles.

I also present model light curves of cyclotron emission from opposite poles of a centered inclined magnetic dipole, as described in the previous chapter. Optimal results are obtained for an inclination of $\sim 60°$ and a magnetic dipole offset of $\sim 30°$. The model of cyclotron emission from two extended arc shaped accretion shock regions explains the dip in the negative circular polarization (see below) as free-free or self absorption of the cyclotron radiation by the accretion column. This occurs when the accretion region in the upper hemisphere traverses the line of sight (chapter 2). A wavelength independent intensity minimum occurs half of a spin cycle later when this region passes over the limb on the white dwarf. This model is inverted with respect to that proposed by Piirola et al. and Väth et al. and is more consistent with the X-ray observations. The arcs are placed ahead of the magnetic poles which I argue is consistent with the recently reported spin down of this system by Mason (1997). The model also provides an estimate of the magnetic field at the pole of $B_p \approx 9 - 21$ MG depending on the optical depth parameter used.

3.2   Instrumentation and Observations

Multi-colour photometry and polarimetry were obtained on the United Kingdom Infrared Telescope, Hawaii (UKIRT), on 1993 February 18 and 19th. Simultaneous photometric and polarimetric observations in the U, B, V, R and I optical bands and one of either the J or K infrared bands were made using the Hatfield Polarimeter (Hough et al. 1991). The po-

larimeter employs continuously rotating achromatic retarders and fixed analysers making it possible to obtain modulation efficiency over a relatively large wavelength range. The instrument is designed to have two separate beams on the sky, one for the optical and the other for the infrared. At any time one beam observes the source and the other observes the background. The telescope is switched between the two beams approximately every 30 seconds making the optical and infrared observations almost simultaneous. The two beams are separated by about 80 arcsec on the sky at the *f*/35 Cassegrain focus. Halfway through both nights the infrared filter was switched from J to K. The polarimeter was used in the simultaneous linear and circular polarization mode but the linear polarization observations were not of sufficient quality to give any useful results.

3.3 Results

Figures 3.1 and 3.2 show the photometric observations corrected for extinction. The light curves have an apparent $\sim$ 5hr sinusoidal variation, the amplitude of which is wavelength dependent, being most prominent in the U band and almost non-existent in the infrared bands. The length of each observation is not long enough to obtain a better estimate of this period; however there are other apparent maxima and minima from previously published work which are listed in table 3.1. These were estimated by eye. I have subtracted 0.5 cycles from the observations that show only minima and then searched all the timings of the maxima for a period. The search was conducted through the range 0.1-0.35 day at a
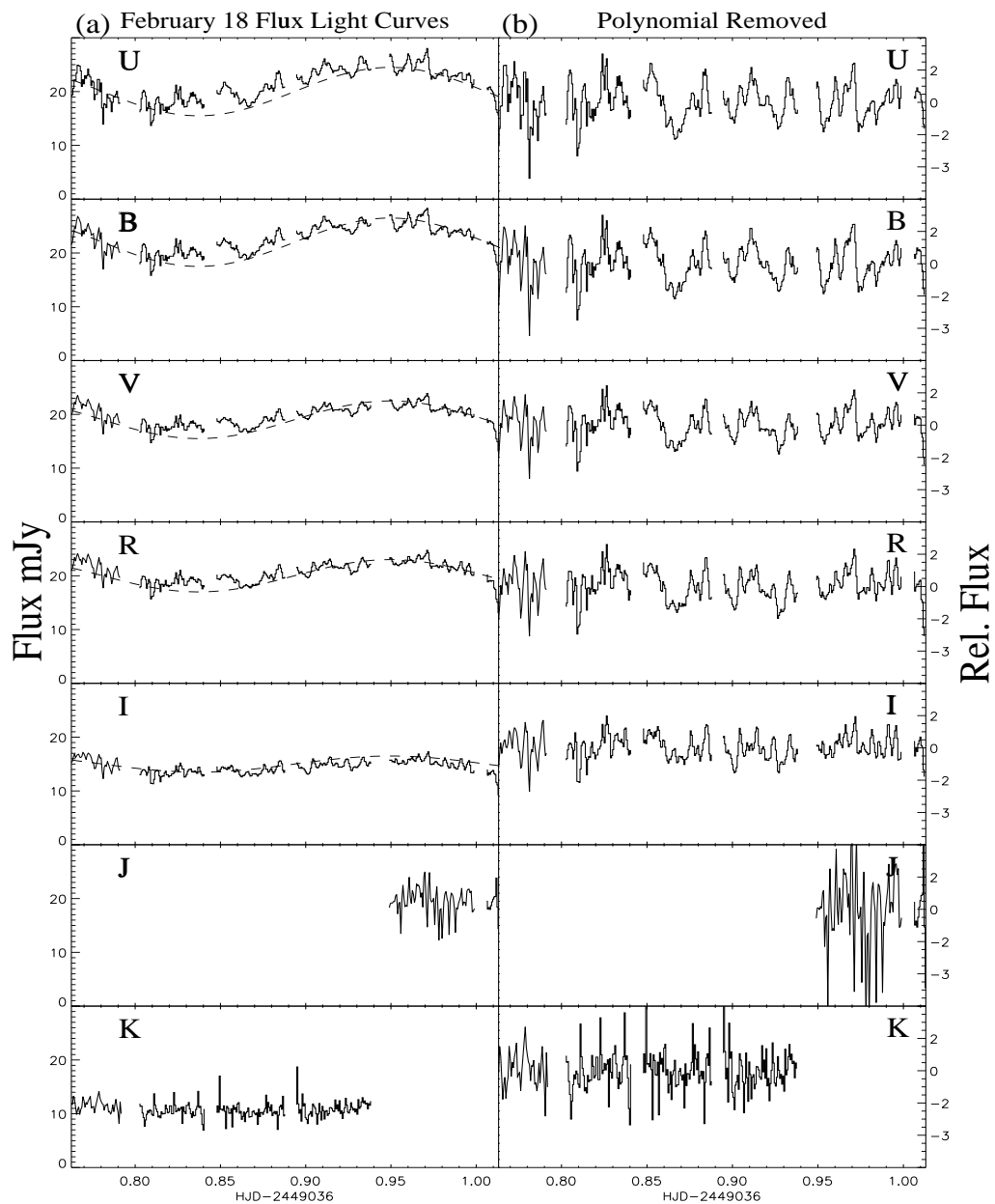
Figure 3.1: (a) Simultaneous light curves taken on 1993 February 18 with best fit sinusoids (period 5.18hr, epoch 2449036.95 HJD) (b) As for (a) but with a 3rd order polynomial subtracted.
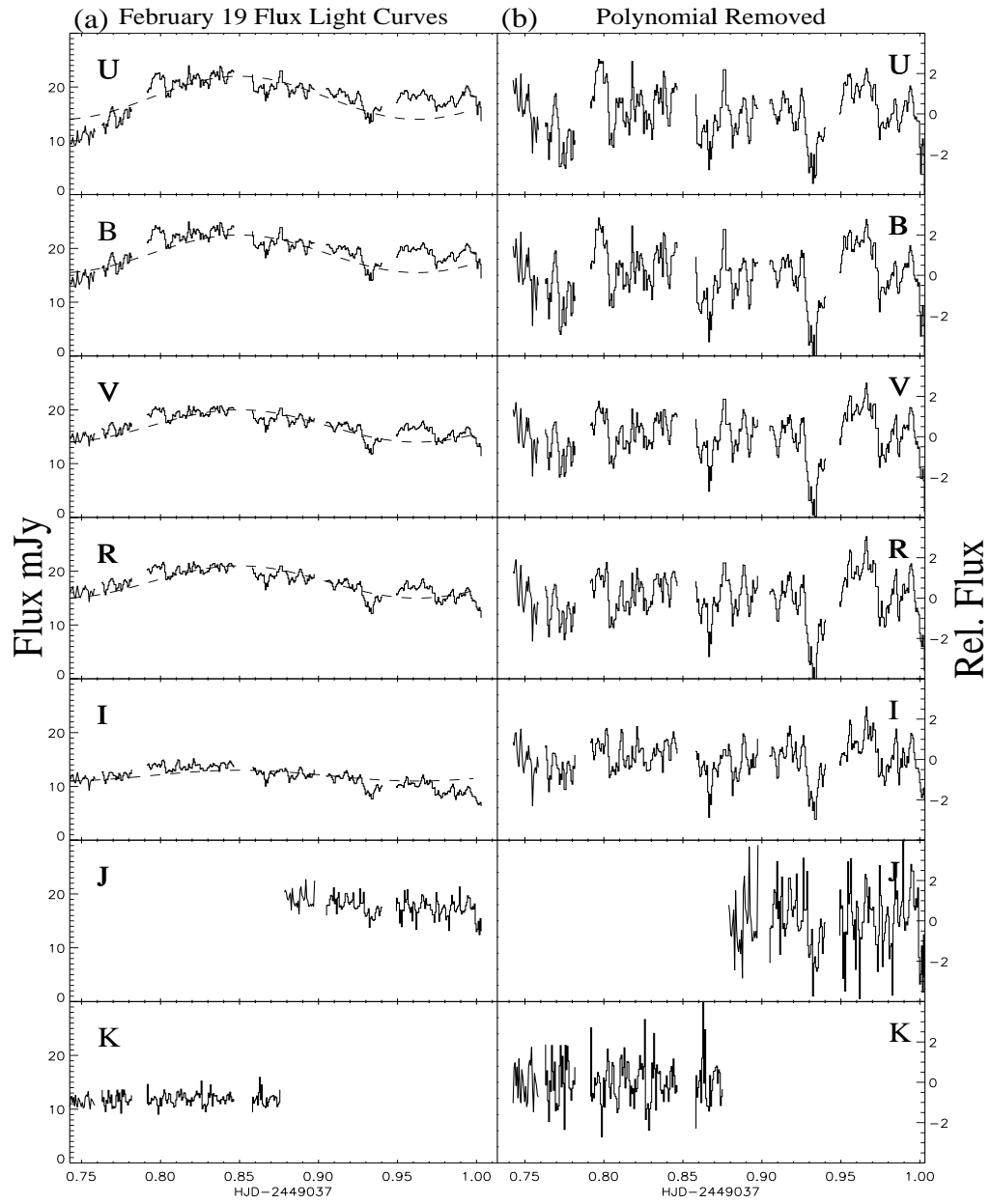
Figure 3.2: As for Fig. 3.1 but for the night of 1993 February 19.

Table 3.1: Times of maxima and minima used in calculating the residuals
in Fig. 3.3

Maxima (HJD)	Minima (HJD)	Reference
2449019.496	2449037.502	Hilditch and Bell (1994)
	2449301.884	Hellier et. al. (1994)
2449036.95	2449036.81	This paper
2449037.836	2449037.96	This paper

Orbital Period Search
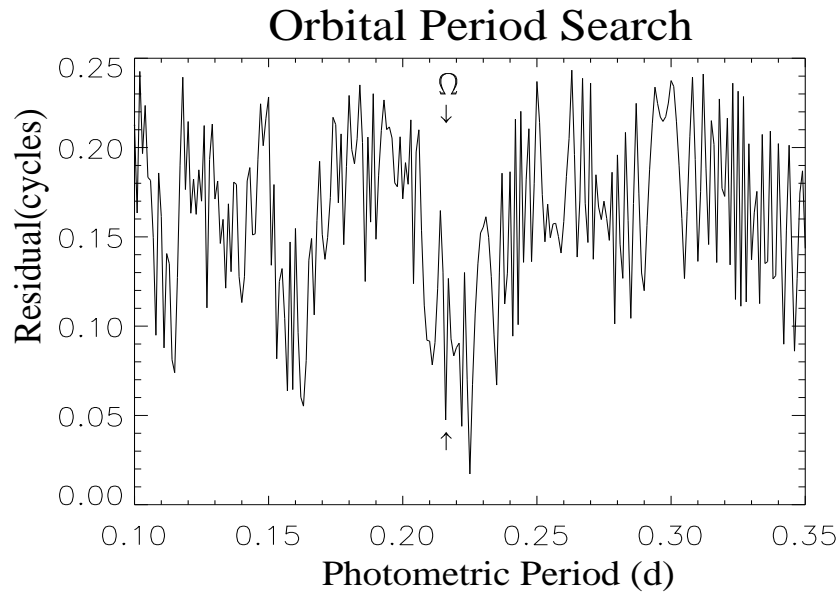
Figure 3.3: Period search among the orbital timings. Ω marks the orbital
period (0.216d) from Mason 1995, Hellier et al. 1994.
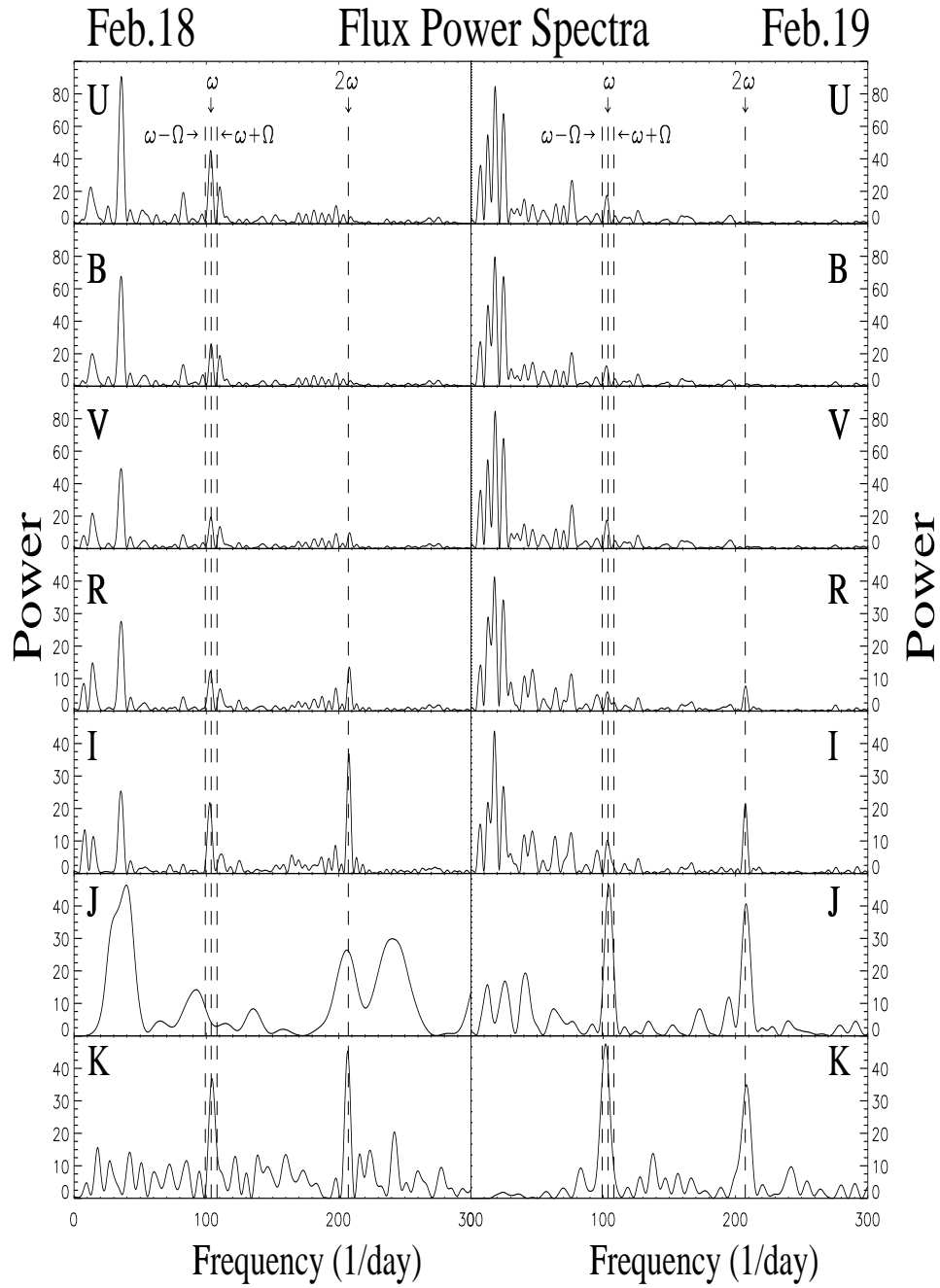
Figure 3.4: Power spectra of the intensity, both days shown side by side. Ω and ω are the orbital and spin frequencies respectively
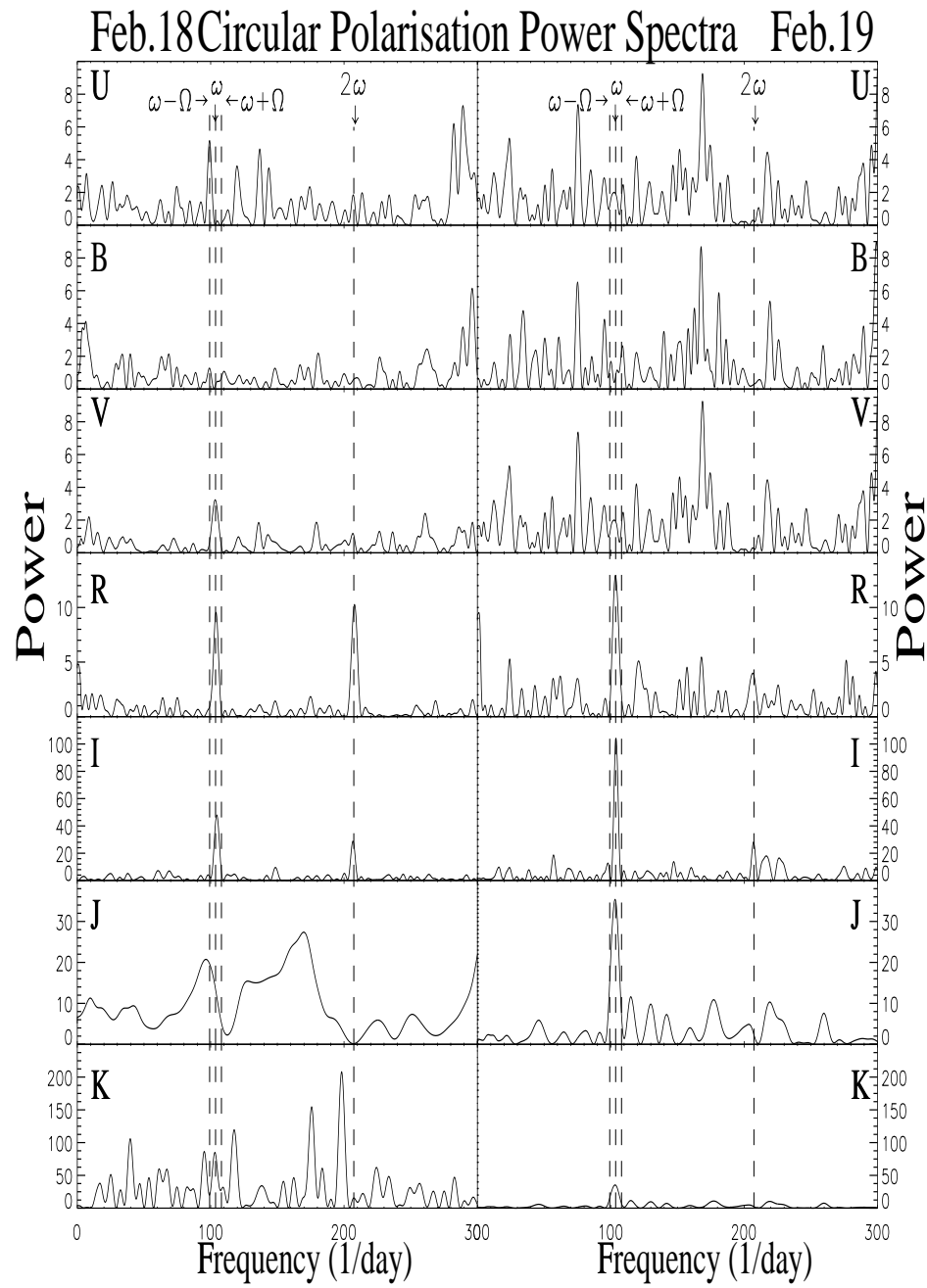
Figure 3.5: As for Fig. 3.4 but for the circular polarization

resolution of 0.001 day. A minimum dispersion in O-C was obtained by varying both the period and epoch. The result is seen in Fig. 3.3, which shows the most prominent dip at 0.225 day (5.4hr), consistent with the spectroscopic period of 5.5 hours (M92) and with the 5.3 hour period calculated from the suggested 14.5-min beat period (Rosen, Mittaz & Hakala 1993). However, other estimates of the orbital period so far gave 5.18 ± 0.01h (0.216d, Mason 1995, Hellier et al. 1994). A dip at this period also occurs in the O-C plot and is labelled in Fig. 3.3. The photometric variation therefore probably occurs at the orbital period so I have superimposed sinusoids of this period on both days observations in Figs. 3.1 and 3.2.

A 3rd order polynomial was subtracted from each band in order to remove these long period variations and the power spectra calculated after applying a cosine bell apodisation. Power spectra of the intensity and of the circular polarization from both days of observations are shown in Figs. 3.4 and 3.5 (ω, Ω are the spin and orbital frequencies respectively). On both days the intensity power spectra (Fig. 3.4) show the 13.9 minute spin period in all of the wavebands and strongest in the I and J bands. However the harmonic at 6.95 minutes becomes prominent only at wavebands longward of the V band and is almost absent in the bluer wavebands. The power in the 14.5 minute synodic beat modulation is very small. (there may also be power at ($\omega + \Omega$) on February 18.) Prominent longer periods are visible at frequencies of ~ 30 cycles per day in both power spectra particularly at the shorter wavelengths. One of these peaks occurs at approximately three times the spin period but only in the first day's observations. The window function is single-peaked and shows no

power at these frequencies. Such features were also seen in the light curves of the polarized intermediate polar, BG CMi, by Patterson & Thomas (1993), who went to considerable lengths to explain them. Their conclusion (hedged with health warnings) was that the spin period of BG CMi may be double that previously considered (eg. by Norton et al. 1992). Periods in this frequency range have previously been explained as being related to the orbital period and caused by tidal resonances between the secondary and the accretion disk (Whitehurst & King 1991, Hirose & Osaki, 1990). However this results in periods which are too long to fit in with a 5.18 hour orbital period of PQ Gem. The resolution of the power spectra is insufficient to pursue this, so I note the prominence of these periods at shorter wavelengths in the data, and suggest that these periods may be a characteristic phenomenon associated with the polarized IPs.

In Fig. 3.5 I have plotted the power spectrum of the percentage of the circularly polarized light. The longer periods in the intensity power spectra are not visible in the circular polarization, suggesting a non-cyclotron origin for these peaks. However the 13.9 minute period and the 6.95 minute period are clearly present. The 13.9 minute period is particularly apparent in the R and I bands on both days and evident from the V band through to the infrared bands. There may be significant circular polarization periodicity at the 14.5 m beat period in the U band on February 18. Other significant periods may be present in the data (for example at ~ 200/day in the K band polarization data on February 18) but their interpretation is unclear.

Figure 3.6 shows the photometry and circular polarization from both days folded on the 13.9 minute spin period with the ephemeris $HJD_{min} =$

$2448173.9570 + 0.00964587554 N_{cyc} + 5.0 \times 10^{-13} N_{cyc}^2$ (Mason 1997). The top two panels also show the soft X-ray light curves plotted on the same ephemeris for comparison. The R, I, J and K intensity bands are double–peaked with the dip at spin phase $\phi_{spin} \sim 0.1$ being more prominent in the K band and not visible in the U and B bands where the light curve is sinusoidal. A second dip at spin phase $\phi_{spin} \sim 0.6$ shows little wavelength dependence. Both positive and negative circular polarizations are detected on the spin period, most notably in the I band. The peak in the positive polarization occurs at spin phase $\phi_{spin} \sim 0.6$ with the peak in the negative polarization occurring at spin phase $\phi_{spin} \sim 0.4$. However the maximum in the negative circular polarization at spin phase $\phi_{spin} \sim 0.4$ can be interpreted as being shifted slightly later in phase by a dip superimposed at phase $\phi_{spin} \sim 0.2$ where the maximum would otherwise have occurred. The J intensity has the greatest modulation amplitude (maximum-minimum flux) of ~ 2.5 mJy, the other bands all having similar modulation amplitudes of ~ 1 mJy. Modulation amplitudes for the circular polarization are greatest in the I and J bands ($\sim 2\%$) and rapidly tend to zero for the other bands.

3.4   Cyclotron Model Fitting

3.4.1   The Model

I have used the grid of calculations, discussed in the previous chapter (Wickramasinghe and Meggitt 1985, WM85), to model the light curves and its polarizations. To re-cap, it was first necessary to calculate the viewing angle i.e. the angle between the line of sight and the magnetic

field line where the emission emanates. This was done by using a dipole magnetic field for the white dwarf together with a system inclination and inclined dipole parameters describing the location of the magnetic dipole with respect to the spin axis of the white dwarf (see Cropper 1989, chapter 2). Then for a given magnetic longitude and latitude of the emission point on the white dwarf, the viewing angle was obtained for different phases of the spin cycle. The shock was assumed to be uniform with a constant temperature and density. The local magnetic field strength was then calculated and subsequently the local optical depth parameter. The intensity spectrum and percentage of circular and linear polarization can then be obtained from interpolating on the grids. Extended sources, such as arcs and comma shapes, are modelled by summing the components of many such emission points as a function of spin phase.

3.4.2   Fits to the data

In the convention used in this thesis (chapter 2) the magnetic latitude (θ) is measured from the magnetic pole in the hemisphere most pointing towards the observer. Therefore the magnetic equator is at a magnetic latitude of $\theta = 90^\circ$ and the magnetic pole in the hemisphere pointing away from the observer is at a magnetic latitude of $\theta = 180^\circ$. Magnetic longitude (ψ) is measured in an anticlockwise direction from the line joining the magnetic pole and the spin pole of the white dwarf as it rotates in a clockwise direction. The magnetic dipole offset angle (β) is the angle between the spin axis and the magnetic axis of the white dwarf (see figure 2.3).

   In modelling the light curves I have used the $\Lambda = 10^7, kT = 10\text{keV}$ grid
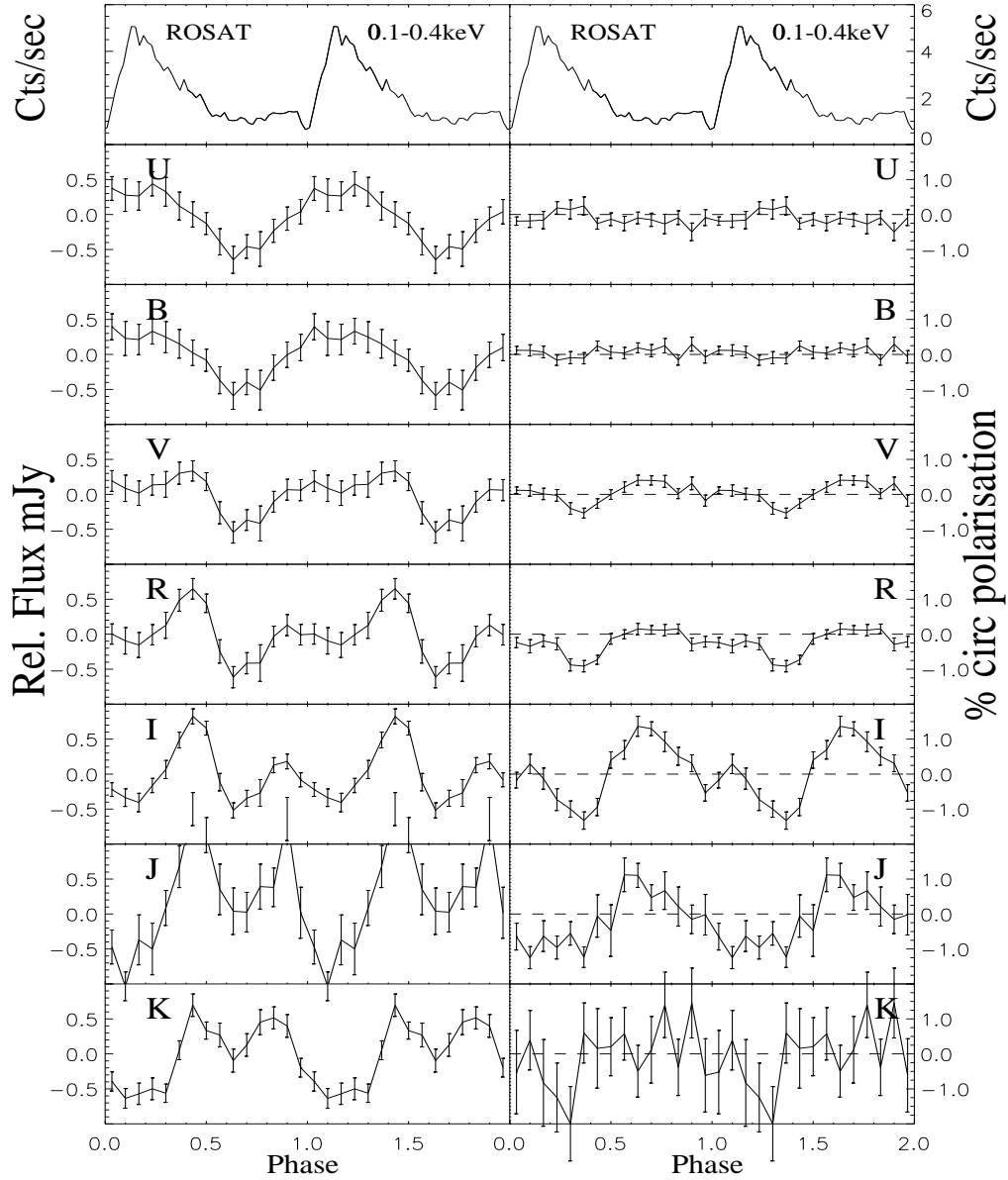
Figure 3.6: Photometry and circular polarimetry of PQ Gem plotted against the phase of the 13.9 minute spin period with the ephemeris $HJD_{min} = 2448173.9570 + 0.00964587554 N_{cyc} + 5.0 \times 10^{-13} N_{cyc}^2$ (Mason 1997). The top two panels show the ROSAT soft X-ray light curves taken from Mason (1995).
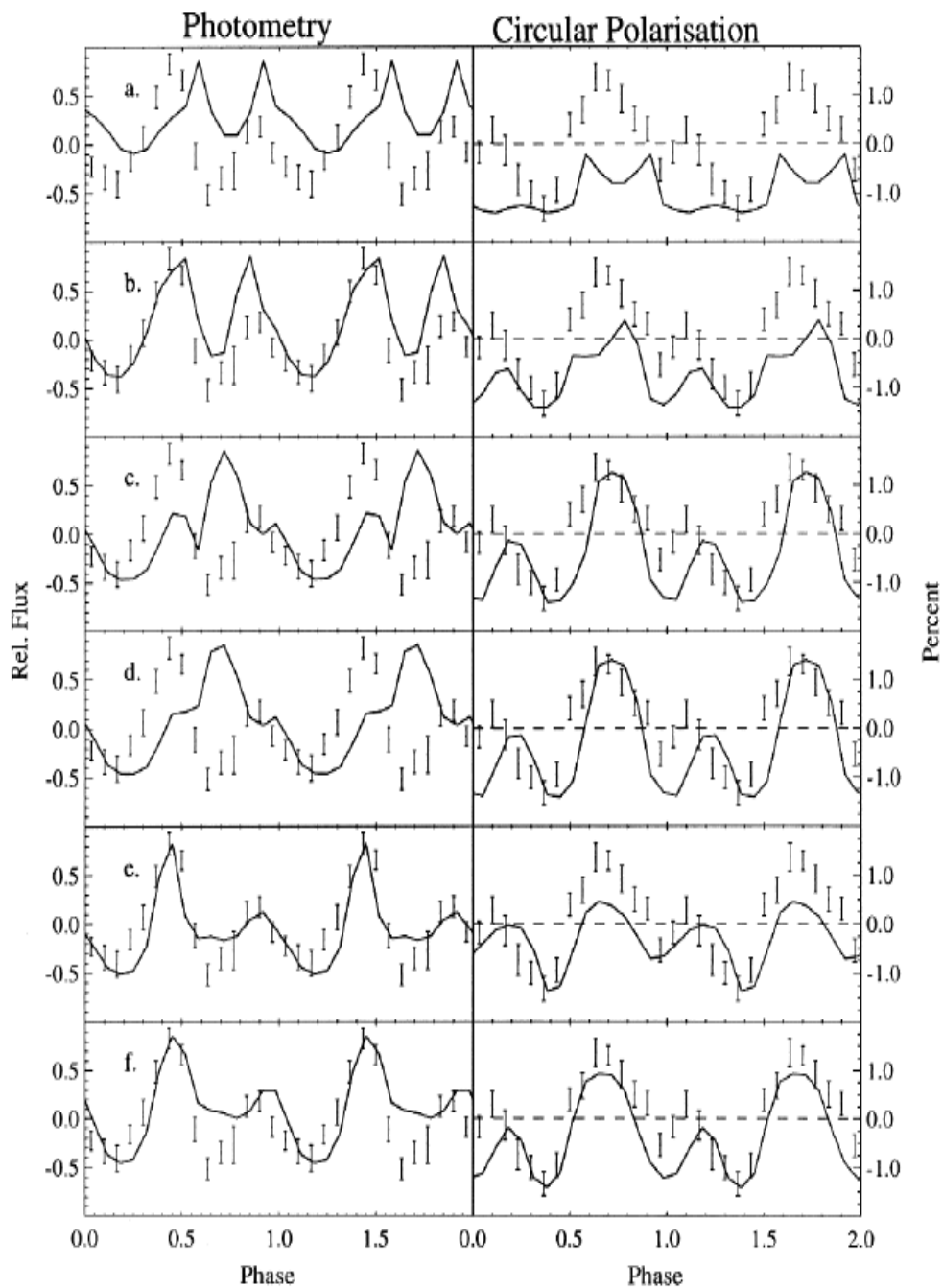
Figure 3.7: Different model fits to the I Band intensity and circular polarization folded on the 13.9 minute spin period. **(a)** Point source accretion. **(b)** Offset point source accretion. **(c)** Arc shaped accretion geometry. **(d)** Arc produced by accretion from a disc **(e)** Extended arc shaped accretion geometry. **(f)** Different size accretion arcs
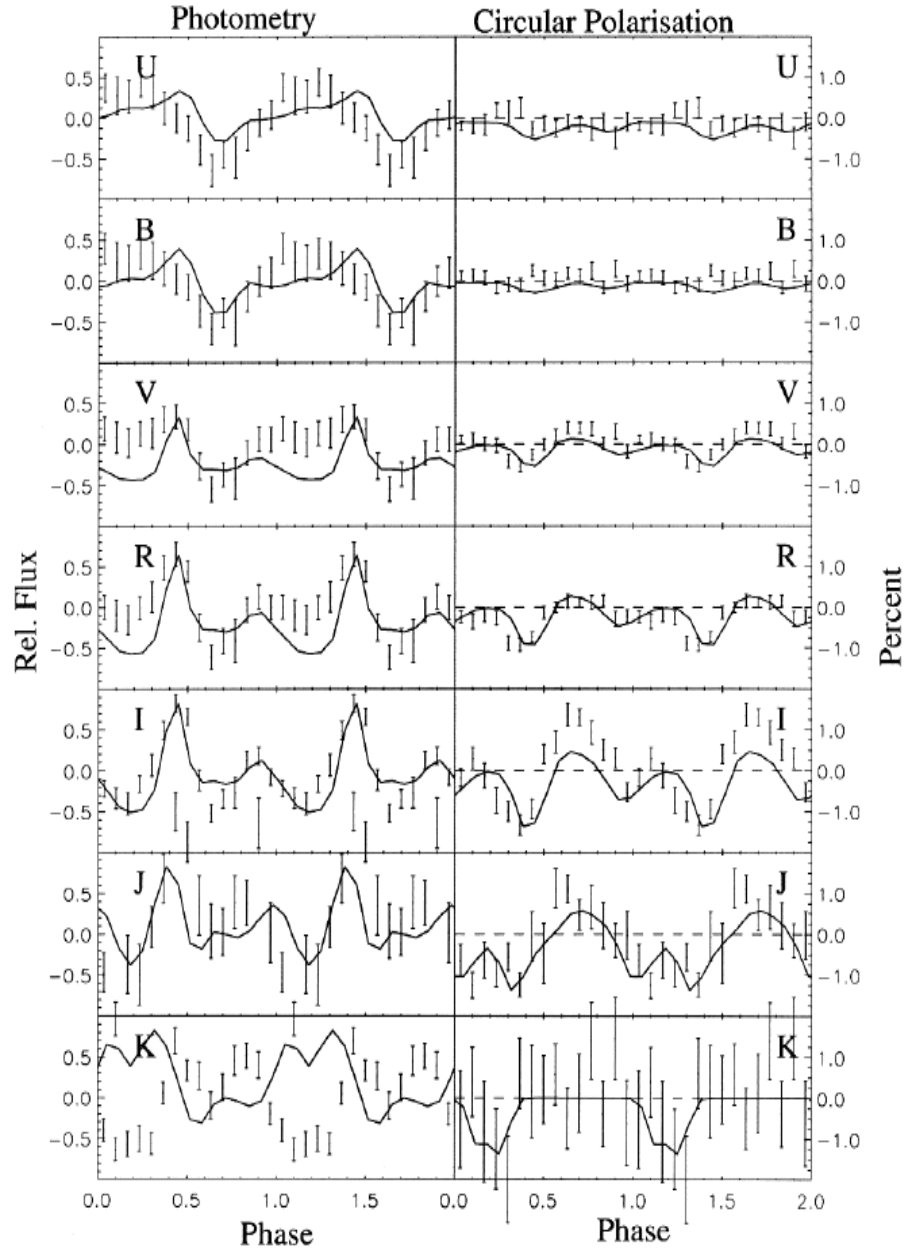
Figure 3.8: The model fit to the multiwavelength photometry and circular polarization using the parameters derived for the I–band. The best fit was obtained for an inclination of $60°$ and a magnetic dipole offset at an angle of $30°$
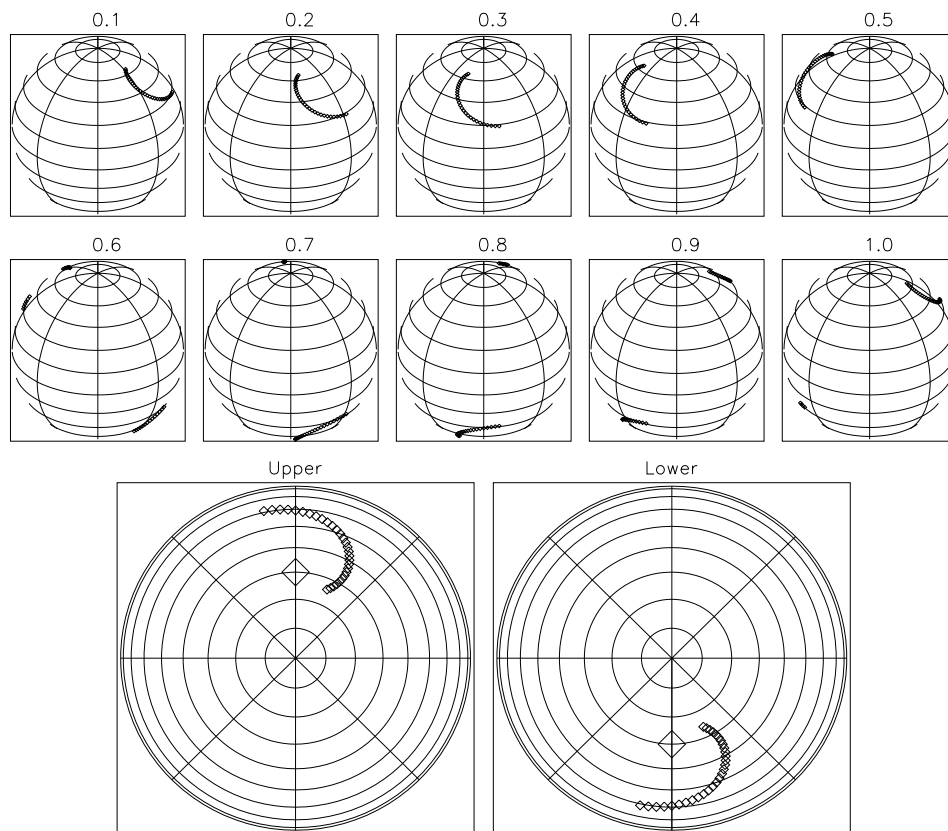
Figure 3.9: Illustration of the model used to compute the curves in Figs. 3.7 and 3.8. The bottom two globes give the view as seen from directly above the top and bottom spin poles respectively. The large diamonds mark the magnetic poles.
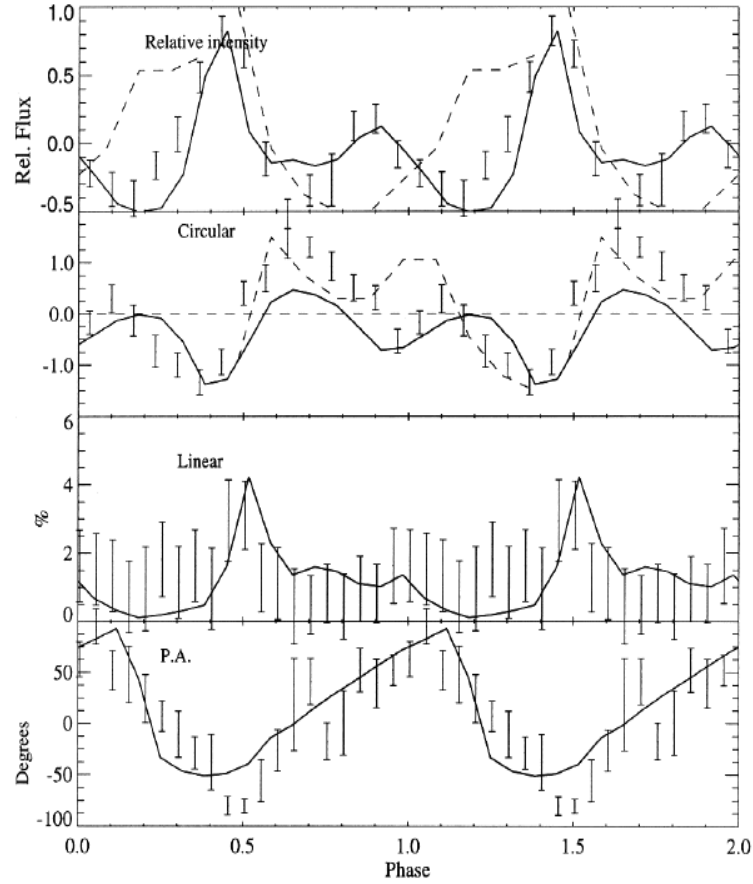
Figure 3.10: The model fit (including the linear polarization and posi-
tion angle predictions) to the I band photometry and circular polarization
(solid line) compared to the Piirola et al. (1993) model fit (dashed line).
The linear and position angle observations are taken from Piirola et al.

of calculations with a field of $B = 14$MG at the magnetic pole (see chapter 2). These values were chosen to give a best fit for all the wave bands simultaneously. Local values for Λ and B were calculated as in chapter 2. The light curves were modelled by summing the contributions of the harmonics that appear in the wavelength range of interest.

The presence of both negative and positive circular polarizations for large fractions of the spin cycle suggests that emission is from two extended regions located near the magnetic poles of a magnetic dipole on the white dwarf's surface. Figure 3.7 shows the process of model development compared to the I band observations. I keep the polar magnetic field strength constant and in each case adjust the inclination and magnetic dipole offset angles and the parameters describing the shape of the arcs to obtain a best fit. In Fig. 3.7a I compare the prediction for the best point source model which has two emission regions diametrically opposed on the star. This is not a good fit but it gives a starting point in calculating the inclination and magnetic dipole offset of the system. To reproduce the correct separation of the observed intensity peaks I found it necessary to move the emission points ahead of the magnetic poles, introducing a tilt to the field lines (Fig. 3.7b). However point sources still produce models that are too symmetrical with phase. Fig.3.7c shows the effect of moving from point sources to arcs at constant magnetic latitude, which makes it possible to reproduce the gross features of the circular polarization curve. This is physically unlikely in almost any case, so in Fig. 3.7d I show the model light curves that would occur from an emission geometry defined by magnetic field lines fed from a disc at a constant radius from the white dwarf. This geometry has the arc closest to the magnetic pole at

its center and extends further away from the magnetic pole at its extremities. This does not improve the fit significantly, so I found it necessary to extend the arcs further towards the magnetic equator to decrease the peak at spin phase $\phi_{spin} \sim 0.7$ and reproduce the intensity peaks in the right proportions. This is shown in Fig.3.7e. Finally I explored the effect of allowing the accretion arcs in the two hemispheres to have different sizes (Fig.3.7f). The formal fit quality is slightly improved by allowing the lower arc to be bigger, but this is not at a level which I would regard as significant. Therefore I use the model shown in Fig.3.7e as the basis for what follows.

While I cannot be sure that the model fit is unique, these predictions reproduce the main features that appear in the observations. What is clear is that it is necessary to place the arc ahead of the magnetic pole to reproduce the asymmetry shown in the phased observations. When the arc is placed behind the magnetic pole the asymmetry is reversed. This has implications for the accretion torques on the white dwarf and therefore its spin evolution (Mason 1997).

Figure 3.8 shows the best fit to all wavebands simultaneously obtained for a system with an inclination of $60°$ and a magnetic dipole offset angle of $30°$. This uses the same parameters as in Fig.3.7e but with the choice of Λ and B modified slightly to optimise the fit. The model calculates the curves for each band simultaneously using the same parameters in all bands. Slightly different values for the dilution factor, to simulate light from other sources in the system, are permitted in each band but are kept at a constant value over the spin cycle within each band. The dilution factor increases slightly towards the shorter wavelengths as would

be expected if the cyclotron component is most prominent at the red and infrared wavelengths and the light from other regions in the system increases towards the blue. The model reproduces the wavelength dependence of the intensity dip at spin phase $\phi_{spin} \sim 0.1 - 0.2$. There is no dilution of the circular polarization curve however, which is of purely cyclotron origin and the model provides a single consistent solution for all bands.

The arcs used in the model are shown in Fig. 3.9. The accretion region in the hemisphere facing the observer emits the negative polarization. The arc is extended in magnetic longitude between $\psi_1 = 60°$ and $\psi_2 = 200°$ and is located at a magnetic latitude of $\theta_1 = 12°$ for ψ_1. It is elongated towards the magnetic equator by an angle of $\Delta\theta^* = 20°$ so that the trailing edge of the arc has a latitude of $\theta_2 = 32°$.

Positive polarization is emitted from an accretion arc placed symmetrically at the opposite magnetic pole on the lower hemisphere.

For completeness I have compared the linear polarization and its position angle predicted by the model in Fig.3.8 with the I-band linear polarization observations of Piirola et al. (1993). This is shown in Fig. 3.10. The model is consistent with the marginal peak in linear polarization at spin phase $\phi_{spin} \sim 0.5$ in the Piirola et al. data and correctly predicts the position angle of linear polarization variations. The linear polarization peak occurs when the upper and lower emission regions pass over the limb of the white dwarf.
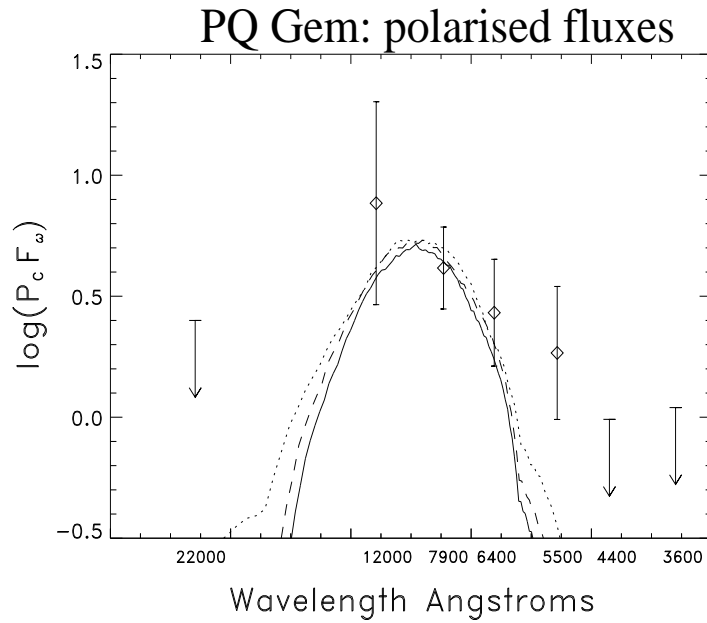
Figure 3.11: Observed total circular polarized fluxes of PQ Gem compared with model predictions. The solid line gives fit to a $kT = 10\text{keV}$ $\Lambda = 10^7$ constant temperature model with a field of $B \sim 14\text{MG}$ and accretion geometry as given in Fig. 3.9. Using the same accretion geometry I also show model curves with $\Lambda = 10^5, B \sim 21$ and $\Lambda = 10^6, B \sim 16.5$, dot and dashed curves respectively.

3.4.3   The magnetic field

I have also deduced the polarized fluxes $F_c = P_c F_{tot}$ (where P_c and F_{tot} are the percentage of polarized flux and total flux respectively) which are independent of any unpolarized additional background such as emission from the accretion stream, the possible disc and bright spot, reprocessed X-rays and stellar light. The polarized fluxes are compared with the cyclotron models of Wickramasinghe and Meggitt (1985) in Fig. 3.11. The observed polarized fluxes were obtained by summing the total amount of polarized flux over the entire spin cycle. Consequently, in modelling the cyclotron spectrum I summed the emission over the entire spin cycle. The shape of the polarized continuum is not well predicted by the model. I found when using the 10KeV, $\Lambda = 10^7$ model calculations of Wickramasinghe and Meggitt (1985), that the best fits were obtained for a magnetic field strength of 14.0 MG. Similarly good fits are also obtained with $\Lambda = 10^5$ and $\Lambda = 10^6$ but with higher magnetic field strengths: for example for $\Lambda = 10^5$, the optimal field is 21.0 MG and for $\Lambda = 10^6$ the optimal field is 16.5 MG. These alternatives are also shown in Fig. 3.11. It is unclear from the structure of the accretion region I have derived (from the polarization curves) what values are appropriate. Wickramasinghe, Wu & Ferrario (1991) have used $\Lambda = 10^8$ derived from more self-consistent modelling of accretion arcs in intermediate polars. I have been limited by the published grid of models from extending the fits to higher values of Λ, but extrapolating from the values used, it is clear that such a fit would result in even lower values for the magnetic field strength. From my modelling of the light curves (Fig. 3.8) I find that the quality of the fit is improved with the lower values of the magnetic field strength.

3.5 Discussion

3.5.1 Implications of the model fits

The intensity light curves of PQ Gem can be explained as the combination of emission arising from the vicinity of both magnetic poles, with positive and negative polarizations arising from emission regions located at opposite ends of the magnetic dipole.

My model explains the dip in the negative circular polarization at spin phase $\phi_{spin} \sim 0.1 - 0.2$ (Fig. 3.8) as absorption or scattering of the cyclotron radiation by the accretion stream. This results in depolarization of the cyclotron radiation from the pole in the upper hemisphere as the accretion region crosses closest to the line of sight (Meggitt and Wickramasinghe 1982)(Fig.3.9). At the same phase the other accretion region on the lower hemisphere of the white dwarf crosses over the limb resulting in a dip in the intensity. Dips have been observed in *GINGA/ASCA* X-ray light curves (1-2 KeV and 4-10 KeV) and in softer X-ray (0.1-0.4 KeV) *ROSAT* light curves (Mason 1995) at similar spin phase. In Figure 3.6 I have plotted the soft X-ray light curve on the same ephemeris as the photometry and circular polarization. My model is therefore consistent with Mason's (1995) suggestion that the dips result from absorption by dense material crossing the line of sight to the emission region.

The positive circular polarization peaks at spin phase $\phi_{spin} \sim 0.7$ when the accretion region in the lower hemisphere crosses closest to the line of sight. This does not show an absorption dip because of the larger angles the magnetic field lines make to the line of sight. The dip in the intensity at this phase is due to occultation by the white dwarf of the main emitting
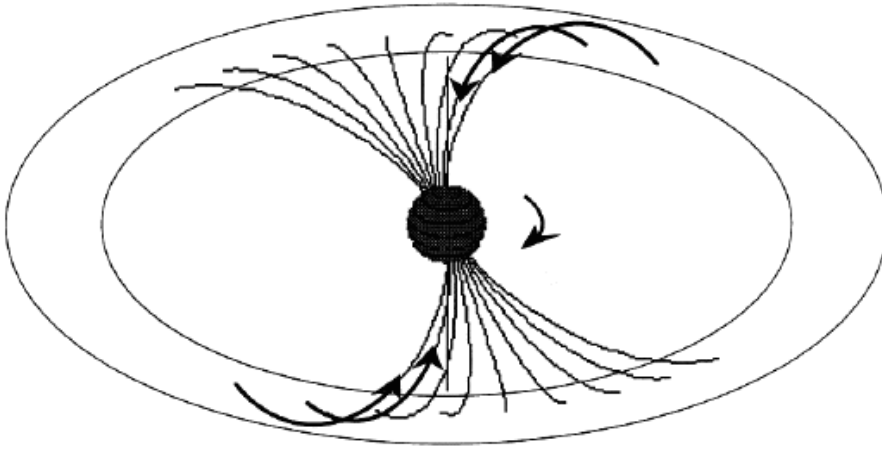
Figure 3.12: Illustration of the accretion disc and magnetic field lines of the white dwarf.

region in the upper hemisphere, and therefore appears in all the wavebands.

Note that my model is the inverse of that proposed by Piirola et al. (1993), who place the accretion region closest to the line of sight in the *lower* hemisphere at my spin phase $\phi_{spin} \sim 0.1 - 0.2$. This lower pole is responsible for the negative polarization seen at this phase. From their modelling of the Piirola et al.(1993) data, Väth et al. (1996) deduced a similar model to that by Piirola et al.(1993). I have added the Piirola et al. (1993) model fits to Fig. 3.10 for comparison. It is clear that, in addition to being more consistent with the X-ray observations, my fits provide a more accurate representation of the polarization data.

3.5.2   Disk Threading

These observations provide an insight into the manner in which accreting material couples onto the field lines in asynchronous magnetic CVs. As noted above, it was necessary to model the observations using arcs placed ahead of the magnetic pole. This indicates that material couples to field lines threading the inner edge of the disk ahead of those directly below the magnetic pole (Fig. 3.12). The details of this interaction are complex (see eg. Li et al. 1996) but simple geometry suggests that these field lines are optimally presented to the material in the inner edge of the disk only if the angular velocity of the magnetic field is greater than that of the disk material. The bulk velocities of the material in this region are more aligned with the field line directions, making it easier for the material in the disk to be threaded. In practise one can expect that the field lines will be distorted in the plane of the disk by the drag imposed by the more slowly rotating material, but even so, the field lines ahead of the magnetic pole will be better presented.

The situation described above is one in which material couples at radii larger than the co-rotation radius. Thus one would expect deceleration torques acting on the white dwarf (Ghosh & Lamb 1979, Li et al. 1996), causing spin down. Indeed, such a spin down on time-scales of $\sim 2 \times 10^5$ yr has been found by Mason (1997).

A further consequence of my modelling is clear from a comparison of Figs.3.7d and 3.7e in which significantly better fits are obtained when the arcs are extended towards the orbital plane. The implication of this is that material has to thread from a range of radii linked to the azimuth angle. More detailed study may yield further significant insights into the

way the field interacts with the material in the disk.

3.5.3   Orbital Variations

Significant variation is seen on the orbital period in Figs. 3.1 and 3.2, especially in the U and B bands. The blue colour and sinusoidal nature of this variation suggests that its origin is the 'bright spot', the region where the stream impacts on the outer edge of the disk, as in Dwarf Novae such as U Gem (Krzeminski 1965). However, the variation seen here is somewhat more sinusoidal than in Dwarf Novae, either the result of a lower inclination or because the region is more extended in PQ Gem. IPs as a class show various degrees of smooth orbital variation (see the discussion in Warner 1995 section 7.3.2). If the variation is due to an illuminated bright spot, then from the trajectory of the stream one would expect the bright spot to be at inferior conjunction at orbital phase $\phi_{orb} \sim 0.4$. This is in agreement with the definition of the orbital phasing in which inferior conjunction of the secondary is defined to be at orbital phase $\phi_{orb} \sim 0.5$.

3.6   Conclusion

The spin folded light curves from the X-ray to the infrared can be interpreted in the following way:

The highest energy X-rays, observed using *GINGA*, show the most straightforward shape, when folded on the spin period. It is single peaked and quasi-sinusoidal. The maximum occurs when the emission region is facing the viewer just after phase $\phi = 0$. Thus these hardest X-rays are thought to arise from the shock heated gas that is settling onto the sur-

face of the white dwarf. This is the relatively unabsorbed kT∼ 20keV bremsstrahlung component. At slightly lower energies, but still relatively hard X-rays, the light curve is cut into by a dip feature as can be seen in the ASCA X-ray light curves between 1 and 10 keV. The quasi-sinusoidal variation is not so pronounced at these energies.

At even lower X-ray energies (below about 0.4keV), as observed by *ROSAT*, the emission is thought to be dominated by the 50 eV blackbody component from the heated photosphere at the footprints of the accretion column. The dip becomes narrower and the light curve takes on a saw-tooth shape. The modelling presented above has the stream feeding the emission region pointing towards the observer just before phase $\phi = 0$. Thus this would explain the energy dependent X-ray dip and the rapid increase in the X-ray flux from its minimum to its maximum in less than about one tenth of a phase. i.e. the narrow accretion stream uncovers its heated footprint at the base of the accretion column very quickly. Also the X-ray dip does not coincide exactly with the maximum in the hard X-ray light curve but in fact is slightly earlier. This suggests that the stream is impacting onto the surface of the white dwarf at some inclined angle pointing in the direction of rotation of the white dwarf. This is also borne out in the cyclotron modelling presented above.

In the optical towards the infrared one can again see an energy dependent dip at phase $\phi \sim 0$. The cyclotron modelling above predicts this as absorption of the cyclotron radiation that peaks in the red and infrared bands. When the opacity increases as the accretion stream comes into the line of sight, a dip also arises in the negative circular polarization as a result of absorption or scattering of the cyclotron radiation result-

ing in depolarization in the emission. Half a spin phase later there is a peak in the positive polarization as the emission region in the lower hemisphere is best presented to the viewer. The U and B-band light curves are strongest at phase $\phi \sim 0$ and approximately in phase with the hard X-ray modulation, probably arising from the hotter photosphere beneath the accretion flow. The U and B-band light curves are also dominated by the ~ 14.5 minute beat period of the system suggesting a reprocessing site of the X-ray emission somewhere in the binary frame or possibly the bright spot.

The model also explains the linear polarization peak observed by Piirola et al. (1993) with a fairly good fit to their position angle observations (Fig. 3.10). The best fits of the model place the emission arcs ahead of the magnetic poles suggesting that material preferentially attaches to field lines which lead the magnetic pole. The torques produced by the interaction of the white dwarf's magnetic field with the accreting material would then act to slow down the rotation of the system. Mason (1997) has reported such an increase in the spin period of the system.

My modelling estimates the magnetic field at the poles to be in the range $B_p \approx 9 - 21$ MG in agreement with Väth et al. (1996) and Piirola et al. (1993). This determination based on the continuum polarized fluxes of PQ Gem depends on the optical depth parameter assumed for the accretion region. However my simultaneous cyclotron modelling of the multicolour observations give best fits for a magnetic field at the lower end of this range.

This relatively strong magnetic field maybe what is required to funnel the accretion flow onto a small surface area of the white dwarf. The

strong soft X-ray emission could then be explained as emission from a heated photosphere at the base of the accretion column. Not all IPs show a strong soft X-ray emission (Harberl & Motch 1995). The angle dependence of the polarization effects and the narrow dips in the X-ray light curves seem to suggest that the accreting material is indeed funnelled. The shapes of the accretion regions described above are also an indicator of how material attaches to the field lines of the white dwarf. My modelling suggests that disk material is being 'scooped up' beyond the corotation radius which is consistent with the reported spin down in PQ Gem by Mason (1997).

Chapter 4

'Stokes Imaging' of the accretion region in Magnetic Cataclysmic Variables

4.1 Introduction

Modelling the polarized cyclotron emission from MCVs has been a pivotal technique for determining the structure on the accretion zones on the white dwarf. To date model solutions, such as those in chapter 3, have been obtained from trial fits to the intensity and polarization data which have been constructed from emission regions (for example arcs and spots) put in by hand. These models were all inferred indirectly from arguments based on the polarization and X–ray light curves.

In chapter 2 I introduced such a model which describes cyclotron radiation and its polarizations from accretion regions of various shapes lo-

cated near the magnetic poles on the surface of a white dwarf. In section 3.5 the model was used to fit the polarization light curves from the intermediate polar PQ Gem. It was found that emission from two symmetrically extended arcs best described the observations. However, the fit was obtained by a trial and error approach using a variety of inferences from the intensity and polarization data. Obviously a more self consistent, analytical and objective method of modelling the polarimetric data is required.

In the past decade several authors have modelled the polarized cyclotron emission from the shock regions in MCVs. However, it was found very early on that it is too simplistic to assume that accretion takes place over a small circular cap at the magnetic pole: many authors (e.g. Potter et al 1997; Wickramasinghe & Ferrario 1988; Beuermann, Stella & Patterson 1987; Cropper 1986) have found that the region must be extended into an arc or comma shape and offset from the magnetic pole in order to explain the shape of the polarized cyclotron light curves. Wickramasinghe et al. (1991) provides a good example of how high signal–to–noise ratio observations can be modelled in detail. Until now, the parameters that define the shape and location of the emission regions have been adjusted by a trial and error approach until the model gives a good fit. however, the number of free parameters describing the shape and location of emission regions becomes very large.

Cropper & Horne (1994) used the maximum entropy method to map the emission region in the AM Her system ST LMi using optical photometry and X–ray light curves. They found that the resulting maps of the emission region in ST LMi showed structure within a more extended re-

gion.

Using the polarizations as well as the intensity provides the opportunity to invoke more constraints in order to choose between the many different solutions with identical observational properties produced by modelling only the intensity curves. For example, it is not possible to constrain the extent in latitude accurately with only intensity data and it is difficult to avoid symmetry with respect to the magnetic equator. The combination of circular polarization and linear polarization with its position angle constrain the solutions strongly and eliminate the above problems. Increasingly the quality of polarization data is becoming sufficiently good to give more reliable information for model fitting.

Therefore in this chapter I proceed a step further from the Cropper & Horne (1994) MEM optimisations, and use the cyclotron emission model, developed and described in chapter 2, incorporating the anisotropies of polarized cyclotron emission. This allows modelling of the intensity, circular polarization, linear polarization and position angle data. However, instead of the maximum entropy method and the conjugate gradient optimisation used in Cropper & Horne (1994) I have used Tikhonov regularisation and a Genetic Algorithm (GA) to obtain the best fit to the data and to produce maps of the emission regions.

To demonstrate the success of this technique, I show the results of several simulations in which I have applied the technique to intensity and polarization light curves calculated from arbitrarily shaped emission regions on the surface of a sphere to recover the original test data. I also show how adding artificial noise effects the outcome of the optimisation technique. Finally I demonstrate the success of applying the technique

to multiwavelength test data and show its dependence on the magnetic field strength.

4.2   Optimisation

In this section I give a description of the way the resulting cyclotron emission distribution is constructed. For the optimisation procedure the surface of the white dwarf is divided into a grid of 1740 points each representing a 6 by 6 degree square in magnetic coordinates. Each point on the grid can have a different number of emission points, related to the accretion rate, and thus the optical depth parameter is calculated also as a function of local density. Given the strength and orientation of a dipole field and the system inclination, the Stokes parameters (I, Q, U and V) are calculated for each point along the emission regions and summed to produce the total polarizations (in terms of intensity, circular polarization, linear polarization and position angle) as a function of orbital (or white dwarf rotational) phase. However, obtaining an optimal fit to the dataset is an under-constrained problem. Typical datasets consist of about 30-50 data points over the orbital phase in each Stokes parameter, so there are all together an order 120-200 data points if all the Stokes parameters are available. Therefore, even a very modest map (say 50×100 elements) over the white dwarf surface has about ten times more free parameters than there are data points. It is thus necessary to employ some sort of additional constraint (for example using a regularisation method such as maximum entropy) in order to find a most likely, by some acceptable criterion, solution of the set of underconstrained solutions that fit

the data.

4.2.1   The Fitness Function

The approach I have used is based on Tikhonov regularisation (Tikhonov 1963, Piskunov et al. 1990) for providing the additional constraint. Tikhonov regularisation is an alternative for using an entropy term. In the maximum entropy approach the function to be minimised is of the form

$$F(p) = \chi^2 + \lambda \sum_j p_j \, log \frac{p_j}{m_j} \tag{4.1}$$

where χ^2 is the χ^2 of the fit to the data, p_j is a single emission element on white dwarf surface and m_j is a local geometric mean of the pixels next to pixel j. The sum is over all the surface grid elements j. $F(p)$ is called the fitness function. Minimising this together with a suitable choice of the Lagrangian multiplier λ will produce the maximum entropy solution of the distribution of emission points. Piskunov et al. (1990) have however pointed out that in the case of Doppler imaging, using the Tikhonov functional instead of the maximum entropy functional leads to more consistent solutions in case of noisy data. In this case the fitness function to minimise is

$$F(p) = \chi^2 + \lambda \sum_j \|\nabla p_j\|^2 \tag{4.2}$$

where $\|\nabla p_j\|$ is the mean gradient of the number of emission points at point j.

4.2.2   Genetic Algorithm

To minimise $F(p)$ a robust technique is needed in order to ensure a global rather than local optimisation is achieved. For this I have chosen a Genetic Algorithm (GA - see for instance Charbonneau 1995 and Hakala 1995 for astronomical applications of GA and Beasley et al. (1993a, 1993b) for a good introduction to genetic algorithms). GA is capable of climbing away from local minima. Still, it must emphasised, that the method is not guaranteed to find the global minimum. There are, however, a number of applications where GAs are shown to provide global and more stable solutions than more conventional optimisation methods (Charbonneau 1995). The second advantage is that GA is a 'forward only' approach for inversion problems: one does not have to invert the problem at all, but simply compute solutions based on given sets of parameters. This makes the method very easily applicable to a range of different problems. Also, major changes to underlying models do not require much effort in terms of 're-inverting' the problem.

The GA works by first generating a set of random solutions. The fitness of each solution is then calculated using equation 4.2 and the solutions are then ranked in order of their fitness. The next generation of solutions are then produced by a type of natural selection procedure – the solutions that were ranked best are more probable to breed the next generation. Formally, solutions are selected from the ranked table by using a selection algorithm of the form

$$S_i = INT(\frac{-N_{pop}}{C_s}log(RND(0,1))) + 1, \qquad (4.3)$$

where S_i is the solution rank number after sorting and N_{pop} is the size of

each population. C_s is a scale parameter used to bias the selection criteria more to the best ranked solutions. INT is the INTEGER function and RND is a random number generator. N_{pop} pairs are selected giving one child per pair hence producing another generation of N_{pop}. An offspring is produced by using a uniform crossover technique (Beasley et al. 1993b), i.e. each parameter of the solution is taken from either one or another parent solution. There is also a small probability (usually of the order one in every thousand) that the child solution can be mutated or cloned. The procedure can be summarised in the following steps:

- Generate a set of random solutions (the population), usually about 1000.

- Calculate the fitness of each solution from their χ^2 fit to the data and the regularisation term equation 4.2. Rank the solutions in order of their fitness.

- Generate the next generation of solutions while applying mutation and cloning operators.

- Repeat the last two steps until the fitness does not improve any further.

Eventually the improvement in fitness of the GA solutions will level out and a more analytical approach is required to improve the fit further. For the final approach to minimum the Powell's method is used: this is a line minimisation routine (see Press et al. 1992).

Figure 4.1: The upper curve traces the genetic optimisation. The numbers represent values of λ and the diamonds mark where λ was halved. The lower curve shows the Powell's optimisation. In this case λ is constant and chosen so that the regularisation term and the χ^2 are equal. The asterisks mark equal computation intervals.

4.2.3   Fixed parameters

The optimisation technique makes adjustments to the number density and distribution of emission points on the surface of the white dwarf to improve the model fit of the polarized light curves to the polarimetric data. However, there are also two other types of parameters that are not included in the optimisation technique and are kept constant during a particular optimisation run.

Firstly there are the physical parameters of the system under consideration. These include the inclination, magnetic dipole offset angles (latitude and azimuth) and the magnetic field strength at the poles. Some or all of these parameters are known for a particular system – different fits are made over a range of values for the parameters that are not known. If none of these parameters are known then good fits can be obtained for a large range in each of these parameters. However, if one parameter is known fairly accurately, such as the inclination or the magnetic field strength, then the range in values for the remaining parameters for good fits to be obtained becomes significantly reduced. For example if the inclination is known, then the circular and linear polarization light curves will be more effective in constraining the magnetic dipole offset angles.

Then there are the parameters that control the direction and/or rate at which the GA finds the global minimum. These include the size of the population, mutation probability, cloning probability and the Lagrangian multiplier. I consider each of these in turn.

The population size (the number of solutions that are bred) is simply a scale factor of the number of data points: the more data points to fit, the larger the population size needs to be in order for the optimisation

technique to work. However its exact value depends strongly on the type of problem and can only be obtained by experiment.

A solution can also be mutated by simply randomising some of its array elements. This is a dynamical term: it has a low probability at the start of the optimisation run and gradually increases as the rate at which better solutions are found decreases. A high mutation probability at the beginning of a run only serves to re-randomise the solutions and therefore the better solutions are not bred to the next generations. However, towards the end of an optimisation run, most of the solutions are located somewhere within the global minimum and are therefore very similar. Therefore, increasing the mutation probability at this stage forces the optimisation technique to search further afield.

The cloning probability is not used in this technique and therefore is kept as a small constant. This parameter is in effect an anti-mutation parameter. If given a high value at the beginning of an optimisation run, then it can force the optimisation technique to search in a particular direction. It does this by making identical copies of some solutions for the next generation instead of a combination of two parent solutions.

4.2.4   The Lagrangian Multiplier

The final solution is dependent on the Lagrangian multiplier λ. Ideally one needs to find the largest value for λ consistent with a good fit to the data (equivalent to the smoothest fit to the data). This is ensured by starting the search with large values for λ and gradually decrease it until $F(p)$ no longer improves. The upper curve in figure 4.1 is a plot of the final values (after genetic optimisation) of the two terms in equation 4.2 for

decreasing values of λ. The diamonds mark the points at with the GA stops and subsequently λ is halved. To begin with, for high λ, only the regularisation term is favoured resulting in a high χ^2 (top left of figure 4.1). As λ is gradually decreased the χ^2 is minimised resulting in a higher final value for the regularisation term (lower right of figure 4.1). Eventually reducing λ further has no effect on the final solution and the process comes to a halt (far right of figure 4.1). The solution has been generated along a trajectory in which the globally smoothest possible solution has always been selected.

The final solution from the GA is then used for the Powell's minimisation. λ is then chosen such that $\lambda \sum_i \|\nabla p_i\|^2$ is the same value as the χ^2 term in equation 4.2. This ensures that the search direction is such that the smoothness of the solution and the χ^2 fit to the data are improved simultaneously. If λ is set too high the final solution is a smooth image with a poor fit to the data. If set too low, the χ^2 improves without any significant decrease in the regularisation term. The lower curve in figure 4.1 shows the Powell's method improvement on the GA's final solution. The asterisks represent equal computation time intervals starting from the right where the GA finished.

4.3 Simulations

For the testing of this technique I have generated synthetic Stokes parameter curves with 50 points over the orbital phase (typical datasets have roughly this number). This gives 200 data points to fit (50 for each of the 4 Stokes parameters). In this chapter I use a 6 degree resolution

map on the white dwarf surface, which in turn yields 1740 free parameters (60*29 surface grid elements on the white dwarf surface). I have chosen an approach where the GA population size is 500. The four simulated polarized light curves presented below were produced by calculating the emission that would arise from a point source (figure 4.2a), two point sources (figure 4.3a) and two extended sources (figure 4.4a) in the B-band. The resulting light curves (figure 4.2b, 4.3b, and 4.4b) have infinite signal–to–noise ratio. All cases were given inclinations of $80°$, magnetic dipole offsets of $10°$, magnetic polar field strengths of 60 MG and the polar optical depth parameter Λ was 1.0×10^5.

4.3.1   Point sources

Figure 4.2b shows the model fit (thick smooth curves) to the input test data (histogram curves) produced by a point emission source (figure 4.2a). The technique has clearly reproduced the polarized light curves accurately. The fits are not perfect because the regularisation term smoothes the image solution and hence the sharp peaks in the test data are not exactly reproduced. It has reproduced the self occultation and self absorption dips in the intensity curve, the correct relative brightness of the linear polarization pulses and the double humped positive circular polarization. The variation in the position angle of linear polarization is also accurately modelled – during phases 0.5-1.0 there is little or no linearly polarized flux and hence the position angle variation has no meaning. Also the fit may be somewhat poor at phases where the position angle varies rapidly. This generally happens when magnetic field lines feeding emission regions, cross the line sight to the observer and rapidly 'swing' through $180°$.

Figure 4.2c shows the model prediction for the shape and location of the emission region needed to produce the input data set. The grey scale is a measure of the number of emission points across the surface of the white dwarf. As can be seen from the figure, the optimisation code has accurately located and mapped the size of the emission region. It has also produced the correct number of emission regions and not for example put an emission region in the opposite magnetic hemisphere in an attempt to obtain the correct amount of circular polarization.

The next logical step is then to test the code on test polarization light curves from two such sites located on opposite magnetic hemispheres of the white dwarf. Figure 4.3 demonstrates the result. The two sites produce both positive and negative circular polarizations and the light curves are more complicated. However, the more complicated the polarized light curves get, the more constraints there are for the optimisation code to find the global minimum, because they contain more information.

4.3.2   Extended sources

Figure 4.4b shows the fit (thick smooth curves) to the input test data (histogram curves) produced by two extended sources (figure 4.4a).

As before, the test light curves have infinite signal–to–noise ratio. The optimisation technique has reproduced the complex features arising from the extended regions. These include the extra linear and intensity features such as dips and peaks. It has also correctly modelled both the positive and negative polarized light curves. The linearly polarized light curves and the variation in position angle now extend over the whole period of rotation.
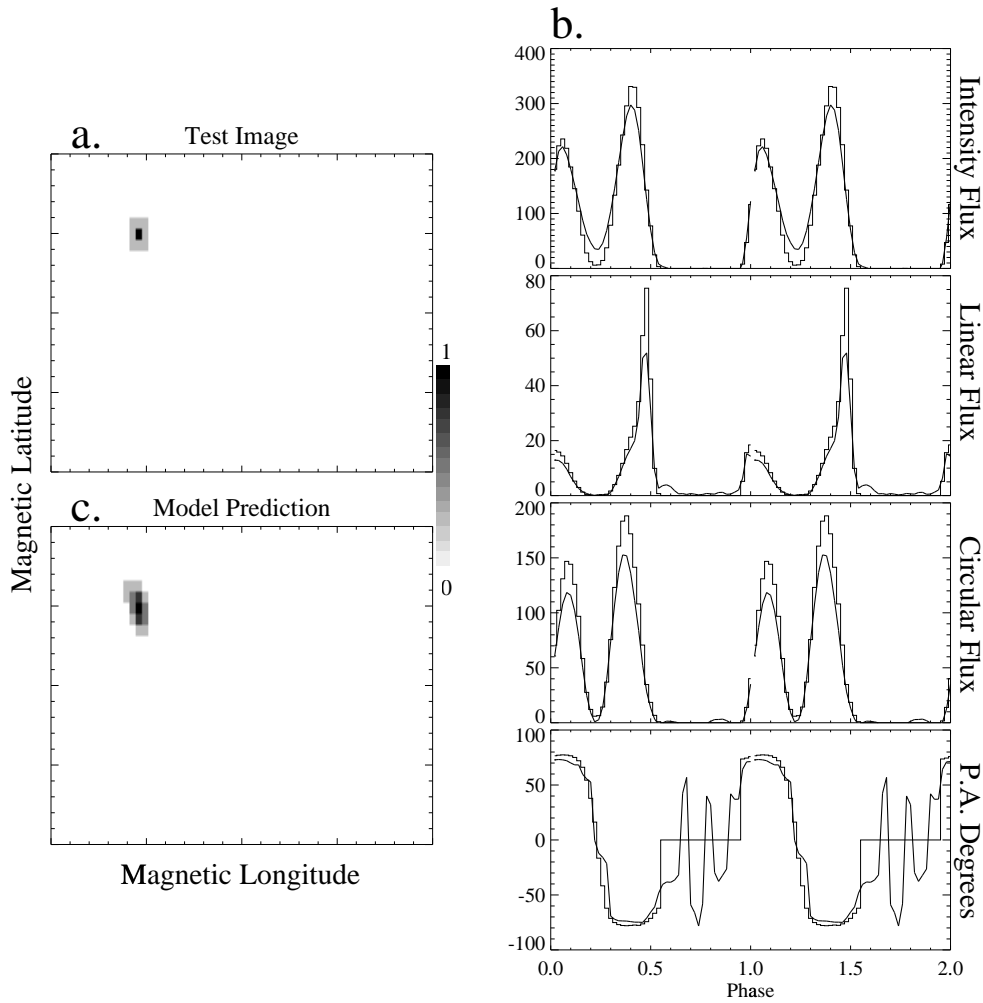
Figure 4.2: Point source: **a.** The emission on the surface of the white dwarf. **b.** The test emission light curves (histogram) and the model fit (solid smooth curve). **c.** The predicted emission region.
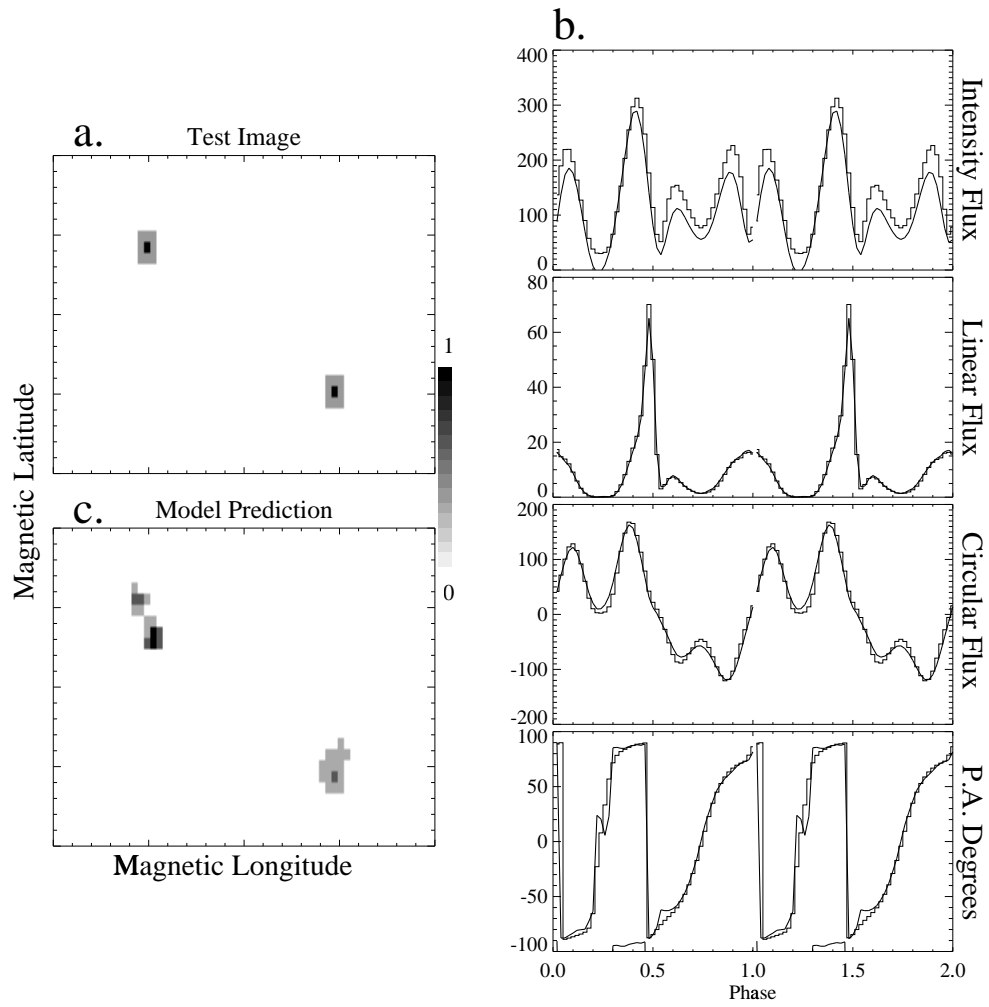
Figure 4.3: As for figure 4.2. but for two point sources.
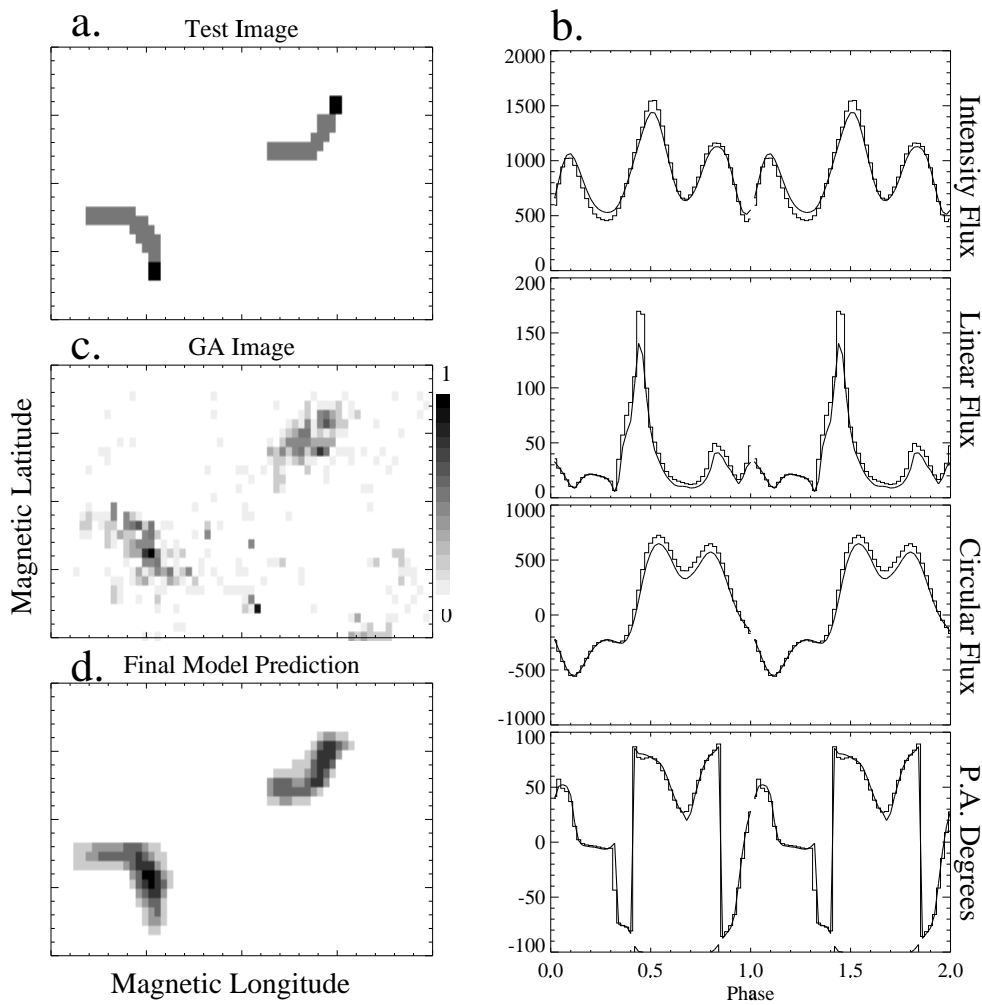
Figure 4.4: Extended sources: **a.** The emission on the surface of the white dwarf. **b.** The test emission light curves (histogram) and the model fit (solid smooth curve). **c.** GA optimised image. **d.** Final model prediction after Powell's optimisation.

Figures 4.4c and d show the optimised image solutions from the GA and the Powell's method respectively. The grey scale is as in figure 4.2. As can be seen from the figures, the GA has found the location and approximate extent of the emission regions. The Powell's method has then smoothed and clearly defined these regions and also reduced the number of low level random emission sites.

4.3.3   Noisy data sets

Real data sets will always have noise to some degree superimposed on the signal. Therefore, in figures 4.5 and 4.6 I demonstrate how the optimisation technique handles noisy data sets. Figure 4.5 and 4.6 use the data set shown in figure 4.4 but have different amounts of artificial noise added.

Figure 4.5b shows the extended source data set from figure 4.4 with artificial noise added. Noise was introduced to each of the four Stokes parameters by using a Gaussian random number generator giving signal–to–noise ratios of 48,3.5,2.7 and 8.6 for the I, Q, U and V Stokes parameters respectively. This gives an average signal–to–noise ratio of ~ 15.0. The error bars represent 1 sigma confidence levels. In comparison to figure 4.4, the model fit to the polarized light curves is approximately the same. Upon closer inspection the sharpness of the linear polarization peaks are beginning to decrease, particularly the main peak at phase ~ 0.45. Also the map predicted by the model (figure 4.5c) is starting to show loss of spatial resolution with the sharpness of the arcs no longer so well defined; however their spatial extent and location on the white dwarf remains fairly well determined.
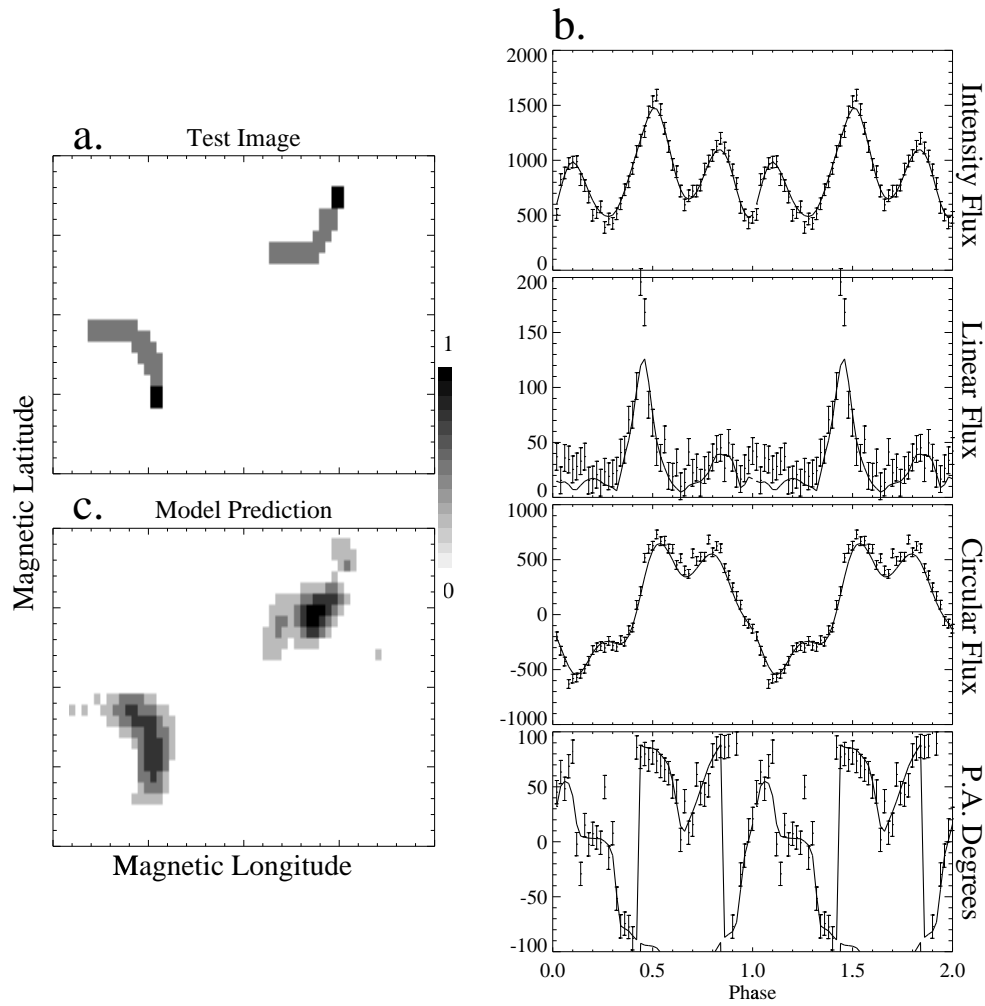
Figure 4.5: As for figure 4.2 but with artificial noise added giving an average signal-to-noise ratio of ~ 15.
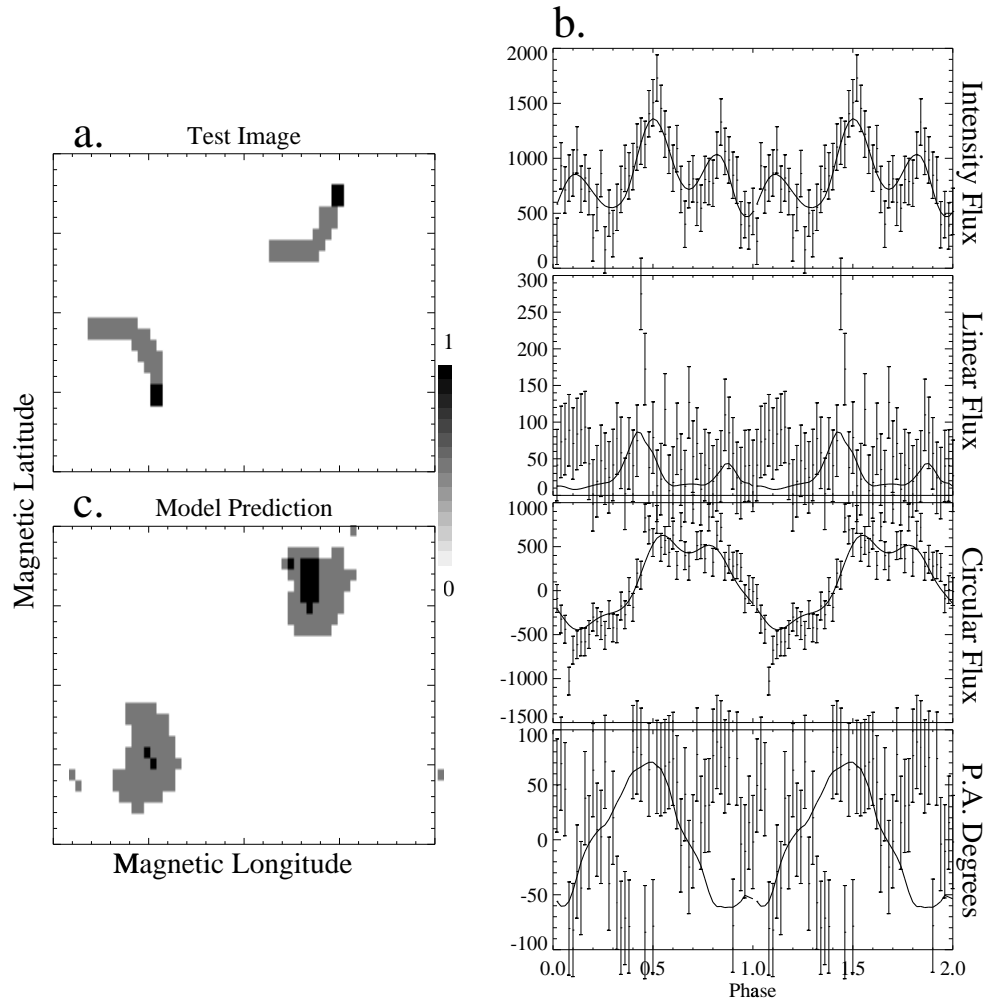
Figure 4.6: As for figure 4.2 but with artificial noise added giving an average signal–to–noise ratio of ~ 4.

Figure 4.6 demonstrates the effect of decreasing the average signal–to–noise ratio even further to ~ 4 corresponding to signal–to–noise ratios of 12.9,0.94,0.74 and 2.3 for the I, Q, U and V Stokes parameters respectively. The prediction for the intensity light curve is still acceptable. The same is also true for the circular polarization but to a lesser extent: the dip feature at phase ~ 0.65 and the peak at phase ~ 0.1 are beginning to be lost in the noise. However, because of the lower number of counts, the noise contribution to the linearly polarized light curve has a significant effect. There is no longer any detailed structure in the light curve and even the strong peak at phase ~ 0.45 is no longer significantly influencing the model fit. The position angle of linear polarization is almost completely lost in the noise and the model fit is significantly different from the infinite signal–to–noise data in figure 4.4.

The results of the model prediction are shown in figure 4.6c. Immediately obvious is the poor prediction for the shape and extension of the emission regions. They have become more extended and amorphous. However, they are still correctly located.

In general, for most MCVs, the linear polarization and its position angle will be the most inflicted with noise. This is true because the amount of linearly polarized flux is generally less than the intensity and circularly polarized fluxes and the intensity and circularly polarized light curves therefore have better signal–to–noise ratios. On their own, the intensity and circularly polarized light curves will put upper limits on the size of the emission regions only and can predict the number and location of the emission regions. The linear polarimetry and position angle determines the shapes of the emission regions more precisely. This is particularly

true because of the sharp peak features produced by most MCVs in their linearly polarized light curves.

4.4 Multiwavelength optimisation

Cyclotron radiation is both wavelength and viewing angle dependent. To place more constraints on the optimisation technique one can therefore use multiwavelength intensity, circular and linear polarization observations. In this section I demonstrate the optimisation technique on multiwavelength data using multiwavelength test cases.

I have used the same system parameters as the previous section, namely an inclination of $80°$, magnetic dipole offset of $10°$, magnetic polar field strengths of 60 MG and polar optical depth parameter Λ of 1.0×10^5. I have used infinite signal–to–noise in this section in order to elucidate the capability of multiwavelength optimisation.

4.4.1 The test case

Figure 4.7a and b (histogram curves) show the R(6500–8400Å) and B-band(3400–5300Å) polarized emission respectively, arising from the two test emission regions used in the above section (4.3.2). The B-band data was also optimised in the previous section.

The light curves clearly show wavelength dependence. Firstly, the general morphology of the intensity curves changes from blue to red with maximum flux occurring almost half a phase earlier in the red data. Most dramatic are the differences in the linearly polarized flux light curves. The linear pulse at phase ~ 0.45 in the R-band has almost vanished and
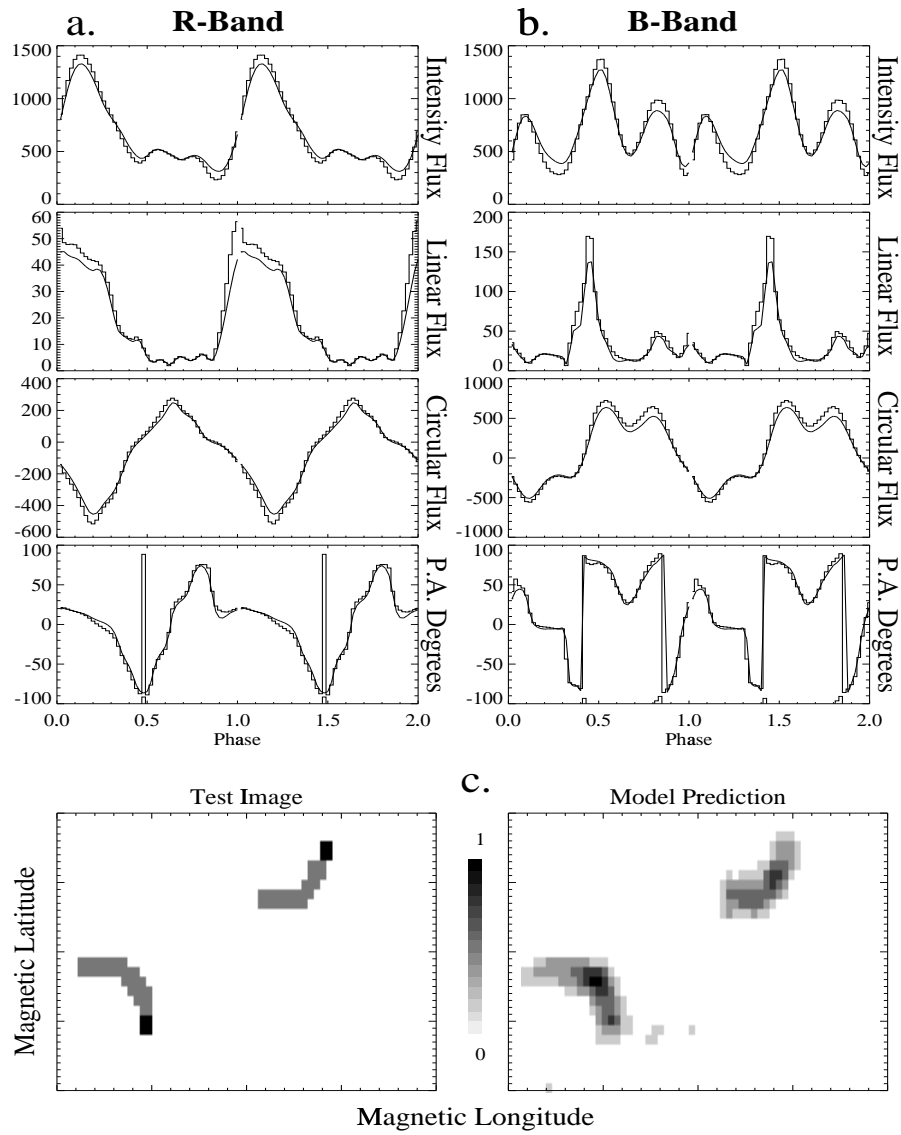
Figure 4.7: Extended sources: Correct magnetic field estimate.

therefore the pulses at phase ~ 0.0 dominate the morphology of the linearly polarized curve. The amount of circularly polarized flux is less in the R-band and the dips at the phase of the polarized flux peaks have disappeared. Also the position angle curves are different because of the different amounts of wavelength dependent linearly polarized flux emanating from different parts of the emission regions.

4.4.2   The optimisation results

The smooth curves in figure 4.7a and b show the optimised model fits to the input test data. The model fits to both wave-bands were optimised simultaneously. Therefore the relative amount of fluxes between each wave-band is modelled correctly. As can be seen from the figure the data has been modelled accurately.

Figure 4.7c shows the predicted shape and location of the emission regions which agree with the test emission regions first depicted in figure 4.4.

4.4.3   Dependence on magnetic field strength

The above fits were obtained on the assumption that the magnetic field strength of the white dwarf in the system is known. However, for most magnetic cataclysmic variables their magnetic field strengths are not known.

Figures 4.8 and 4.9 demonstrate the effects of optimising the model fits with estimates of the magnetic field strengths being $10MG$ too low and too high respectively. In both cases the model predictions for the shape and location of the emission regions are less well defined, with sev-
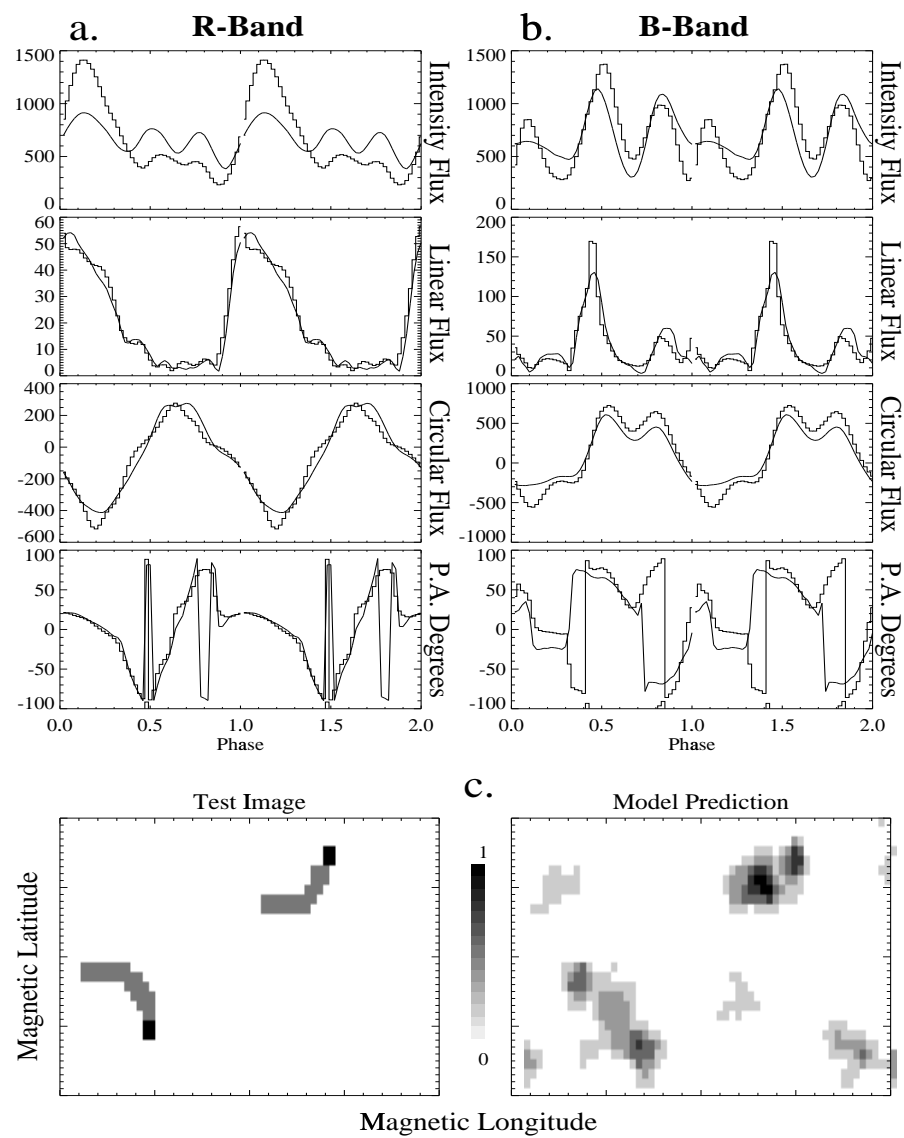
Figure 4.8: Extended sources: Magnetic field estimate too low.
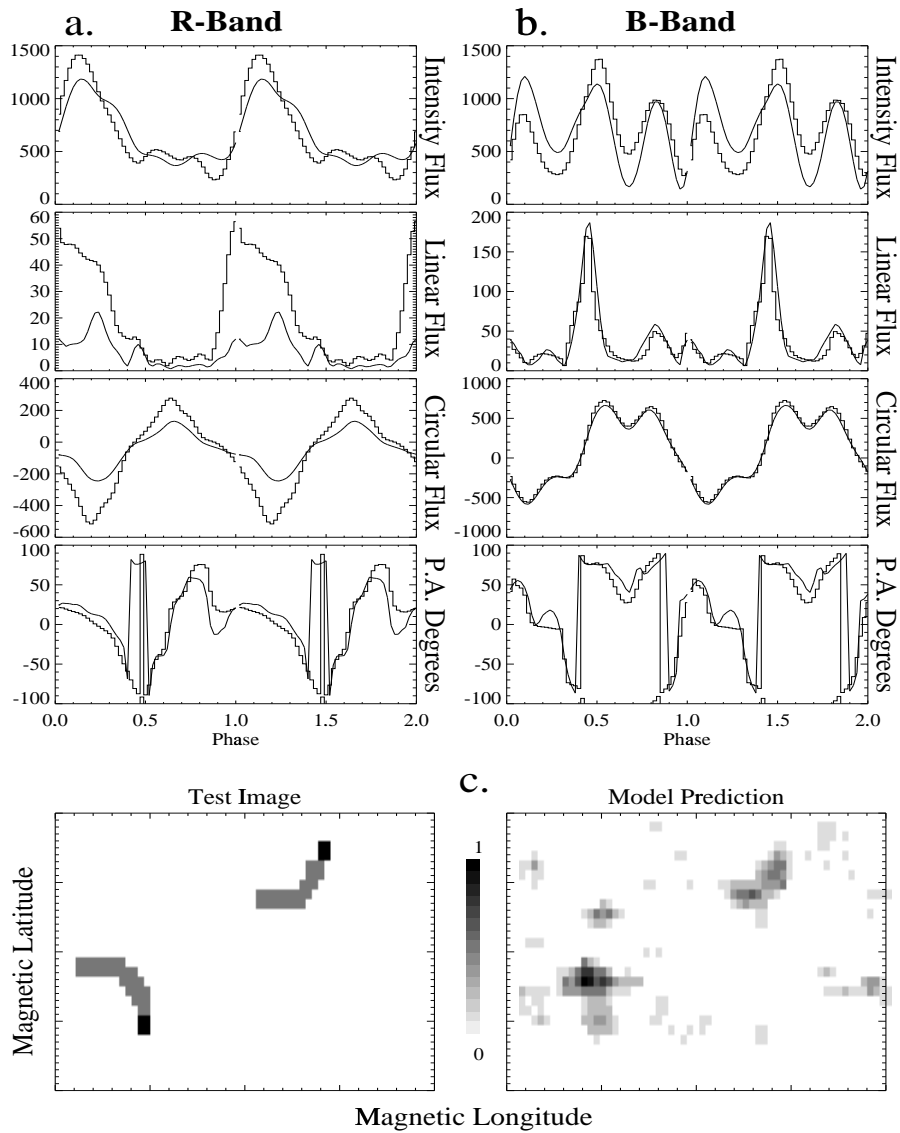
Figure 4.9: Extended sources: Magnetic field estimate too high.

eral extra emission regions appearing. From the figures it can also be seen that when the estimate for the magnetic field strength is too low the polarized model fits to the B-band data deteriorate more compared to the R-band data. The opposite is then true when the estimate for the magnetic field strength is too high.

This can be understood by looking at figure 2.10. In this figure the B and R-bands correspond to the left and right wings of the spectral curve respectively. When the magnetic field strength is too high, the spectrum moves towards the blue resulting in almost zero flux in the R-band. The opposite is then true when the magnetic field strength is set too high.

4.5   Summary

In this chapter I have developed a technique, using a combination of a genetic algorithm and Powell's method, to produce objective maps of the cyclotron emission regions in magnetic cataclysmic variables. I have applied the technique to various simulation test cases with different source shapes and different signal–to–noise ratios. From the test cases I have shown that data with an average signal–to–noise ratio of ~ 15 it is possible to determine the approximate shape of the emission regions and their location on the surface of the white dwarf fairly accurately. Even without good linear polarization data I have shown that it is possible to locate the emission sites and put upper limits on their size.

With better signal–to–noise ratio data and data with higher phase resolution it is possible to obtain very detailed maps of the cyclotron emission regions. For example, with 50 phase bins per rotational cycle of the

white dwarf, one phase bin will correspond to just over 7 degrees of rotation by the white dwarf.

To increase the spatial resolution of the optimised maps further it is necessary to obtain more phase bins per rotational cycle of the white dwarf.

I have also shown that by incorporating multi-band data it is possible to map the emission regions with greater accuracy. This is possible because of two reasons. Firstly, there are more data points to fit which will therefore constrain the total number of possible solutions. Secondly, the shape of the emission regions are strongly wavelength dependent: solutions that are good for one wave-band may not necessarily give a good solution for another wave-band.

Having obtained maps of the accretion region and by assuming a dipole field, it is then possible to back trace the magnetic field lines that feed the emission region to the orbital plane and hence locate approximately the threading regions where the material attaches to the magnetic field lines. Doppler mapping of the emission lines can be added to obtain the velocity structure of the accretion flow and to relate this to the results obtained from the Stokes imaging.

Chapter 5

The accretion region of the AM Her system ST LMi

5.1 Introduction

In this chapter I apply the optimisation technique, described and developed in the previous chapter, to the AM Her system ST LMi. I have chosen this system because of its 'simple' one–pole accretion mode and its relatively high levels of polarization. Also, several authors (Wickramasinghe & Meggitt 1985, Ferrario & Wickramasinghe 1990 and Cropper & Horne 1994) have previously modelled the polarized emission (intensity only in the case of Cropper & Horne 1994) from ST LMi thus allowing comparisons to be made with the maps produced using the 'Stokes Imaging' technique.

5.2   The AM Her system ST Leo Minoris

ST LMi was discovered as a strong emission line object during the Case Western objective prism survey and identified by Shore et al. (1982) as a cataclysmic variable. Soon after, Stockman et al. (1983) discovered variable linear and circular polarization and thus showed it to be an AM Her star. The light curves repeated on a $\sim$ 114 minute orbital period with a bright intensity, linear and circular polarization phase lasting $\sim$ 40 minutes, similar to VV Pup (Cropper & Warner 1986). Radial velocities of 350–1400 kms^{-1} in Hβ, Hγ and Hδ were identified by Stockman et al. (1983) with maximum positive velocity occurring at approximately the center of the bright phase. From the rate of change of the position angle Stockman et al. (1983) derived inclination and magnetic dipole offset angles of $i = 69°$ and $\beta = 56°$ respectively. They found that there was no undershoot in the sign of the circular polarization, as seen in VV Pup, suggesting that the cyclotron emission column is not tall and quite extended.

Schmidt et al. (1983) obtained spectropolarimetry and spectrophotometry which revealed Zeeman-split Balmer polarization and absorption features during the faint phase of ST LMi. This corresponds to a flux–weighted mean photospheric magnetic field strength of $B = (19 \pm 2) \times 10^6$ gauss. They estimated the polar magnetic field strength to be $B_p = (30 \pm 5) \times 10^6$ gauss. They also tentatively identify a possible Zeeman absorption feature (H$\alpha\sigma^-$) during the bright phase implying a magnetic field of 13 MG at the cyclotron emission region.

An optical and near–infrared study of ST LMi was carried out by Bai-
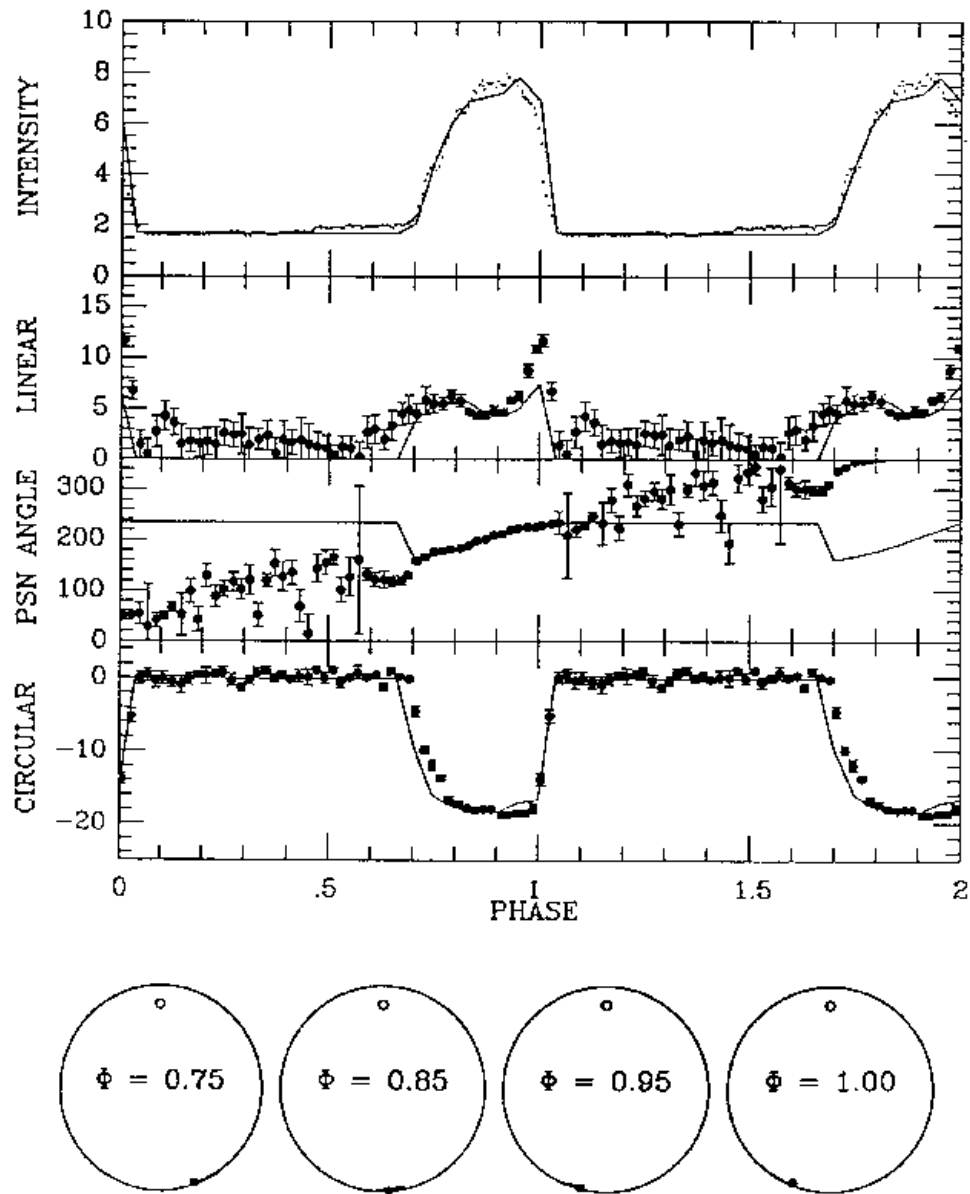
Figure 5.1: The optical white light polarimetric observations of ST LMi (Cropper 1986b) with model light curves from Ferrario & Wickramasinghe (1990). The lower globes represent the white dwarf and the accretion region as viewed from Earth. See figure 5.5b for a clearer view of the location and size of the accretion region.

ley et al. (1985). The faint phase infrared radiation is dominated by an M–dwarf secondary whose ellipsoidal variations place it closest to the observer at phase ~ 0.95, the final part of the bright phase. They also derived a magnetic field strength of 18 MG from Zeeman features for the inactive pole in agreement with Schmidt et al. (1983). The observed emission line profiles have two components, one thought to originate from the stream of infalling material onto the white dwarf and the second from near the secondary. The flux distribution from the total and polarized components during the bright phase showed that the cyclotron radiation is optically thick at wavelengths above about $1\mu m$ and optically thin at shorter wavelengths. From their derivations for the white dwarf mass, distance and size of the accretion region they estimated the temperature of the cyclotron region to be between 10–50 keV.

Wickramasinghe & Meggitt (1985) used the theoretical cyclotron calculations of Wickramasinghe & Meggitt (1985,WM85) in their analysis of the flux and circular polarization observations of ST LMi by Bailey et al. (1985). They estimated the temperature of the polarized emission region to be in the range 15–30 keV. Also, with a magnetic field strength of between 10 MG and 19MG for the cyclotron emission region they estimated values for the optical depth parameter to be between $\Lambda \sim 10^5$ and $\Lambda \sim 10^6$.

Cropper (1986b) presented white–light simultaneous photometry, linear and circular polarimetry of ST LMi (figure 5.1). These relatively high signal–to–noise observations clearly show standstills in the gradual rise to maximum brightness with a more rapid decline at the end of the bright phase. The hard X–ray light curve published in Beuermann et al (1984)

has the same bright–phase duration as the optical intensity and circular polarization curves, lasting about 0.35 of the orbital period. The stand-stills have been seen at different epochs suggesting that they are long term features, prompting Cropper (1986b) to suggest two cyclotron emission regions located close together as an explanation for the standstills. The soft X–ray light curve and the linear polarization light curve how-ever, have a longer bright phase lasting about 0.45 of an orbital period. The linear polarization increases gradually at the beginning of the bright phase and decreases rapidly from its maximum at the end of the bright phase where it appears to be depolarized between phases 0.04–0.07. The position angle increases through $180°$ during one orbit and appears to drop at both ends of the bright phase. Cropper (1986b) describes three possi-ble mechanisms for linear polarization during the faint phase as being either electron scattering or cyclotron radiation from further up the col-umn or cyclotron emission from a second accretion region located near or at the other magnetic pole. Other parameters calculated by Cropper (1986b) are: a magnetic field strength of 18 MG at the cyclotron emission region using the ratio of the circular to linear polarization; from the size and height of the emission region, an inclination of $i = 56 \pm 4°$ and dipole offset angle of $\beta = 134 \pm 4°$ or $46°$ using the coordinate system of Stock-man at al (1983); primary mass of $0.54 \pm 0.2 M_\odot$; luminosity of $\sim 5 \times 10^{32}$ erg s^{-1}; mass transfer rate of $\sim 10^{-10} M_\odot y^{-1}$.

Ferrario & Wickramasinghe (1990) discussed the properties of cyclotron radiation originating from homogeneous (constant optical depth) arc–shaped emission regions, taking into account the effects of field spread across the shock, and applied their model to interpret observations of three AM Her

systems including ST LMi. The model fit is shown as the solid line to the data of Cropper (1986b) in figure 5.1. Their best fit model used an inclination of $i = 55°$ and a magnetic dipole offset angle of $\beta = 150°$. The emission is that at harmonic $n = 8$ with $T_e = 10$keV, $N_e = 1.0 \times 10^{16} cm^{-3}$ and $\Lambda_s = 1.5 \times 10^4$ in the radial direction. They used a magnetic field offset along the dipole axis by $0.1 R_{WD}$ with a polar strength of $B_p =$40 MG. The shape and location of their emission arc is shown at the bottom of figure 5.1 and reproduced in figure 5.5b as the solid curve. It is extended in magnetic latitude by $2°$ between $9°$ and $11°$ with an elongation towards the magnetic equator of $\delta\theta^* = 10°$. It is also extended in magnetic longitude between $130°$ and $200°$. They explained the mismatch between the observed duration of linear polarization and that of their calculations as possibly being caused by a low–density leading edge of the emitting arc.

Peacock et al. (1992) obtained simultaneous multi-band photometric and polarimetric light curves for ST LMi in the visible range and the near infrared. The H and J band observations clearly show the presence of a second accretion region near the second magnetic pole of the white dwarf. Positive circular polarization during the faint phase was detected between 10 and 15 percent. Using the rate of change of position angle they calculate an inclination of $i = 66°$ and a magnetic dipole offset of $\beta = 147°$ for the main cyclotron emission region.

Ferrario et al (1993) presented near–infrared spectroscopic observations of ST LMi in which broad and resolvable cyclotron emission harmonics were seen during the bright phase. The observed position of the harmonics yielded a magnetic field strength of ~ 12 MG. However, the position of the harmonics depends on the electron temperature T_e, the opti-

cal depth Λ, the viewing angle and on the extent of the cyclotron emission region. Therefore, in order to fit the data they used the models and notation of Ferrario & Wickramasinghe (1990) to obtain a best fit model with a polar magnetic field at the weaker pole of 11.5 ± 0.5MG, when $\Lambda = 10^5$ and $T_e = 10$keV. They also found that a better fit is obtained by introducing a change in the opacity along the arc: a high–temperature, high–density region with $T_e = 12$keV and $\Lambda = 4.2 \times 10^7$ extending from $\psi = 130°$ to $\psi = 170°$ and a second, lower density, region with $T_e = 5$keV and $\Lambda = 2.6 \times 10^4$ extending from $\psi = 170°$ to $\psi = 250°$. The spectroscopic observations and the results of their model are shown in figure 5.4.

As briefly mentioned in chapter 4, Cropper & Horne (1994) used the maximum entropy method to map the spatial extent of the X–ray and optical emission in ST LMi. Their map of the optical emission region is shown in figure 5.5c. Their maps indicate that the cyclotron radiation was being emitted from two closely connected regions extended in a south west–north east orientation at the time of the optical observations.

5.3   System parameters

As discussed in chapter 4 some parameters of the system under consideration are kept constant during an optimisation run. These include the inclination, magnetic dipole offset angles (latitude and azimuth), temperature at the shock and the magnetic field strength at the poles. Many optimisations are then run to cover this the system parameter space.

Section 5.2 indicates that most of these parameters have been estimated with different degrees of confidence:

1) The extension of the Ferrario et al (1993) data into the IR together with the more sophisticated models available to them probably make their magnetic field determination the most reliable. I therefore adopted 12 MG for the magnetic field.

2) The inclination of ST LMi has been estimated to range from $56°$ to $69°$.

3) The magnetic dipole offset angle (latitude) has been estimated to range from $33°$ to $56°$.

4) The magnetic dipole field offset in azimuth: Stockman et al. (1983) found the maximum positive radial velocity of the Balmer lines to occur at approximately the center of the bright phase and Bailey et al. (1985) estimated the secondary to be closest to the observer during the end part of the bright phase. The radial velocity of the Balmer lines is maximum when the magnetic field lines feeding the accretion region cross our line of sight. Also, from the discussion in chapter 2, the morphology of the linear polarisation curves implies that the emission region is ahead of the magnetic pole in phase. Therefore the phase at which the dipole field crosses our line of sight must be later than the phase at which maximum positive radial velocity occurs and before approximately the end of the bright phase.

5) Wickramasinghe & Meggitt (1985) estimated a shock temperature in the range of 15–30 keV and Bailey et al. (1985) in the range 10–50 keV. However, in order to reproduce the cyclotron harmonics in the infrared spectra of ST LMi the lower temperatures in this range are required. For the shock temperature I have chosen to use the 10 keV constant temperature calculations of MW85.

6) The optical depth parameter was also estimated by Wickramasinghe

& Meggitt (1985) to be between $\Lambda \sim 10^5$ and $\Lambda \sim 10^6$. This parameter is included in the optimisation technique and is allowed to vary in the range $\Lambda \sim 10^5 - \Lambda \sim 10^7$

5.4 Optimised model fit

Figure 5.2 shows the optimised model fit, using the 'Stokes imaging' technique described in chapter 4, to the polarimetric white light observations of Cropper (1986b). The fit was obtained using an inclination of $61°$ and a magnetic dipole offset angle of $48°$. Outside a range of $\pm 5°$ the fits become significantly poorer with the prediction for the linear polarization and the variation in position angle deteriorating most.

The 'Stokes imaging' technique has reproduced the gradual rise and rapid decline of the bright phase emission between phases $\phi \sim 0.7$–0.05 and similarly for the circularly polarized flux.

The peak in the linear flux has been reproduced at phase $\phi \sim 0.0$ and the overall shape is in close agreement. The variation in position angle of the model is also in close agreement with the observed variation in position angle during the bright phase. Also, the relative amounts of linear and circular fluxes has been correctly modelled.

The model does not correctly predict the gradual rise in intensity between phases $\phi \sim 0.45$ and $\phi \sim 0.7$. The technique can be 'forced' to fit the data more accurately by lowering the value of the Lagrangian multiplier during the line minimisation part of the optimisation. However, this precursor to the bright phase is possibly due to emission from a second emission region located at or near the other magnetic pole. This second emis-
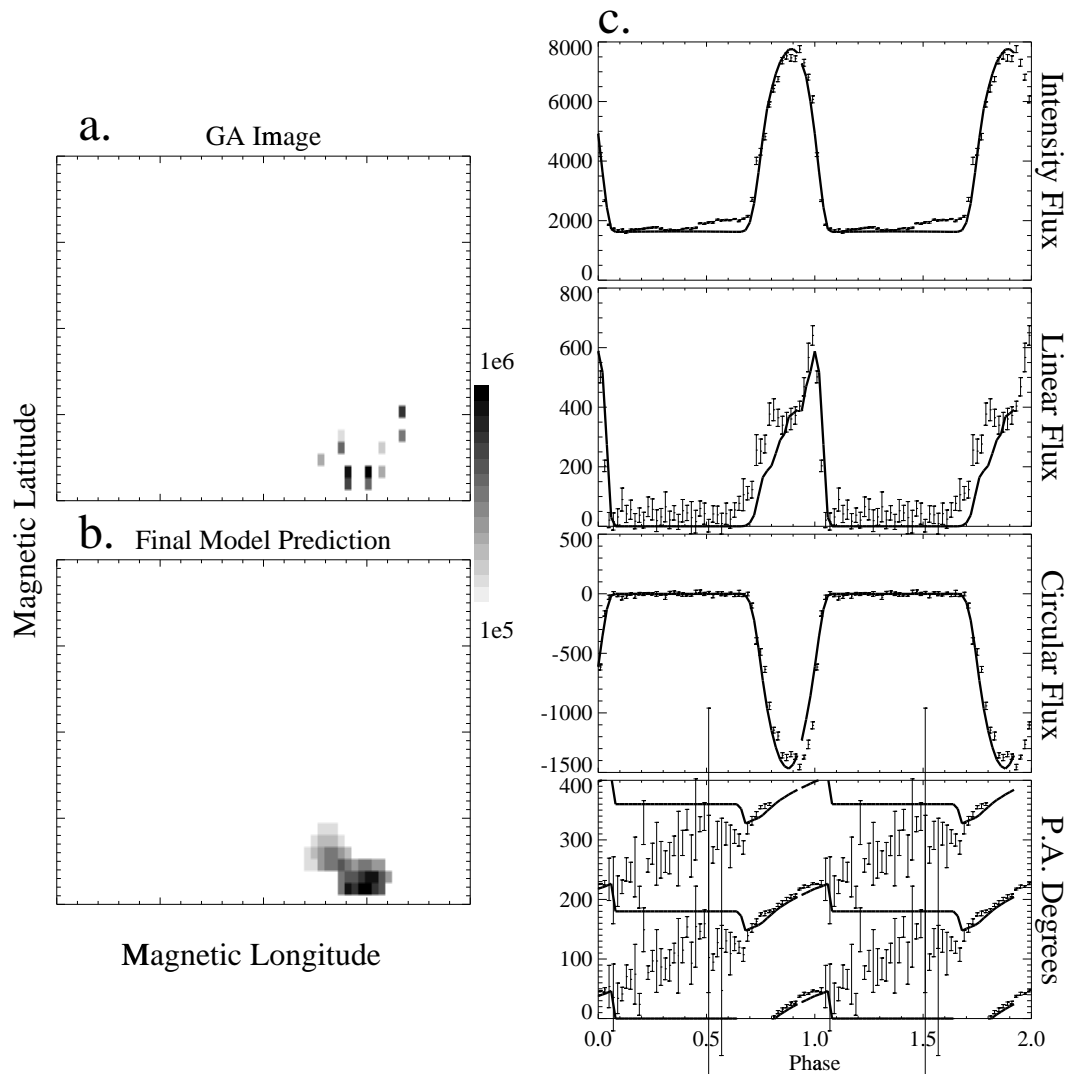
Figure 5.2: Optimised model solution: **a**. The emission on the surface of the white dwarf after genetic optimisation. **b**. Final optimised image after line minimisation. **c**. The model fit (smooth curves) to the polarimetric observations of Cropper (1990).
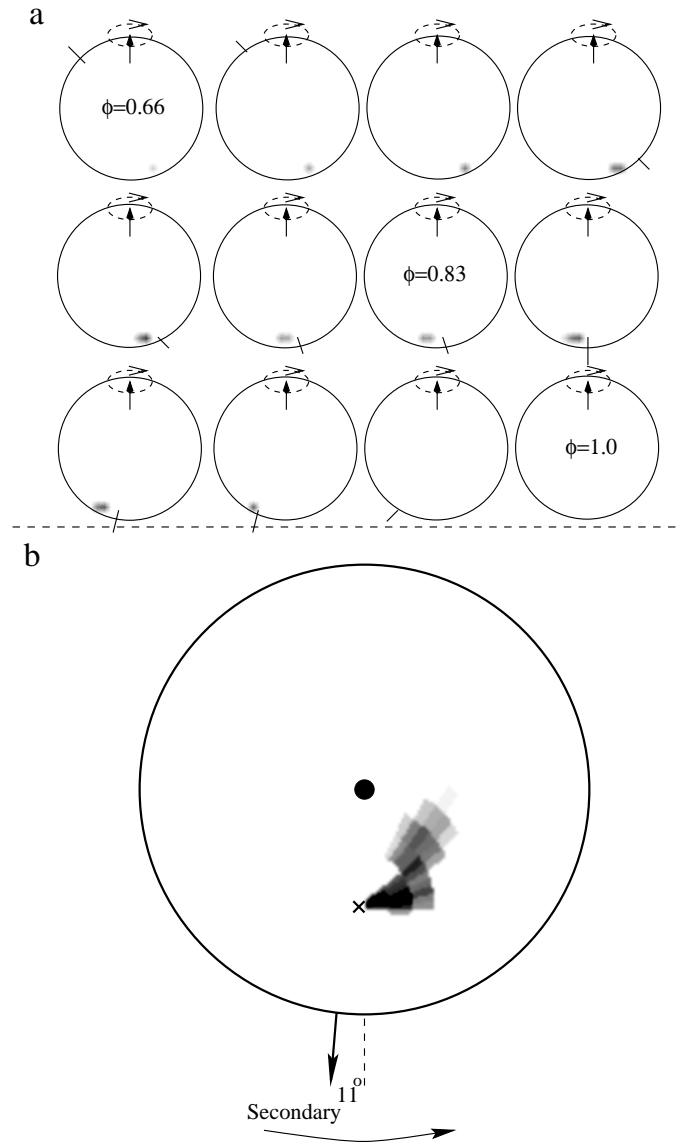
Figure 5.3: **a**. The white dwarf with emission region as seen from Earth during the bright phase. **b**. The emission region in more detail viewed from directly above the spin axis (dot) of the white dwarf in the hemisphere containing the emission region. The horizontal arrow points the direction in which the secondary orbits the white dwarf. The cross marks the magnetic pole.

sion region may also be responsible for the excess linear polarisation at the beginning of the bright phase and the variation in position angle during the faint phase. Observations by Peacock et al. (1992) suggests that this region is mainly radiating cyclotron emission in the IR and therefore does not make a significant contribution to the white light polarimetry. To be able to model the cyclotron emission from the second emission region requires better signal–to-noise polarimetry than that obtained by Peacock et al. (1992). In particular, circular polarization is required to locate the hemisphere in which the secondary emission region in located.

The 'Stokes imaging' technique has predicted a single emission region located near the magnetic pole in the lower hemisphere of the white dwarf in ST LMi (figure 5.2b). The emission region appears to consist of two distinct regions joined together. The optical depth parameter Λ is a function of density and hence the image prediction gives a map of the local relative density of the cyclotron emitting region. The leading smaller region is of lower density than the trailing larger higher density region. The larger region is centered at a magnetic longitude of $\psi \sim 90°$ and extends in longitude by $\sim 18°$ on either side. In latitude it extends from $\theta \sim 6°$ to $\theta \sim 25°$ while the optical depth parameter Λ decreases from $\sim 10^6$ to $\sim 5 \times 10^5$. The smaller less dense region is centered at a magnetic longitude of $\psi \sim 125°$, $\sim 35°$ ahead of the larger region and extends in longitude by $\sim 15°$ on either side. In latitude it extends from $\theta \sim 20°$ to $\theta \sim 45°$ while the optical depth parameter Λ decreases from $\sim 5 \times 10^5$ to $\sim 10^5$.

Figure 5.3a shows the emission region mapped onto a sphere representing the surface of the white dwarf as viewed from Earth during the bright phase. The magnetic axis (shown as diagonal lines) is offset from

the spin axis by $48°$ which itself is inclined to the viewer by $61°$. The emission region appears during phases $\psi \sim 0.65$–1.0 only. At the beginning of the bright phase the lower density region appears over the limb of the white dwarf first and towards the end of the bright phase the higher density region disappears over the limb of the white dwarf last. Figure 5.3b shows the emission in more detail. This time the viewing angle is from directly above the spin axis of the white dwarf in the hemisphere containing the emission region.

5.5 Cyclotron spectrum

The cyclotron emission is optically thin towards the higher harmonics for the magnetic field strengths of interest here (Bailey et al. 1985). At lower harmonics, as pointed out by Lamb & Masters (1979), the cyclotron emission is greater than the Raleigh–Jeans tail of the blackbody emission. Therefore at lower harmonics the cyclotron emission is optically thick with the excess flux absorbed (see chapter 2). The wavelength of maximum cyclotron flux and the general morphology of the cyclotron spectrum not only depends on the shape of the emission region but also on the physical conditions of the accretion shock such as its temperature and density. The spacing of the cyclotron harmonics in the spectrum also provides a direct measurement of the magnetic field in the accretion region.

Figures 5.4a–d show the bright phase infrared spectrum of ST LMi from Ferrario et al (1993). The thin solid line is their model fit from an arc shaped emission region whose dimensions are given above. They identified the features at phases 1.42, 1.65 and $2.00\mu m$ as cyclotron humps
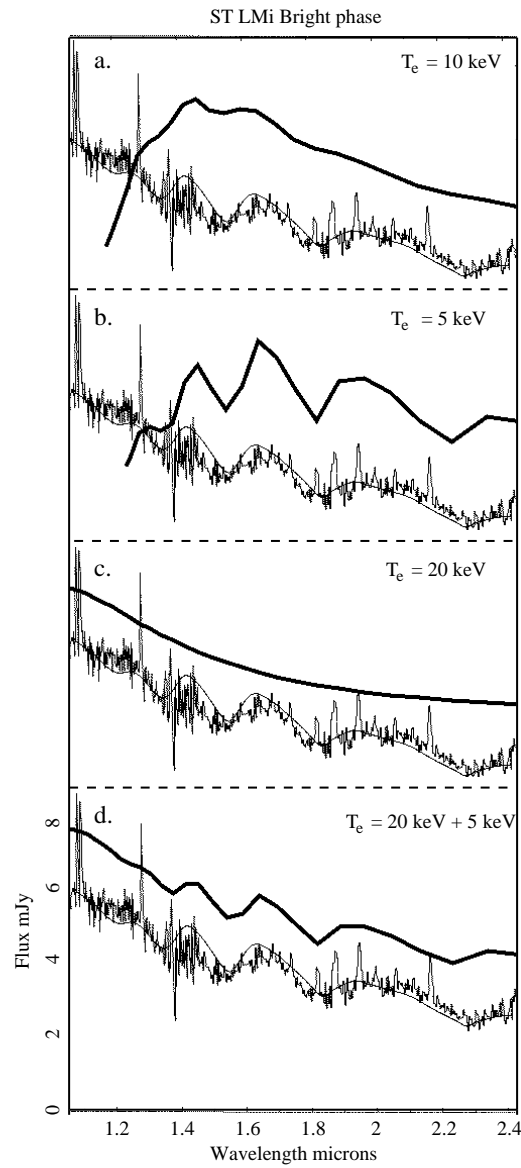
Figure 5.4: **a–d** The bright phase spectrum of ST LMi and model fit (thin line) from Ferrario et al (1993). The thick curves are the spectra (vertically displaced for clarity) produced by the optimised emission region during the bright phase, using the shock temperatures shown,

with harmonic numbers 6,5 and 4 respectively corresponding to a magnetic field of 11.5 ± 0.5 MG. Also, from optical and IR observations, Bailey et al. (1985) showed that maximum cyclotron flux occurs at $\sim 1\mu m$ and thus the cyclotron emission to be optically thick above $\sim 1\mu m$.

The vertically displaced thicker curve in figure 5.4a is the predicted cyclotron spectrum of the optimised model during the bright phase. The model spectrum can be moved arbitrarily in the vertical direction to fit the data. Its spectral slope is in good agreement with the observations above $\sim 1.4\mu m$ and the position of the cyclotron humps match well. However, the model spectrum peaks at a longer wavelength than the observations suggest making the fit at shorter wavelengths than $\sim 1.4\mu m$ very poor. Also, the general morphology of the observed cyclotron humps is not repeated by the model, in particular their amplitude.

Figure 5.4b shows the predicted cyclotron spectrum using the same optimised solution as above but with a lower shock temperature. By lowering the shock temperature the amount of excess cyclotron emission that is absorbed by the Raleigh–Jeans tail of the blackbody emission is reduced. As a result, the amplitude of the cyclotron harmonics is greater and their general morphology match the observations more closely. However, the wavelength at which the maximum predicted cyclotron flux occurs is even further longward than the $T_e = 10$keV prediction.

Therefore in figure 5.4c I show the predicted cyclotron spectrum from the same optimised region but with a shock temperature of $T_e = 20$keV (the shock temperature calculations are from Wu, private communication). The spectral slope now agrees with the observed IR spectrum. However, the amount of excess cyclotron emission that is absorbed by the Raleigh–

Jeans tail of the blackbody emission has increased resulting in the loss of cyclotron hump structure.

As first suggested by Ferrario et al (1993) these results indicate that a single temperature model is insufficient in reproducing the cyclotron spectrum in ST LMi. A lower temperature and possibly a lower density region is required to reproduce the cyclotron humps in the optically thick part of the spectrum and a higher temperature and density region to reproduce the correct spectral slope. In figure 5.4d I show the predicted combined cyclotron spectrum of the $T_e = 5$keV and the $T_e = 20$keV models. This combined spectrum is a significant improvement over the single temperature model in that the spectral slope and the general morphology of the cyclotron humps are reproduced.

5.6   Discussion

5.6.1   The accretion region

In figure 5.5 I compare the prediction for the shape and location of the cyclotron emission region with that of previous work. Figure 5.5b shows the prediction for the shape and location of the cyclotron emission region from Ferrario et al (1993) mapped onto the same coordinate system used throuout this thesis and defined in chapter 2. The arc is an extension of that used by Ferrario & Wickramasinghe (1990) whose white light model curves are shown in figure 5.1. Ferrario et al (1993) added a lower density and temperature emission region to the leading edge of the arc (shown as a dashed curve) in order to reproduce the cyclotron features seen in the infrared spectrum of ST LMi. In this respect figures 5.5a and 5.5b
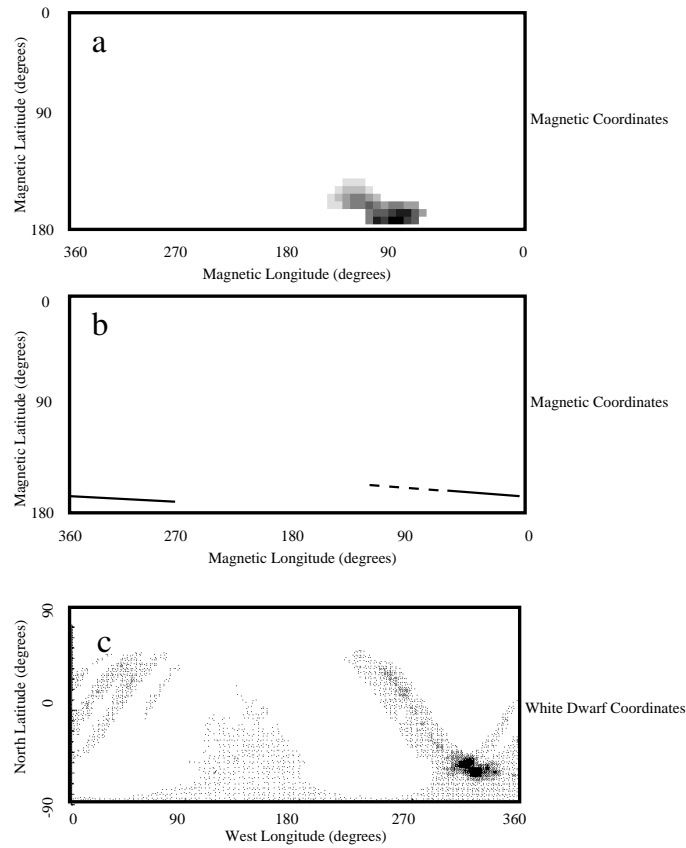
Figure 5.5: **a.** The optimised emission region. Grey scale is a measure of optical depth (see figure 5.2). **b.** The accretion region from Ferrario et al. (1993) mapped onto the same coordinate system used in this thesis. The dashed curve has a lower temperature and optical depth parameter than the trailing solid curve. **c.** The optimised intensity map from Cropper & Horne (1994). The figure is not on the same coordinate system used in this thesis. Specifically it is on white dwarf spin coordinates.

agree and also in the approximate location of the leading edge of the arc further in magnetic latitude from the magnetic pole with the higher density region closer to the magnetic pole. However, the shape of the emission region used by Ferrario et al (1993) is as much as three times more extended in magnetic longitude and only $2°$ wide in latitude. Additional complications arise because different values were used for the inclination and magnetic dipole offset angle.

Figure 5.5c shows the intensity map from Cropper & Horne (1994) which they obtained using a maximum entropy technique. They applied the same technique to the X–ray light curves from ST LMi and found the X–ray map to be closely coincident with the optical map. The map cannot be directly compared to figures 5.5a and 5.5b because the coordinate systems used are different: Cropper & Horne's map is plotted on the white dwarf's spin latitude and longitude coordinates which contains no magnetic field orientation geometry. However, the approximate size and shape of the emission region can be compared. For example, both images (figures 5.5a and 5.5c) have the emission region divided into two closely adjoining regions. In each case the region is ahead of the line of centers of the two stars and elongated in the same direction. Moreover, they are approximately the same in size, although a more accurate comparison is difficult because of the differing coordinate systems. Finally, the two images differ the most in that Cropper & Horne's image maps the surface brightness and the Stokes image maps the optical depth parameter. For this reason and because of the viewing angle dependence of polarized cyclotron emission, if the Stokes image were to be mapped in terms of surface brightness, a separate plot would have to be made for the intensity,

circular and linear polarisation distributions for every rotational phase of the white dwarf. This can be easily demonstrated only using an animation.

5.6.2   The cyclotron emission

The predicted cyclotron spectrum from the model fit was shown in figure 5.4a. As discussed in section 5.5 it was found that a constant temperature model of $T_e = 10$keV is inadequate in reproducing the cyclotron spectrum of ST LMi. Moreover, a better fit was obtained by using a combination of the $T_e = 5$keV and $T_e = 20$keV temperature models (figure 5.4d).

It is impossible to map the temperature structure within the accretion region from one IR spectrum alone, although intuitively, as suggested by Ferrario et al. (1993), one would expect the lower density region to have a lower temperature than the higher density region. This picture could be confirmed with phase resolved cyclotron spectra during the bright phase of ST LMi. The spectral slope and structure of the cyclotron humps in the spectrum would be expected to change as different parts of the accretion region appear and disappear over the limb of the white dwarf. At the beginning of the bright phase the low density and temperature emission region only is in view. The spectrum may then look like that of the model fit given in figure 5.4b with the cyclotron humps most pronounced. Then, during the middle of the bright phase when all the accretion region is in view, the spectrum is probably not too dissimilar to that observed by Ferrario et al. (1993). Towards the end of the bright phase, the lower temperature and density region has disappeared over the limb of the white dwarf leaving the higher temperature and density region only in view.
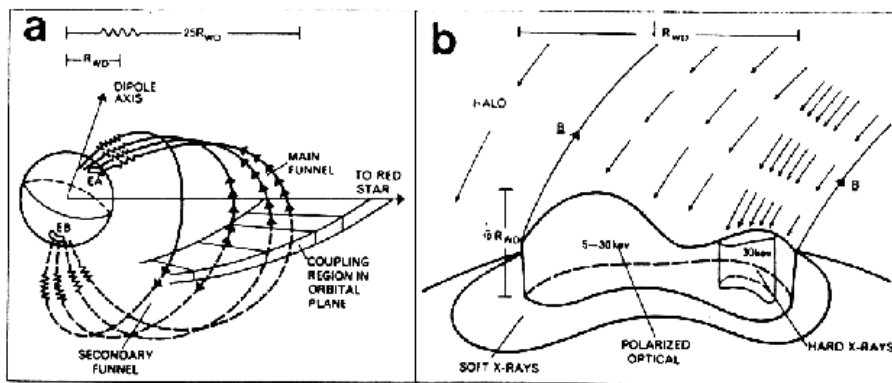
Figure 5.6: From Warner (1995), adopted from Wickramasinghe (1988). Schematic views of **(a)** the threading region showing the two accretion funnels and **(b)** the structure of the accretion zone showing a high density compact region emitting hard X–rays and an extended lower density region emitting polarized optical and IR radiation. .

The spectrum would then take the form of that given by the model spectrum in figure 5.4c which no longer has any pronounced cyclotron humps. In summary, it is the leading low density region further from the magnetic pole that emits the cyclotron harmonics in the infrared and the trailing higher density region that gives rise to most of the polarized optical emission.

5.6.3 The threading region

The structure of the accretion region in Polars depends on how and where the accreting material attaches to the field lines at the threading region. Work by Liebert & Stockman (1985) and Lamb (1985) have shown that

a number of physical processes and instabilities are competing in the region making a theoretical study difficult (see the introduction chapter for more references and an overview). However, the map produced for the emission region of ST LMi can give some indication of where and how material threads on to the magnetic field lines in ST LMi.

In figure 5.3b I showed the emission region mapped onto the surface of a sphere representing the surface of the white dwarf in ST LMi. The viewing angle was from directly above the rotational axis in the hemisphere containing the emission region of the white dwarf. The optimised model gave a best fit when the magnetic dipole was in the line of sight at phase $\phi \sim 0.92$. Also, Bailey et al.(1985) place the secondary star at phase $\phi \sim 0.95$, placing it $\sim 11°$ later than the dipole axis in the binary frame. The higher density cyclotron emission region is then located $\sim 101°$ further around from the line of centers of the two stars. The lower density region extends even further and also at increasingly greater magnetic latitudes from the magnetic pole.

A simple picture of the threading process can be gained by the use of the suggested schematic view of Wickramasinghe (1990) and reproduced in figure 5.6. After leaving the Inner Lagrangian point the gas accretes around the white dwarf until the magnetic pressure overcomes the ram pressure of the gas. At this point most of the gas is threaded onto the magnetic field lines forming the main flow onto the surface of the white dwarf. Some gas penetrates further in orbit around the white dwarf before it too is threaded onto magnetic field lines. The result is a higher temperature and density region trailing a lower temperature and density region.

Another consequence of this picture is that, the further the gas accretes around the white dwarf before threading, the easier it becomes for it to follow the magnetic field lines onto the opposite magnetic pole once it has been threaded. If this is the case, it would make itself evident in the infrared, because of the lower accretion rate, and appear just before the bright phase in the light curves (as observed in the intensity observations). The observations of Cropper (1986b) show the presence of position angle variations throughout the faint phase of ST LMI and as already mentioned, Peacock et al. (1992) found evidence of a second accretion region from IR polarimetric observations of ST LMi.

To test this hypothesis I have produced the polarized light curves that would be produced by a small emission region located at the opposite end of the magnetic field lines feeding the leading edge of the main accretion region (figure 5.7). The exercise here is to see what, if any, the main features that such a region would produce in the light curves and not actually to fit the observations.

I have expanded the scale in the intensity, linear and circular observations in order to observe the faint phase variations more clearly. By doing this, it is clear that there are two intensity maxima during the faint phase with a minimum centered on phase $\phi \sim 0.4$. The model prediction is the same with the minimum arising at phase $\phi \sim 0.4$ due to self absorption of the cyclotron radiation as the region is most nearly in the line of sight. A minimum has also been observed in the IR intensity observations of Peacock et al. (1992) at the same phase.

Peacock et al. (1992) also observed H–band positive circular polarization during the faint phase. Although the data is rather noisy it does

show a local minimum at phase $\phi \sim$ 0.3–0.4 in agreement with the model prediction.

The excess observed linearly polarized flux that occurs during phase $\phi \sim 0.75$ compared to the model prediction for the main emission region, is explained by the model as linear flux from the second emission region. From figure 5.7 it can be seen that the second emission region gives rise to a linear pulse centered at around phase $\phi \sim 0.7$. The model also predicts a linear pulse at phase $\phi \sim 0.15$. There is an indication in the J–band observations of Peacock et al. (1992) that there may also be a linearly polarized pulse at this phase. More importantly however, is the model prediction in the variation of position angle during the faint phase. The rate of change in position angle and its position on the Y–axis match the observations. Moreover, the dip in the position angle at the beginning of the bright phase can now be explained as being due to the secondary emission region.

5.7 Summary

In this chapter I have applied the 'Stokes imaging' technique developed and discussed in chapter 4 to the white light polarimetric observations of the AM Her star ST LMi from Cropper (1986b).

The technique has predicted a main cyclotron emission region located in the lower hemisphere of the white dwarf near its magnetic pole. The best fits to the observations were obtained for a system inclination of $i = 61°$ and magnetic dipole offset angle of $\beta = 41°$ although good fits were also obtained for $\pm 5°$ for both angles. From careful examination of previ-

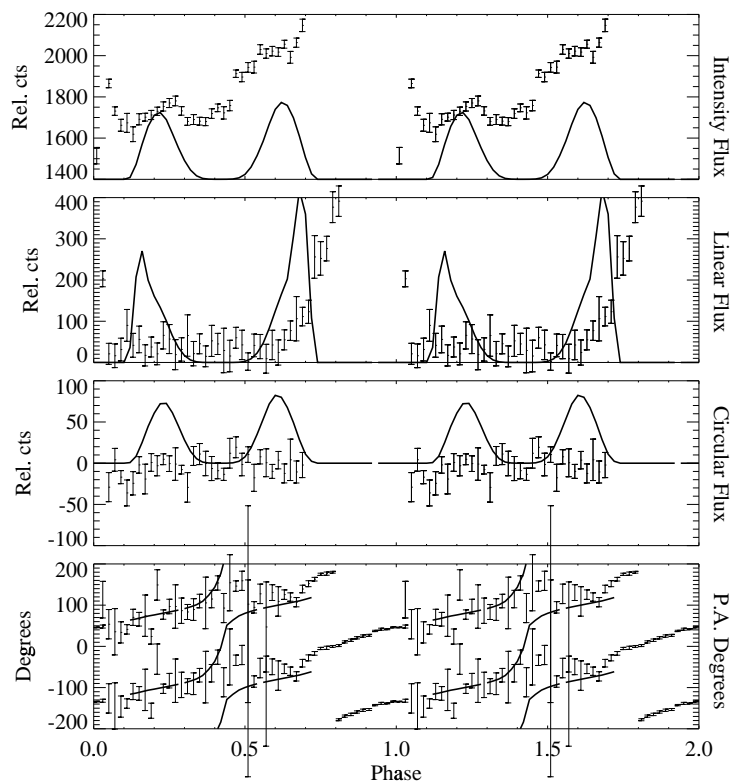Figure 5.7: The polarimetric observations of Cropper (1986b). The intensity, linear and circular axes have been expanded to reveal the faint phase variations. The smooth curve is the model prediction for emission from a second emission region located at the footprints at the opposite end of the magnetic field lines that feed the main emission region. No attempt has been made to fit the observations: see text.

ous observations I placed the dipole axis to cross the line of sight to the observer at phase $\phi = 0.92$. This is ~ 0.03 in phase ahead of the line of centers of the two stars.

I found the emission region to consist of two closely connected regions. A high density region is centered at a magnetic longitude of $\psi \sim 90°$ and extends in longitude by $\sim 18°$ on either side. In latitude it extends from $\theta \sim 6°$ to $\theta \sim 25°$ while the optical depth parameter Λ decreases from $\sim 10^6$ to $\sim 5 \times 10^5$. A less dense region leads the higher density region in orbital phase and has the parameters: $\psi \sim 125°, \Delta\psi \sim 30°, \theta \sim 32°, \Delta\theta \sim 25°$ and the optical depth parameter varies between $\Lambda \sim 5 \times 10^5 - 10^5$.

I have shown that a single temperature model is insufficient to explain the spectral slope and the general morphology of the cyclotron humps observed in the IR during the bright phase in ST LMi. A better model solution is obtained by using the combination of a low temperature, to reproduce the IR cyclotron humps, and a higher temperature, to reproduce the spectral slope and the optically thin emission in the optical wavelengths. Further time resolved spectra could confirm if the low density region has the lower temperature and the higher density region has the higher temperature.

Also, I have shown that the secondary emission region would be responsible for the positive circular polarization in the IR, the position angle variation during the faint phase and the excess linear flux at the beginning of the bright phase in the white light observations. Finally, by using some simplified arguments concerning the geometry of the magnetic field in ST LMi, I show that the secondary accretion region can be fed from the same magnetic field lines that feed the main cyclotron emis-

sion region.

Chapter 6

The accretion region of the AM Her system RE J1844-741

6.1 Introduction

In the previous chapter I applied the 'Stokes Imaging' technique, described and developed in chapter 4, to the relatively well studied and 'simple' one–pole system ST LMi. In this chapter I apply the optimisation technique to the polarimetric observations of the AM Her system RE J1844-741. I have chosen this system because it shows more complicated two–pole accretion, evident in its polarized light curves, and because it has relatively high levels of polarization which have allowed high signal–to–noise polarimetric observations to be obtained. Also, several authors (Bailey et al. 1995 and Ramsay, Potter et al. 1996) have previously modelled the polarized emission (intensity and circular polarisation only in the case of Bailey et al. 1995) from RE J1844-741 thus allowing com-

177

parisons to be made with the maps produced using the 'Stokes Imaging' technique. Furthermore, the system parameters of RE J1844-741 (for example its inclination) have not been well determined. Therefore, in this chapter, I describe an extension to the 'Stokes Imaging' technique which also searches the system parameter space.

6.2   The AM Her system RE J1844-741

RE J1844-741 was discovered during the first all–sky survey in the extreme–UV (EUV) region of the spectrum by the Wide Field Camera (WFC) on board the *ROSAT* satellite (Wells et al. 1990; Pounds et al. 1993). Follow–up optical observations by O'Donoghue et al. (1993) showed substantial variations in the cycle–to–cycle light curve with a suggested 90–min period present and a high EUV–to–optical ratio. They also obtained time-resolved spectroscopy which showed an obvious ~ 0.063–d period, in approximate agreement with the photometric data. The semi–amplitude of the radial velocity curve was found to be 270 ± 20km s^{-1}. The prominent Balmer emission lines were found to behave in essentially the same way. i.e. the blue wing of the line profiles are steeper than the red wing at one phase and vice versa half an orbital phase later. Unfortunately the photometric and spectroscopic observations were not simultaneous, nor were the accuracy of the photometric and spectroscopic ephemerides accurate enough to allow comparisons to be made. RE J1844-74 was also detected in the XRT/PSPC survey (Beuermann & Schwope 1993).

Bailey et al. (1995) obtained detailed phase–dependent spectropolari-metric, intensity and polarization data of RE J1844-741. The spectra showed

strong positive circular polarization with a spectral energy distribution rising towards the red during the bright phase. There were no resolvable cyclotron harmonic structures or atomic Zeeman lines present in the data making a precise magnetic field determination impossible. However, as Bailey et al. (1995) pointed out, the rise of the spectral energy distribution towards the red and by comparisons with other AM Her systems, the field strength is likely to be $\lesssim 25$MG.

Furthermore, they obtained phase–dependent photometry in six wave-bands and circular polarization observations in five non–standard wave-bands using the Hatfield polarimeter (Hough et al. 1991). As can be seen from figure 6.1a, the circular polarization rises from 12 per cent in the 3400-4800Å and 15 percent in the 3400–5300Å band, up to 30 per cent in the 4900–5700Å , 5500–8400Å and 6500–8400Å bands. The circular polarization is positive between phases 0.35 and 0.8 and negative between phases 0.8 and 1.35. Therefore, Bailey et al. (1995) suggested that RE J1844-74 is a 'two pole' system where the two opposite circular polarizations arise from two separate regions of opposite field polarity on the white dwarf surface. Interestingly, the circular polarization crosses zero about 0.15 of a phase later in the two bluest bands compared to the red bands. The reversal in sign of the circular polarization was not so clearly seen in the spectropolarimetric data. Bailey et al. (1995) suggested that this is indicating that the pole producing the positive polarization is the dominant pole and therefore accreting more strongly.

They also obtained Hα emission line radial velocities (see later and figure 6.7) from their phase–dependent spectra. These show large velocity variations whose full amplitude is ~ 700km s^{-1}. Maximum positive ra-

dial velocity coincides with the center of the bright phase and positive circular polarization, and maximum negative radial velocity with the center of the faint phase.

The solid lines in figures 6.1a and b show model fits of Bailey et al. (1995) to the 5500–8400Å band and the 3400–4800Å band intensity and circular polarization data. They used a magnetic field structure of a centered dipole and assumed the cyclotron emission regions to consist of arcs extended in latitude and longitude along the surface of the star. The optical depth parameter Λ was assumed to be constant along the arc. They then attempted to fit the intensity and circular polarimetry by adjusting the location and size of the arcs on the surface of the white dwarf. Similarly the system parameters, such as the inclination and magnetic dipole offset, were adjusted to match the gross features in the data.

Their best fitting model for the 3400–4800Å data had the following system parameters (they used the parameters and notation of Ferrario & Wickramasinghe 1990): a polar magnetic field strength $B_p = 25\mathrm{MG}$, an orbital inclination $i = 60°$, a dipole inclination $\theta = 130°$ and an effective harmonic number for this band of $n = 11$. The main emission region is below the orbital plane and lies close to the magnetic axis between $\theta_1 = 8°$ and $\theta_2 = 10°$ with constant angular width $\delta\theta$ along the arc. It is elongated towards the magnetic equator by $20°$. The longitude extent is between $\psi_1 = 80°$ and $\psi_2 = 200°$. The main emission region was given an electron temperature of $T_e = 10\mathrm{keV}$ and optical depth parameter $\Lambda = 10^6$. The secondary emission region was located above the orbital plane with the parameters: $\theta_1 = 166°, \theta_2 = 168°, \delta\theta = 40°, \psi_1 = 240°, \psi_2 = 400°, T_e = 10\mathrm{keV}$ and optical depth parameter $\Lambda = 2.0 \times 10^6$. Figure 6.1c shows the
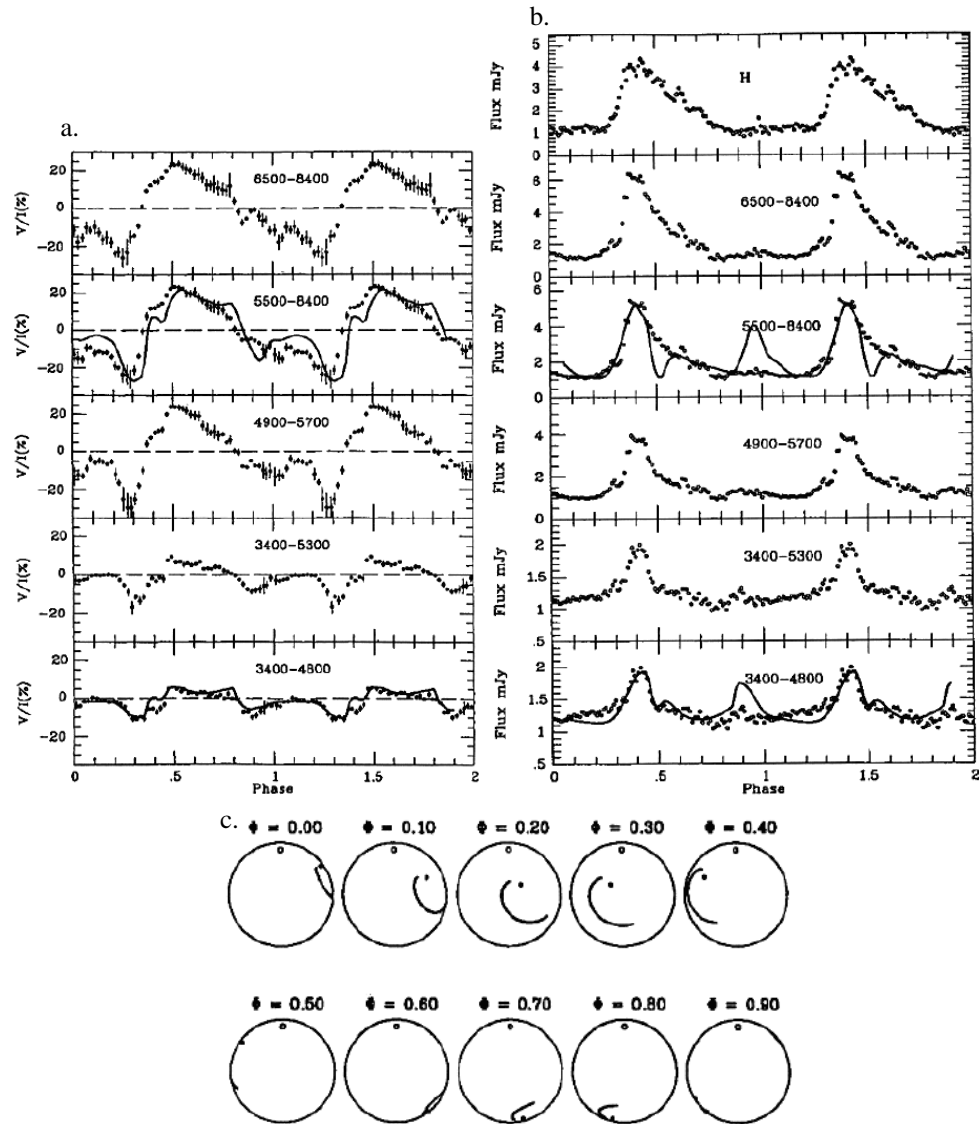
Figure 6.1: Broad band polarimetric observations of RE J1844-741 from Bailey et al (1995) with model fits (smooth curves) **a.** Circularly polarized observations.**b.** Intensity observations. **c.** Position of model arcs as seen from Earth for one orbital rotation.

emission arcs mapped onto a sphere representing the surface of the white dwarf as seen from Earth at 10 different orbital cycles.

For the 5500–8400Å observations Bailey et al. (1995) used the same geometrical parameters for the emission regions used above but with $T_e = 5\text{keV}$ and $\Lambda = 1.4 \times 10^5$ for the main emission region and $T_e = 5\text{keV}$ and $\Lambda = 2 \times 10^5$ for the secondary emission region. From figure 6.1 it can be seen that the model has fit the gross features of the observations but not the finer details. It particular, it incorrectly predicts a large intensity peak at about phase 0.

6.2.1   New polarimetric and X–ray observations

The observations and results of Bailey et al. (1995) prompted further polarimetric observations. These new data included linear polarization and its position angle variation and these results have been published in Ramsay, Potter et al. (1996). They also included X–ray observations made with *ROSAT*. I will first discuss the results of the 'hand' modelling I performed on the polarimetric observations. This will then be followed by the 'Stokes Imaging' modelling.

The data in this section is folded on a new more accurate ephemeris:

$$T = HJD2448475.2933(2) + 0.06255330(2)E,$$

where the error in the last significant figure is in brackets. The timings of the start of the bright phase published in O'Donoghue et al. (1993) and those observed in our new observations were used as the fiducial point.
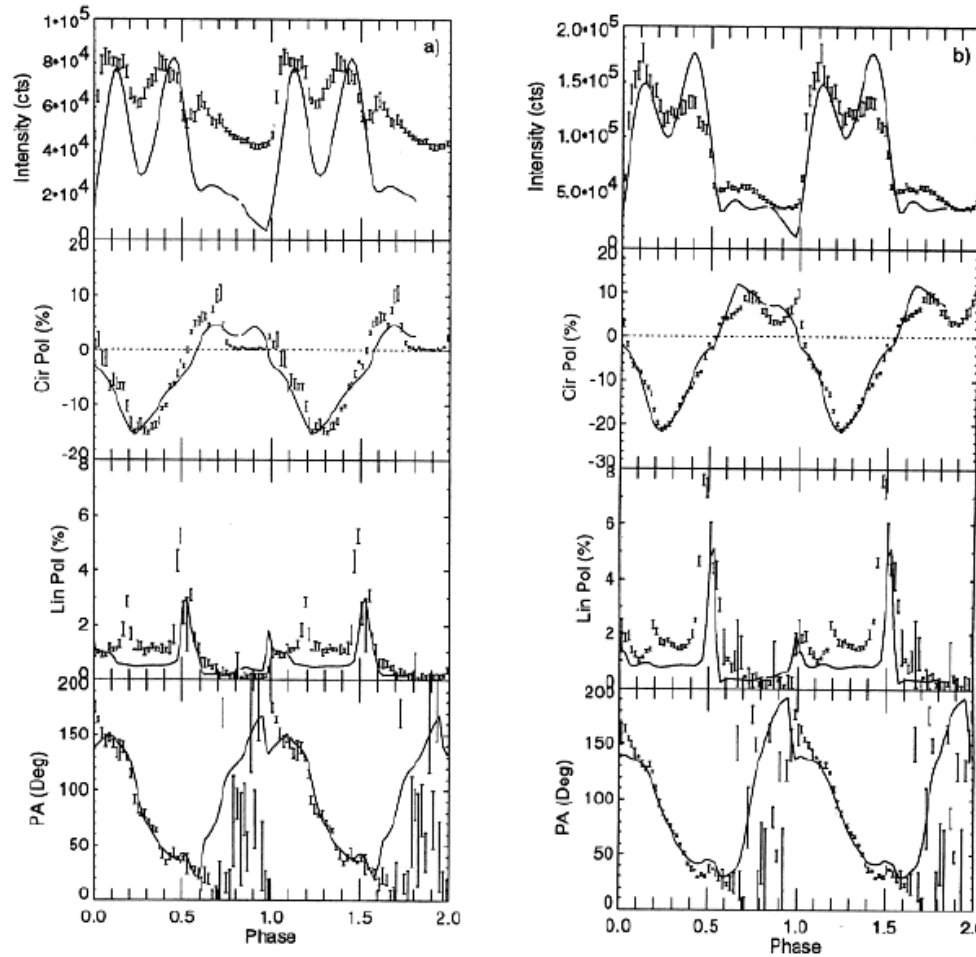
Figure 6.2: The green filter (3500–6500Å, **a**) and red filter (5500–9500Å, **b**) polarimetric observations from Ramsay, Potter et al. (1996). My best model fits are also overlaid (smooth curves).

6.2.2   Polarimetric observations

The optical photometric and polarimetric observations for this chapter, were obtained using the Faint Object Polarimeter and the Anglo–Australian telescope on 1994 July 1–4. Observations were made on alternative nights in the 5500–9500Å (OG570, red filter) and the 3500–6500Å (BG39, green filter) pass-bands with linear and circular polarization measurements taken for the first and second halves of the night respectively.

Figure 6.2a and b show the phase averaged green and red filter data folded on the above ephemeris. It can be seen from the data that the orbital cycle can be divided into a 'bright' phase and a 'faint' phase. There are two distinct peaks during the bright phase: one at $\phi \sim 0.1$ and the other at $\phi \sim 0.4$. The relative intensity of the first peak compared with the second peak is higher in the red than in the green. Also, when comparing these data with those of Bailey et al. (1995) the relative prominence of the secondary peak at $\phi \sim 0.4$ to the primary peak at $\phi \sim 0.1$ is much greater in these new data.

The linear polarization shows three peaks: the most prominent occuring at the end of the bright phase ($\phi \sim 0.5$), a second at the beginning of the bright phase ($\phi \sim 1.0$) and a third at $\phi \sim 1.2$ during the bright phase. Between $\phi \sim 0.7$ and 1.0 during the faint phase the linear polarization is zero. The position angle of linear polarization is well defined during the bright phase but not during the faint phase.

The circular polarization varies over the orbital cycle with a ~ 30 per cent peak–to–peak variation. Before the onset of the bright phase, the circular polarization increases in the positive sense before quickly becoming negative. The circular polarization then increases (in a negative sense)

reaching a maximum of ~ -20 per cent at $\phi \sim 0.25$ and then decreases to zero at $\phi \sim 0.5$. Between phases $\phi \sim 0.0$ and $\phi \sim 0.5$ the circular polarization is positive with evidence of depolarization at phase $\phi \sim 0.85$. The sign of the circular polarization presented here is opposite to that of Bailey et al. (1995). There are no circularly polarized standard stars. However, we have observed with this instrument, using the same configuration and the same reduction software, many times before and are confident that our data were reduced correctly.

The cyclotron model

In the Ramsay, Potter et al. (1996) paper I modelled the polarimetric observations using the same approach as for PQ Gem in chapter 3. I started by modelling the data taken through the red filter by considering several accretion regions on the surface of the white dwarf to obtain a crude fit to the light curves. A single accretion region is sufficient to reproduce the prominent features in the light curves. For example, the rapid increase in the intensity, circular and linear polarization at $\phi \sim 0.0$ and later their rapid decrease at $\phi \sim 0.5$ can be attributed to a single emission region appearing and disappearing from view over the limb of the white dwarf.

However, a second accretion region is required to fit the finer details of the light curves, such as the linear polarization peak at $\phi \sim 0.2$ and the positive circular polarization.

The magnetic field strength, optical depth parameter, inclination, and the colatitude of the magnetic axis were then adjusted until the model fitted all three polarization curves relatively well. Figure 6.2b shows that the accuracy of the model fit is adequate. However, some of the more de-

tailed features of the light curves are not so well reproduced: for example the linearly polarized spike at $\phi \sim 0.2$ and the general level of linear polarization throughout the bright phase. I found that by adjusting the magnetic field strength or the optical depth parameter Λ it was possible to obtain better fits to some parts of the data but made the fit to other parts of the data significantly worse. This is suggestive of variation in the optical depth parameter along the length of the accretion arcs. An inclination of $i = 80°$ and a magnetic dipole offset of $\beta = 30°$, gave the best fits. The parameters describing the location and shape of the arcs are given in table 6.1.

As radiation in both the red and the green filters is cyclotron emission from the same region, the sizes and locations of their emission regions should not be different. Therefore the same values for i, β and the parameters describing the location and shape of the emission region were used to fit the green data. However, I found that it is was not possible to achieve a good fit to the data. Better fits were obtained by increasing the value of the optical depth parameter Λ, (figure 6.2a), although again the finer details of the light curves were not always fitted. Furthermore, best fits were obtained when the magnetic field strength at the secondary pole is 10 MG greater than that at the main pole.

I found that long arcs are required to get good fits to the optical polarization data. Figure 6.3 demonstrates the effects of varying the length of the main accretion arc on the model fit to the red data. The length of the secondary region and the system parameters remain unchanged from that quoted in table 6.1. From the figures it can be seen that the effect of reducing the length of the main arc has no significant effect on the polar-

Table 6.1: The parameters describing the best fitting model solution. A plasma temperature of 10 keV was used.

Accretion Region	Range in mag long (degrees)	Range in mag lat (degrees)	Width of arc (degrees)	B (MG)	Λ(red) (10^6)	Λ(red) (10^6)
Main	200–80	8–28	2	27	0.6	7
Secondary	360–220	160–125	1	38	0.8	8

ized light curves. However, the goodness of the fit to the position angle of linear polarization deteriorates noticeably at the ingress and egress of the main accretion region. I also shortened the length of the secondary arc: this had no effect on the linear polarization or its position angle but did significantly worsen the fit to the positive circular polarization.

6.3   Genetically optimised Stokes Imaging

In the previous chapter the 'Stokes Imaging' technique was applied to the AM Her system ST LMi. This object had been relatively well studied and consequently its system parameters (inclination, magnetic field strength etc) have been estimated with different degrees of confidence. It was therefore possible to search all of its system parameter space in a reasonable amount of time. However, RE J1844-741 is a relatively new object with little or no estimates for its system parameters. It was therefore not possible to search the parameter space in a reasonable amount of time.

In chapter 4 it was explained that the system parameters were not included in the optimisation procedure. If they were, an optimal image
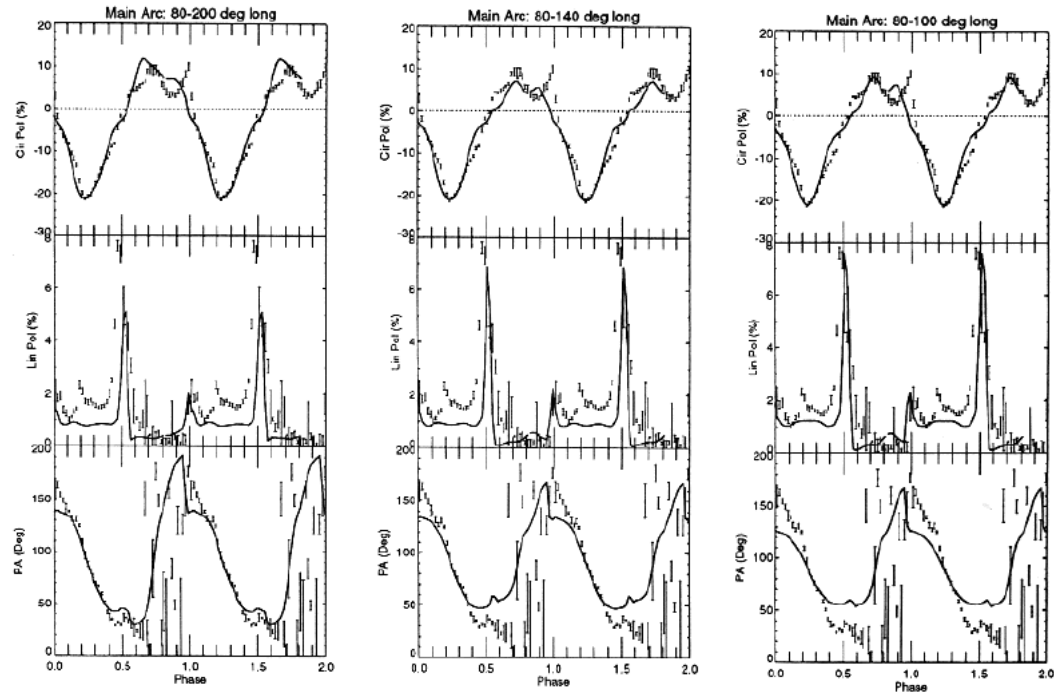
Figure 6.3: The model fits overlaid upon the red filter data for main accretion arcs of three different lengths. From Ramsay, Potter et al. 1996

would never be obtained because the system parameters would be changing too rapidly for an image solution to form. Therefore, the system parameter space has to be searched separately from that searched during the 'Stokes Imaging' technique, either by hand, as in chapter 5, or as I now describe, by the use of a genetic algorithm (GA) operating as an outer loop to the 'Stokes Imaging' procedure. There is no regularisation functional operating on the system parameters. Instead, the outer optimisation loop optimises the final fitness values produced by several optimised solutions. In effect, the optimised solutions produced by several runs of the 'Stokes Imaging' technique become child solutions themselves. The procedure can be summarised in the following steps:

- Generate an initial set of 20 random solutions

- Calculate the final fitness value for each solution using the 'Stokes Imaging' technique. The summary at the end of section 4.2.2 would apply here. Rank the solutions in order of their fitness.

- Generate the next generation of solutions while applying mutation and cloning operators.

- Repeat the last two steps until the fitness does not improve any further.

There are five parameters to be searched in the outer loop. These are the inclination, magnetic dipole offset (latitudinal and azimuthal) and the magnetic field strengths at each pole. A constant shock temperature of 10 keV was assumed. The size of the population is chosen to ensure a global search is undertaken. Furthermore, as mentioned in chapter

4, the cloning and mutation probabilities (with the population size these are collectively called genetic operators) are adjusted to ensure the most efficient method for searching the parameter space. However, GAs are relatively new tools, especially in astronomical applications. Therefore, these genetic operators are obtained by a trial and error approach. In the development of the 'Stokes Imaging' technique (chapter 4) this was a relatively straight forward task. This was because one optimisation run would take about an hour to complete. Therefore, it was possible to execute many trial solutions with different genetic operators until the most efficient and reliable values were found.

However, in the case of the outer loop optimisation procedure described above, a single member of the population takes about one hour for its final fitness value to be computed (compared to less than one second for the 'Stokes Imaging' technique). As a result, for a population of 20, it takes about 20 hours between each generation. Several generations are needed before the solutions start to converge on the global minimum. Dividing the population between other computers helps with the computation time, nevertheless it is impractical to attempt several trial runs to find the most efficient genetic operators.

Therefore, based on my experience with the 'Stokes Imaging', I have chosen a population of 20 and a mutation probability of 0.05 to inject one mutation per generation. The cloning probability is set to zero. The population size is too small for clones to improve the efficiency.

Eventually, after several days of computation time, the rate at which better solutions are found decreases. As explained in chapter 4, this is because the GA becomes less efficient when nearing the global minimum.

In the 'Stokes Imaging' technique the GA is stopped at this point and the search continued with the Powells method. This more traditional line minimisation technique then finds the minimum more efficiently. However, the size of the population used in the 'outer loop' may not be large enough to guarantee a global search, but instead may have found a local minimum. Consequently, a line minimisation routine would converge to the local minimum. Nevertheless, an examination of all the GA solutions show that there is an optimal range in the parameter space. The optimal parameter space is sufficiently small to be searched systematically in a grid of $2°$ steps for the angles and 2 MG steps for the magnetic field strengths. The parameter range is set by the best 20 solutions found by the 'outer loop'. A number of 20 was chosen to provide a good representation of the best solutions and while giving a sufficiently small parameter range to allow a systematic search in a reasonable amount of time.

6.4   Optimised model fit

Ramsay, Potter et al. (1996) and Bailey et al. (1995) obtained their model fits to the different wave–bands observations of RE J1844-741 separately. The 'Stokes Imaging' technique however, models the red and green wave–band data simultaneously. The system parameters and the location and shape of the accretion region(s) are consistent for both wave–bands. Therefore, the technique will search the parameter space in order to find a solution that will fit the morphology of the polarized light curves in both bands simultaneously while preserving the correct amount of relative flux between the two bands. The simultaneous modelling of multiwave–band

data was investigated in chapter 4. In particular, the effects of different magnetic field estimates on the final optimised solution was explored.

Figure 6.4 shows the best optimised model fit using this genetically optimised 'Stokes Imaging' technique described above. The fit presented in the figure was obtained using an inclination of $64°$, a magnetic dipole offset angle of $40°$ and magnetic field strengths of 28 and 24 MG for the upper and lower poles respectively. The upper magnetic dipole crosses the line of sight to the observer at $\phi \sim 0.6$.

Upon inspection of the final fitness values from the systematic grid, similar good fits were also possible for angles within $\pm 6°$ of the above quoted inclination and magnetic dipole offset (latitude) angles. The position of the dipole in phase is accurate to within ± 0.2 of a phase. Outside this range, the fits are dramatically worse. The accuracy to which the magnetic field strengths have been determined is less certain with the GA predicting a scatter of possible values within the range 10–30 MG. However, better fits are obtained when the upper magnetic pole has a magnetic field strength of ~ 5 MG, greater than the lower pole.

Figure 6.4 b shows that the optimised model solution has reproduced the red polarization data remarkably well . The gross morphology of all the red polarized light curves have been accurately predicted, in particular the location and size of the main linearly polarized pulse, the variation in position angle, the relative amounts of linear and circular flux, the peaks and dips in the circular polarization and the overall variation in the intensity curve.

The model fit does not accurately predict the variations in the green polarimetric observations (figure 6.4a). It has modelled the gross varia-

tions but not the finer details, in particular the green linearly polarized pulse at $\phi \sim 0.5$. This has arisen because of the less accurate determination for the magnetic field strengths thus affecting the quality of the fit to one wave-band more than the other: the relative fluxes between the two wave-bands depends on the magnetic field strength (see chapter 4). The fit to the green data can be improved by increasing the magnetic field strength on the upper pole. Maintaining a dipole field constraint, however, this makes the fit to the red data significantly worse.

The genetically optimised 'Stokes Imaging' technique has predicted an extended but broken main emission region in the lower hemisphere and a single smaller region in the upper hemisphere of the white dwarf (figure 6.4c). The main emission region appears to consist of a relatively higher density region whose center is located $\sim 25^{\circ}$ from the magnetic equator. It is extended in a south west–north east direction by $\sim 25^{\circ}$ with two relatively lower density regions extending further in the south west direction approaching the magnetic pole. The secondary emission region in the upper hemisphere is relatively less dense than the main emission region. It is also much smaller in size and almost diametrically opposed to the center of the main emission region.

Figure 6.5 shows the emission regions mapped onto a sphere representing the surface of the white dwarf as viewed from Earth for a complete orbital rotation. The observed features of the polarimetric observations (figure 6.4a,b) can be explained with reference to figure 6.5. The most prominent feature of the observations is the bright and faint phase. The main emission region in the lower hemisphere is responsible for the bright phase emission during $\phi \sim 0.0$–0.5 and the secondary smaller emis-

sion region is responsible for the faint phase emission during $\phi \sim 0.5$–1.0. The south west–north east orientation of the main emission region means that it gradually appears over the limb of the white dwarf at $\phi \sim 0.0$ and then rapidly disappears at $\phi \sim 0.5$ resulting in a large linearly polarized pulse. The secondary emission region is visible for a larger fraction of the orbital period. It first appears just before $\phi \sim 0.5$ and therefore contributes to the linearly polarized pulse. At $\phi \sim 0.85$ the magnetic field lines feeding the secondary emission region are most pointing towards the line of sight resulting in depolarization of the radiation by cyclotron self absorption as observed by the dip in the positive circular polarization. The secondary region then moves away from the line of sight resulting in an increase in emission seen as the contribution to the rapid increase in the intensity and the brief increase in positive circular polarization at $\phi \sim 1.0$. The secondary emission region continues to stay in view until ~ 0.2 of a phase after the appearance of the main emission region. The small linear pulse at $\phi \sim 1.2$ can then be identified with the disappearance of this region. The more gradual decline in the intensity from the bright phase at $\phi \sim 0.5$ (seen especially in IR observations in Bailey et al. (1995), reproduced in figure 6.1b) can be attributed to the appearance of the secondary region.

6.5   Discussion

6.5.1   The accretion region

In figure 6.6 I compare the prediction for the shape and location of the cyclotron emission region with that of previous work. The figures are
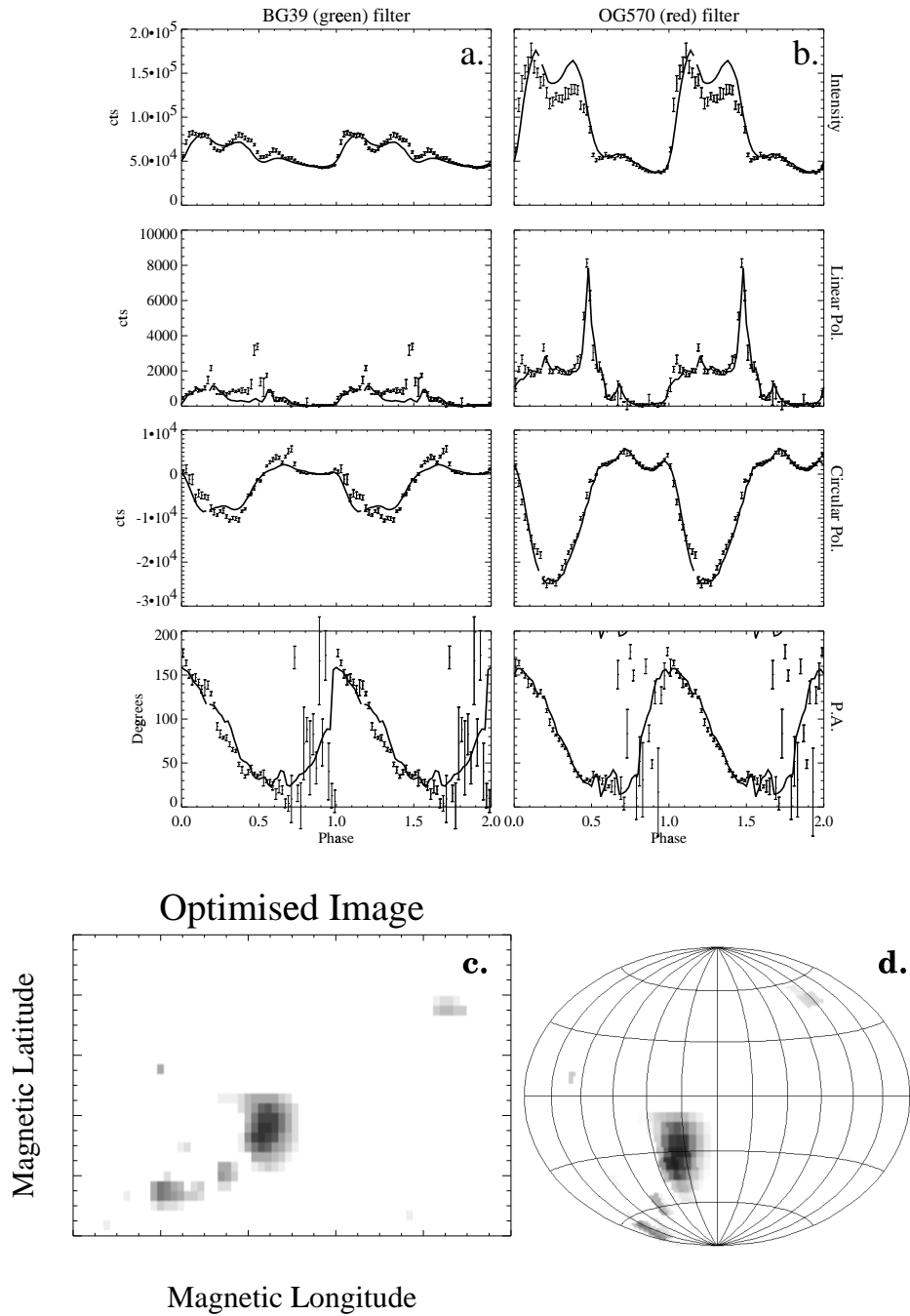
Figure 6.4: The 'Stokes Imaging' optimised solution to the polarimetric observations of Ramsay, Potter et al. (1996). **a.** The green data. **b.** The red data. **c.** The optimised image. **d.** The optimised image mapped onto an equal areas projection.
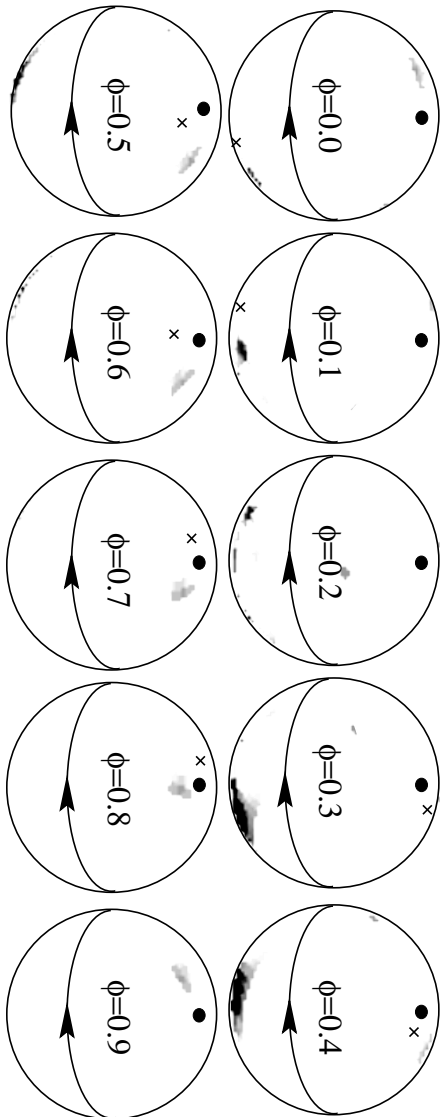
Figure 6.5: The position of the cyclotron emission regions as viewed from Earth for a complete orbital rotation. The cross represents the magnetic pole.
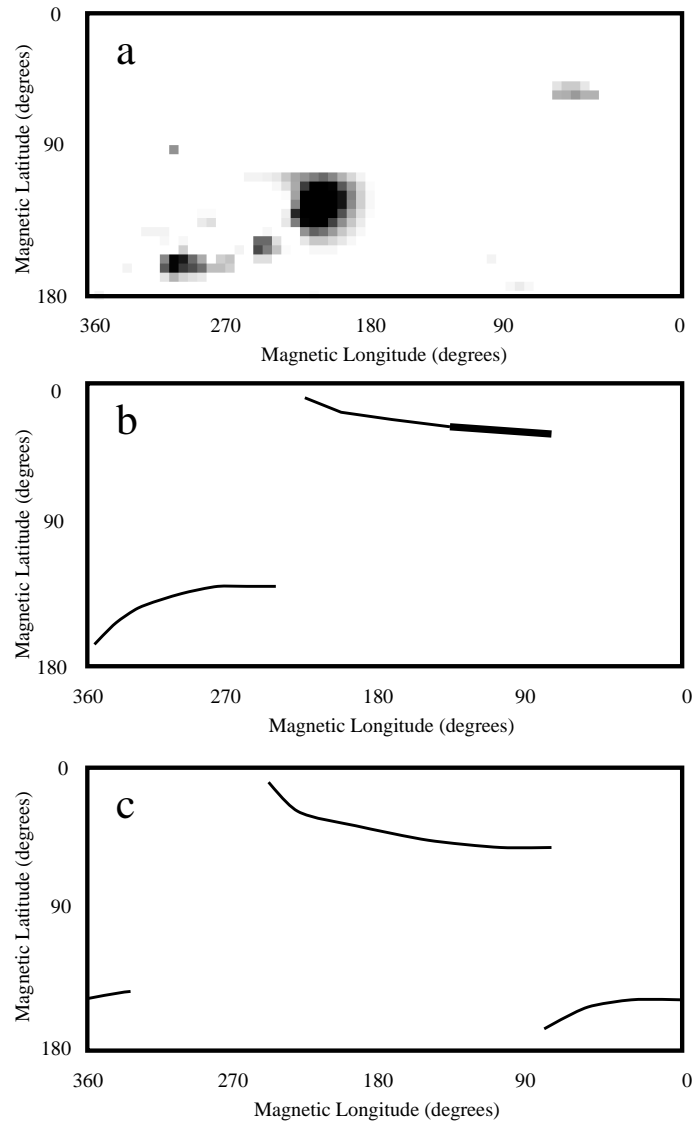
Figure 6.6: A comparison between: **a.** The optimised image solution. **b.** My model prediction in Ramsay, Potter et al. (1996) **c.** The model prediction of Bailey et al. (1995).

mapped onto a flat surface. As a result, the large differences in longitude near the polar regions are much smaller in real space on the surface of a sphere. Figure 6.6b shows my prediction for the shape and location of the emission region from Ramsay, Potter et al. (1996) which was discussed in section 6.2.3. The emission region is mapped onto the same coordinate system used throughout this thesis and defined in chapter 2. The main difference is that Ramsay, Potter et al. (1996) located the main emission region, responsible for the negative polarization, on the upper hemisphere of the white dwarf. They also used a much higher value for the inclination ($80°$) as an explanation for the equal orbital coverage of the bright and faint phases and the variation in the position angle. Furthermore, they used two long thin arcs. The only similarity is that both models predict enhanced brightness on the trailing edge of the main emission region.

Figure 6.6c shows the model prediction of Bailey et al. (1995) mapped onto the same coordinate system as figures 6.6a and b. They also predict two long thin arcs located in approximately the same locations (large changes in magnetic longitude near the poles, translate to small changes in actual position) as that of Ramsay, Potter et al. (1996). However, they locate the main emission region in the lower hemisphere in agreement with the 'Stokes Imaging' technique. Furthermore, Bailey et al. (1995) estimated an orbital inclination of $i = 60°$ and a magnetic dipole offset of $\beta = 50°$ also in closer agreement with the 'Stokes Imaging' technique.

Figure 6.7 shows the radial velocity curve of the Hα emission line from Bailey et al. (1995). The phase axis has been changed to match the ephemeris of Ramsay, Potter et al (1996). The radial velocity curve is positive and

negative during $\phi \sim 0.1$–0.65 and $\phi \sim 0.65$–1.1 respectively. These observations can be explained by the model prediction with the use of figure 6.5 in the following way. Assuming that the Hα emission line emanates from the infalling material in the stream close to the shock, then the variation in the radial velocity arises as a function of the viewing angle over the orbit. This then appears as a sinusoidal variation with a positive mean velocity for an inclination of $60°$. This is generally true for a single emission region.

In figure 6.7 I have over plotted a solid sinusoidal fit to the data omitting what appears to be a discrepant point close to $\phi \sim 0.8$. This gives a mean radial velocity of about 100 km s^{-1} as one would roughly expect for a single emission region. The dashed curve is the sinusoidal fit to all the data points. The chi squared of the fit is slightly worse and the discrepant point still stands out as a bad data point.

At $\phi \sim 0.75$–0.8 the secondary emission region is in view only. At this phase the field lines feeding the emission region appear behind in phase from over the limb of the white dwarf. Material accreting along these field lines would therefore be moving towards the observer and thus show negative radial velocities in their emission lines. Positive radial velocity occurs at $\phi \sim 0.1$–0.65 when the main emission region is in view. This emission region is below the orbital plane and thus the accreting material will mostly always be moving away from the observer.

6.5.2 The magnetic field

The genetically optimised 'Stokes Imaging' technique predicts a higher magnetic field strength for the upper magnetic pole than for the lower. If
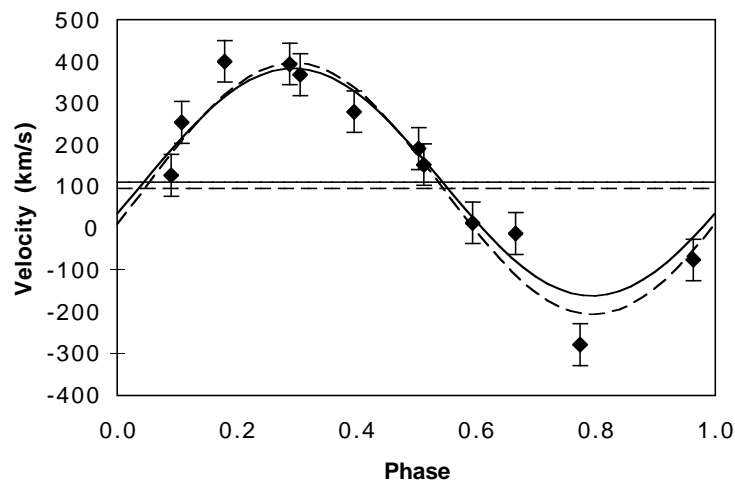
Figure 6.7: The radial velocity curve of the Hα emission line re-phased on the ephemeris of Ramsay, Potter et al. (1996). Adopted from Bailey et al. (1995). The solid curve is the sinusoidal fit neglecting the point at $\phi \sim 0.8$. Th dashed curve is the fit including the point at $\phi \sim 0.8$.

this is the case, the peak in the cyclotron flux from the secondary emission region in the upper hemisphere ought to occur at bluer wavelengths than the main emission region. This prediction can explain the observed positive circular polarization in the red bands and the negative circular polarization in the blue bands at phase ~ 0.4 (corresponding to $\phi \sim 0.0$ when using the ephemeris of Ramsay, Potter et al. 1996) of the Bailey et al, (1995) observations (figure 6.1a) in the following way. At $\phi \sim 0.0$–0.2 the model predicts both emission regions to be in view simultaneously. Therefore, the positive circular polarization from the secondary emission region dominates in the blue at $\phi \sim 0.0$ while the negative circular polarization from the main emission region dominates in the red. During $\phi \sim 0.1$–0.2, (phase ~ 0.45–0.5 in figure 6.1a), the secondary emission region begins to disappear while more of the main emission region begins to appear and dominates the circular polarization at all wavelengths.

6.5.3   The threading region

As mentioned in chapter 5 and discussed in the introduction, the structure of the accretion region in Polars depends on how and where the accreting material attaches to the field lines at the threading region. A number of physical processes and instabilities are competing in the region making a theoretical study difficult (see the introduction chapter for references and an overview). The map produced for the emission region of RE J1844-741 can give some indication of where and how material threads on to the magnetic field lines in RE J1844-741.

A simple picture of the threading process can be gained in the same manner as discussed in section 5.6.3 with ST LMi and the use of figure

5.6a. From figure 6.4c it can be seen that most of the accreting material reached the surface of the white dwarf in the lower hemisphere close to the magnetic equator. This means that the material leaving the Inner Lagrangian point must have penetrated deeply into the magnetosphere before the magnetic pressure overcame the ram pressure of the gas. Some material however, possibly in the form of higher density blobs, has accreted further around the white dwarf. This has resulted in the broken extension from the main region towards the magnetic pole and later in phase. Were the magnetic dipole field not inclined to the spin axis of the white dwarf then this material would be expected to accrete at the same magnetic latitude as the main region. However, the dipole is inclined to the spin axis by $40°$. Therefore, material that penetrates further around the white dwarf from the main region will attach to magnetic field lines emanating from closer to the magnetic pole. This description would correspond to the main accretion occurring along the field lines labelled as the secondary funnel of figure 5.6a.

As a result, the magnetic pole in the lower hemisphere appears over the limb of the white dwarf first, followed by the broken extended arc, and then by the main region. This is opposite to the situation described for ST LMi. In ST LMi the main accretion flow was along the field lines labelled as the main funnel depicted in figure 5.6a. Thus, the part of the accretion arc furthest from the magnetic pole appears over the limb of the white dwarf first, followed by the region closest to the magnetic pole and then the magnetic pole itself.

The process by which material attaches to the magnetic field lines that feed the secondary emission region in RE J1844-741 is more difficult to

determine. The problem lies in not knowing the location of the secondary star in the orbital plane in this system. Also, the secondary emission region is not attached to the opposite end of the magnetic field lines feeding the main emission region, as is the case for ST LMi. Instead it is located on approximately the diametrically opposite point of the white dwarf. Depending on the location of the secondary, there are therefore two possible scenarios by which material threads the magnetic field lines that feed the secondary emission region. Firstly, some material may penetrate even further around the white dwarf from the main threading region and attach to field lines that more easily feed the magnetic pole in the upper hemisphere of the white dwarf. In this case the secondary star would cross the line of sight at $\phi \sim 0.6-0.9$ such that it would be trailing the main emission region in phase. The other possibility is that some material attaches to magnetic field lines that feed the secondary emission region while the bulk flow continues around the white dwarf and feeds the main emission region. If this were the case then the secondary star would cross the line of sight at $\phi \sim 0.9-1.3$. Any earlier in phase it would be more likely to feed the lower magnetic pole. The first scenario is favoured because it is easier to envisage larger blobs capable of penetrating further than the main flow around the white dwarf before threading.

6.6   Summary

In this chapter I have applied an extension of the 'Stokes Imaging' technique ,developed and discussed in chapter 4, simultaneously to the green (3500–6500Å) and red (5500–9500Å) polarimetric observations of the

AM Her star RE J1844-741 from Ramsay, Potter et al. (1996).

The technique has predicted an extended main cyclotron emission region, located in the lower hemisphere of the white dwarf, and a secondary, smaller less dense region diametrically opposite. The main emission region is found to consist of a relatively higher density region whose center is located $\sim 25°$ from the magnetic equator. It has a broken extended region extending ahead in phase towards but trailing the magnetic pole. The technique also predicts a secondary emission region in the upper hemisphere which is relatively less dense than the main emission region. It is also much smaller in size and almost diametrically opposed to the center of the main emission region.

The best fits to the observations were obtained for a system inclination of $i = 64°$, a magnetic dipole offset angle of $40°$, and magnetic field strengths of 28 and 24 MG for the upper and lower poles respectively. These fits were obtained when the upper magnetic dipole crosses the line of sight to the observer at phase ~ 0.6. Outside a range of ± 0.2 of this phase, the fits are dramatically worse. Similar good fits were also possible for angles within $\pm 6°$ of the above quoted values. A constant shock temperature of 10 keV was assumed.

The accuracy in the determination of the magnetic field strengths are less certain with good fits possible within the range 10–30 MG. However, better fits are obtained when the upper magnetic pole has a magnetic field strength of ~ 5 MG, greater than the lower pole. I have also shown that the difference in the polar magnetic field strengths and the simultaneous appearance of both emission regions at $\phi \sim 0.0$–0.2 in the model, can explain the simultaneous observed positive circular polarization in

the red wave–bands and the negative circular polarization in the blue wave–bands in the multi-wave band observations of Bailey et al (1995).

The location of the emission regions are also consistent with the radial velocity measurements of Bailey et al (1995).

Finally, I have presented a simple view of the threading process in this system. This can be explained with the use of figure 5.6a in which most material accretes along the field lines, labelled the secondary funnel, forming the main emission region. The secondary emission region is then fed by a second threading region whose location depends on the location of the secondary star in the orbital plane.

Chapter 7

Summary and Conclusions

From the modelling of the two AM Her systems presented in this thesis alone, it can be seen that the nature of the threading process varies significantly from system to system. It is naive to make general conclusions from the modelling of two systems only, however some characteristics of the threading processes can be gleaned from these two systems.

First of all, the modelling does not predict long, thin arcs that the 'hand fitting' techniques predicted. Instead, the regions are more extended.

In ST LMi the stream penetrated further around the white dwarf than where the magnetic dipole pole is most pointing towards the binary plane in phase. In RE J1844-741 the material is threaded before the point at which the dipole is most pointing towards the orbital plane. These two different scenarios resulted in two types of emission regions.

In ST LMi, the accretion region appears before the magnetic dipole with the tail end of the region closest to the pole in latitude. Whereas in RE J1844-741 the dipole appears first and the tail end of the emission region is furthest from the magnetic pole in latitude. This results in two

types of intensity light curves. ST LMi's light curve shows a gradual increase then a more rapid decrease in intensity at the beginning and end of the bright phase respectively and vice versa in the case RE J1844-741.

Furthermore, the secondary accretion region in ST LMi is fed from field lines that also feed the main emission region, but in RE J1844-741 the secondary region is approximately diametrically opposite the main emission region. In both cases I have proposed that the secondary emission regions are fed by material that has 'made it' past the main threading region.

Both systems have roughly the same magnetic field geometry, in that both have unequal magnetic polar strengths. However, in ST LMi accretion occurs onto the stronger magnetic pole and onto the weaker pole in the case of RE J1844-741. Furthermore, in each case the stream will first encounter the magnetic field lines from the stronger pole. The question then arises is, why doesn't RE J1844-741 accrete more strongly at its stronger pole? One possibility is a higher accretion rate in RE J1844-741 forcing the material to 'ram' past the first pole it encounters. Only when it has penetrated deeper in to the magnetic field will it couple to the field lines. However, systems that have been observed to have different accretion rates don't appear to switch their main accretion from one pole to another. The only other possibility is that the mode of accretion is very dependent on the magnetic field strengths and their dipole orientations. This is further supported in work by, for example Wu & Wickramasinghe (1993), who have shown that offset dipoles and multipole configurations can explain the observed field alignments between the two stars in the binary. The obvious next step would be to apply the 'Stokes Imaging' tech-

nique to more systems in which the magnetic field strengths and dipole orientations are known relatively accurately and hence improve our understanding of stream/magnetic field interactions in MCVs.

Acknowledgements

References

Arons, J. & Lea, S. M. 1980, ApJ, 235, 1016.

Bailey, J. A. et al., 1985, MNRAS, 215, 179.

Bailey, J. A. et al., 1995, MNRAS, 272, 579.

Berg, R. A. & Duthie. J. G. 1977, ApJ, 211, 859.

Beuermann K., & Schwope, A., 1993, Advances in Space research, (Paper given at 1992 COSPAR meeting, Washington DC)

Beuermann K., et al, 1984, A&A, 136, 250.

Beuermann K., Burwitz V., 1995, in ASP Conf. Series Vol. 85, Proc. Cape Workshop on MCVs. Astron. Soc. Pac., San Francisco, p. 99.

Beuermann K., Stella, L. & Patterson, J., 1987, ApJ., 316, 360.

Bowyer, S., & Malina, R. F., 1991, in Extreme Ultraviolet Astronomy, eds. Malina & Bowyer, (New York: Pergamon), 397.

Buckley, D. A. H., Sekiguchi, K., Motch, C., O'Donoghue, D., Chen, A.-L., Schwarzenberg-Czerny, A., Pietsch, W., & Harrop-Allin, M. K., 1995, MNRAS , 275, 1028.

Charbonneau, P., 1995, ApJS, 101, 309.

Cowley, A. P. & Crampton, D. 1977, ApJ, 212, L121.

Cropper, M. S., 1985, MNRAS, 212, 709.

Cropper, M. S., 1986, MNRAS, 222, 853.

214

Cropper, M. S., 1986b, MNRAS, 222, 225.

Cropper, M. S. & Warner, B. 1986, MNRAS, 220, 633.

Cropper, M. S., 1989, MNRAS, 236, 935.

Cropper, M. S., Harrop–Allin, M. K., Mason, K. O., Mittaz, J. P. D., Potter,
    S. B. & Ramsay, G. T. B., 1998, MNRAS, In Press.

Cropper, M. S., 1990, Space Sci. Rev., 54, 195.

Cropper, M. & Horne, K., 1994, MNRAS, 267, 481.

Drummond, W. E. & Rosenbluth, M. N., 1963, Phys. Fluids, 6, 276.

Duck, S. R., Rosen, S. R., Ponman, T. J., Norton, A. J., Watson, M. G., &
    Mason, K. O., 1994, MNRAS, 271, 372.

Ferrario, L., & Wickramasinghe, D. T., 1990, ApJ, 357, 582.

Ferrario, L., Bailey, J. & Wickramasinghe, D. T., 1993, MNRAS, 262, 285.

Frank, J., King, A. R. & Lasota, J.–P., 1988, A&A, 193, 113.

Frank, J., King, A. R. & Raine, D.J, 1985, Accretion Power in Astrophysics,
    Cambridge University Press, Cambridge.

Ghosh, P. & Lamb, F. K., 1978, ApJ, 223, L83.

Ghosh, P. & Lamb, F. K., 1979a, ApJ, 234, 296.

Ghosh, P. & Lamb, F. K., 1979b, ApJ, 232, 259.

Haberl, F. & Motch, C., 1995, A&A, 297, L37.

Hakala, P. J., 1995, A&A, 296, 164.

Hameury, J. M., King, A. R. & Losata, J.–P. 1986a, A&A,162, 71.

Hameury, J. M., King, A. R. & Losata, J.–P. 1986b, MNRAS, 218, 695.

Harrop-Allin, M. K.; Cropper, Mark; Potter, S. B.; Dhillon, V. S.; Howell,
    Steve B., MNRAS, 288, 1033.

Hearn, D, R., Richardson, J. A. & Clark, D. W., 1976, ApJ, 210, 23.

Hellier, C., Ramseyer, T. F., Jablonski, F. J., 1993a, PASP, 105, 966.

Hellier, C., Ramseyer, T. F., Jablonski, F. J., 1993b, MNRAS, 265, L35.

Hellier, C., Ramseyer, T. F., Jablonski, F. J., 1994, MNRAS, 271, L21.

Hellier, C., 1995, in Cataclysmic Variables and Related Objects, eds. A. Evans & J. H. Wood, Kluwer Academic Publishers, London, p. 185.

Hilditch, R.W., & Bell, S.A. 1994 , MNRAS, 266, 703.

Hirose, M., & Osaki, Y. 1990, PASJ, 42, 135.

Horne,K. 1991, in Fundamental Properties of CVs ed. A.W. Shafter (U. San Diego).

Hough, J.H., Peacock, T. & Bailey, J. A., 1991, MNRAS, 248, 74.

Howell, Steve, B., Sirk, Martin, M. Ramsay, Gavin, Cropper, Mark, Cropper, Potter, Stephen, B., Rosen, Simon, R., 1997, ApJ, 485, 333.

Katz, J. I., 1985, in Cataclysmic Variables and Low–Mass Binaries, eds. D. Q. Lamb and J. Patterson, Reidel, Dordrecht, p373.

Kemp, J. C., Swedlund, J. B. & Wolstencroft, R. D. 1974, ApJ, 193, L15.

King, A. R., 1993, MNRAS, 261, 144.

King, A. R., 1995, in Buckley, D. A. H., Warner, B., eds, Cape Workshop on Magnetic Cataclysmic Variables., ASP Vol. 85, p 21.

Kraft, R. P. 1962, ApJ, 135, 408.

Kraft, R. P. 1964, ApJ, 139, 457.

Krzeminski, W. 1965, ApJ, 142, 1051.

Krzeminski, W. & Serkowski, K. 1977, ApJ, 216, L45.

Kuijpers, J. & Pringle, J. E. 1982, A&A, 114, L4.

Lamb, D. Q. 1985, in Cataclysmic Variables and Low–Mass Binaries, eds. D. Q. Lamb and J. Patterson, Reidel, Dordrecht, p. 179.

Lamb, D. Q. & Masters, A. R., 1979, ApJ, 234, L117.

Lamb, D. Q. & Melia, F. 1986, in The Physics of Accretion onto Compact

Objects, eds. K. O. Mason et al., Springer–Verlag, Berlin, p. 113.

Li, Jianke, Wickramasinghe, Dayal T.; Ruediger, Guenther, 1996, ApJ, 469, 765.

Li, J., Wickramasinghe, D. T. & Rüdiger, G., 1996, ApJ (in press)

Liebert, J. & Stockman, H. S. 1985, in Cataclysmic Variables and Low–Mass Binaries, eds. D. Q. Lamb and J. Patterson, Reidel, Dordrecht, p. 151.

Livio, M. & Pringle, J. E. 1992, MNRAS, 259, 23P.

Lubow, S. 1989, ApJ, 340, 1064.

Mason, K.O., 1997, MNRAS, 285, 493.

Mason, K.O., 1995, in Buckley, D. A. H., Warner, B., eds, Cape Workshop on Magnetic Cataclysmic Variables., ASP Vol. 85, p 225.

Mason, K. O., Watson, M. G., Ponman, T. J., Charles, P. A., Duck, S. R., Hassal, B. J. M., Howell, S. B., Ishida, M., Jones, D. H. P., & Mittaz, J. P. D., 1992, MNRAS 258, 794 (M92).

Mason, K. O., Hassall, B. J. M., Bromage, G. E., Buckley, D. A. H., Naylor, T., O'Donoghue, D., Watson, M. G., Bertram, D., Branduardi-Raymont, G., Charles, P. A., Cooke, B., Elliott, K. H., Hawkins, M. R. S., Hodgkin, S. T., Jewell, S. J., Jomaron, C. M., Sekiguchi, K., Kellett, B. J., Lawrence, A., Mchardy, I., Mittaz, J. P. D., Pike, C. D., Ponman, T. J., Schmitt, J., Voges, W., Wargau, W., & Wonnacott, D. 1995, MNRAS, 274, 1194.

Masters, A. R., 1978, PhD Thesis, Unversity of Illinois.

Meggitt, S. M. A., &, Wickramasinghe, D. T. 1982 (MW82), MNRAS, 198, 71.

Milgrom, M & Salpeter, E. E. 1975, ApJ, 196, 583.

Harberl, F. & Motch, C., 1995, A&A, 297, L37.

Mukai, K. 1988, MNRAS, 232, 175.

Norton, A. J., Beardmore, A. P., & Taylor, A. P. 1996. MNRAS, in press.

Norton, A. J., McHardy, I. M., Lehto, H. J., Watson, M. G. 1992, MNRAS, 258, 697.

O'Donoghue, D., et al., 1993, MNRAS, 265, 545.

Patterson, J. 1984, ApJS, 54, 443.

Patterson, J., &, Thomas, G. 1993, PASP, Vol. 105, No. 683, 59.

Patterson, J. 1994, PASP, Vol. 106, No. 697, 209.

Pavlov, G. G., Mitrofanov, I. G. & Shibanov, IU. A. 1980, Ap&SS, 73, 63.

Peacock, T., Cropper, M. S., Bailey, J. A., Hough, J. H. Wickramasinghe, D. T., 1992, MNRAS, 259, 583.

Penning, W. R., Schmidt, G. D., & Liebert, J. 1986, ApJ, 301, 885.

Piirola, V., Hakala, P., & Coyne, S. J., 1993, ApJ, 410, L107.

Piskunov, N. E., Tuominen, I. & Vilhu, O. 1990, A&A, 230, 363.

Potter, S. B. Cropper, M. S., Mason, K. O., Hough, J. H., Bailey, J. A., 1997, MNRAS, 285, 82.

Potter, S. B. Hakala, P., Cropper, M. S., 1998, MNRAS submitted.

Pounds, K. A. et al., 1993, MNRAS, 260, 77.

Press, W. H., Teukolsky, S. A., Vetterling, W. T. & Flannery, B. P., 1992, Numerical Recipes in FORTRAN, Cambridge University Press, p406.

Pye, J. P., Mcgale, P. A., Allan, D. J., Barber, C. R., Bertram, D., Denby, M., Page, C. G., Ricketts, M. J., Stewart, B. C., & West, R. G., 1995 , MNRAS, 274, 1165.

Ramsay, G., Mason, K. O., Cropper, M., Watson, M. G. & Clayton, K. L. 1994, MNRAS, 270, 692.

Ramsay, Gavin., Cropper, Mark., Wu, Kinwah & Potter, Stephen., 1996, MNRAS, 282, 726.

Rosen, S. R., Mittaz, J. P. D., & Hakala, P. J., 1993, MNRAS, 264, 171.

Schmidt, G. D. Stockman, H. S & Margon, B. 1981, ApJ, 243, L157.

Schmidt, G. D., Stockman, H. S. & Grandi, S. A., 1983, ApJ, 271, 735.

Schwope, A. D., 1990, Rev. Mod. Astr., 3, 44.

Schwope, A. D., et al 1995a in Magnetic Cataclysmic Variables, eds D. Buckley, B. Warner, ASP Conf. Ser. 85, 166.

Schwope, A. D., 1995b, in Cataclysmic Variables and Related Objects, eds. A. Evans & J. H. Wood, Kluwer Academic Publishers, London, p. 189.

Shore, S. N., Foltz, C. B., Wasilewski, A. J., Byard, P. L. & Wagner, R. M., 1982. PASP., 94,682.

Sirk, M. M., Vallerga, J. V., Finley, D. S., Jelinsky, P., Malina, R. F., 1997, ApJS, 110, 347.

Stavroyiannopoulos, D., Rosen, S. R., Watson, M. G., Mason, K. O. & Howell, S. B. 1997, MNRAS, 288, 891.

Stockman, H. S., Schmidt, G. D., Angel, J.R.P., Liebert, J., Tapia, S. & Beaver, E. A. 1977, ApJ, 217, 815.

Stockman, H. S., Foltz, C. B., Schmidt, G. D. & Tapia, S., 1983, ApJ., 271, 725.

Swedlund, J. B., Kemp, J. C. & Wolstencroft, R. D. 1974, ApJ, 193, L11.

Tapia, S. 1977a, ApJ, 212, L125.

Tapia, S. 1977b, Int. Astr. Union Circ., No. 3054.

Tikhonov, A. N., 1963 Soviet. Math. Dokl. 4, 1624.

Väth, H., Chanmugam, G. & Frank, J. 1996, ApJ, 457, 407.

Visvanathan, N. & Wickramasinghe, D. T. 1979, Nature, 281, 47.

Walker, M. F. 1954, PASP, 66, 230.

Warner, B. 1995, Cataclysmic Variable Stars, Cambridge Astrophysics Series 28, Cambridge University Press.

Watson, M. G., 1986, in Mason, K. O., Watson, M. G., & White, N. E., eds, Lecture Notes in Physics: Proceedings of Workshop on 'The Physics of Accretion onto Compact Objects', Tenerife, Spain, Springer–Verlag, p. 97.

Watson, M. G., 1995, in Magnetic Cataclysmic Variables, eds D. Buckley, B. Warner, ASP Conf. Ser. 85, 179.

Wells, A. A. et al., 1990, Proc. SPIE, 1344, 230.

Whitehurst, R., & King, A. R. 1991, MNRAS, 249, 25.

Wickramasinghe, D. T., 1988, in Coyne G. V., Magalhaes A. M., Moffat A. A. F. G., Schulte–Ladbeck R. E., Tapia S., Wickramasinghe, D. T., eds, Polarized Radiation of Circumsteller Origin, Vatican Obs. Publ., p. 1

Wickramasinghe, D. T., & Meggitt, S. M. A., 1985 (WM85), MNRAS, 214, 605.

Wickramasinghe, D. T., & Ferrario, L., 1988, ApJ., 334, 412.

Wickramasinghe, D. T., Wu, K., & Ferrario, L., 1991, MNRAS, 249, 460

Wickramasinghe, D. T., 1993, in Spectral Line Shapes, eds. L. Frommhold & J. Keto, A.I.P. New York, 6, 574.

Wynn, G. A. & King, A. R. 1995, in ASP Conf. Series Vol. 85, Proc. Cape Workshop on MCVs. Astron. Soc. Pac., San Francisco, p. 196.